HHS Public Access

Author manuscript

Chem Soc Rev. Author manuscript; available in PMC 2018 April 18.

Published in final edited form as:

Chem Soc Rev. 2017 April 18; 46(8): 2158–2198. doi:10.1039/c6cs00765a.

Advanced optoacoustic methods for multiscale imaging of *in vivo* dynamics

X. L. Deán-Ben[a], **S. Gottschalk**[a], **B. McLarney**[a,b], **S. Shoham**[c], and **D. Razansky**[a,b]

[a]Institute for Biological and Medical Imaging (IBMI), Helmholtz Center Munich, Ingolstädter Landstr. 1, 85764 Neuherberg, Germany

[b]Faculty of Medicine, Technical University of Munich, Ismaninger Str. 22, 81675 Munich, Germany

[c]Department of Biomedical Engineering, Technion – Israel Institute of Technology, 32000 Haifa, Israel

Abstract

Visualization of dynamic functional and molecular events in an unperturbed *in vivo* environment is essential for understanding the complex biology of living organisms and of disease state and progression. To this end, optoacoustic (photoacoustic) sensing and imaging have demonstrated the exclusive capacity to maintain excellent optical contrast and high resolution in deep-tissue observations, far beyond the penetration limits of modern microscopy. Yet, the time domain is paramount for the observation and study of complex biological interactions that may be invisible in single snapshots of living systems. This review focuses on the recent advances in optoacoustic imaging assisted by smart molecular labeling and dynamic contrast enhancement approaches that enable new types of multiscale dynamic observations not attainable with other bio-imaging modalities. A wealth of investigated new research topics and clinical applications is further discussed, including imaging of large-scale brain activity patterns, volumetric visualization of moving organs and contrast agent kinetics, molecular imaging using targeted and genetically expressed labels, as well as three-dimensional handheld diagnostics of human subjects.

Graphical Abstract

Multi-scale optoacoustic imaging - from single cells to whole organisms, from sub-millisecond biological dynamics to longitudinal studies with unprecedented image quality.

Correspondence to: D. Razansky.

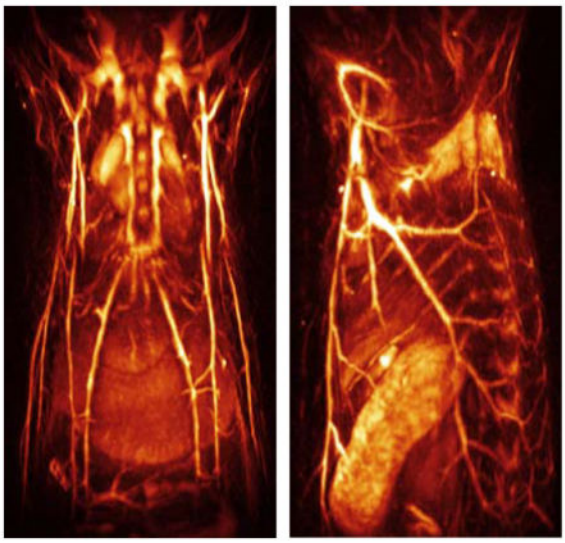

1. Introduction

Living systems exhibit complex, multi-level processes whose behaviour is difficult to predict or understand by making observations at a single spatial or temporal scale. Diseases are often manifested via anatomical alterations or functional failures at the organ or whole-body level, yet their precursors are most efficiently detected by specific molecular targeting and imaging at the cellular or sub-cellular scales. Similarly, many biological processes are manifested at multiple temporal scales, e.g. local neural activity occurring on a millisecond scale is closely linked to much slower cerebral hemodynamic changes through a mechanism known as neurovascular coupling.

In vivo imaging across multiple scales is commonly associated with challenging compromises between the achievable contrast, imaging speed and spatial resolution [1]. For example, ultrasound (US) imaging is capable of imaging whole mammalian organisms with high imaging speed accounting for fast motion and perfusion but it chiefly captures mechanical tissue properties or blood flow [2]. Conversely, optical imaging uses contrast mechanisms that offer a highly versatile ability to visualize biological processes at the cellular and molecular levels. By using powerful new classes of probes based on fluorescence dyes, reporter genes and nanoparticulate agents, previously invisible processes associated with tissue function, disease progression and treatment can now be sensed, both in real time and longitudinally. In particular, the Nobel prize winning discovery of fluorescent proteins led to reporter molecules that enable intrinsic tagging of cells, thereby facilitating the observation of cellular or subcellular activity, from gene expression and protein function to signaling pathways. While these breakthroughs provided new windows for microscopically interrogating systems level biology [3, 4], inherent optical limitations restrict the effective imaging depth of most optical microscopy techniques to below a millimeter in highly scattering tissues [5].

Macroscopic imaging approaches, such as fluorescence molecular tomography (FMT) [6] make use of the reduced haemoglobin absorption in the 650–950 nm spectral window to visualize optical contrast through several centimeters in highly vascularized mammalian tissues. Promising new developments include the introduction of near-infrared-shifted fluorescent molecules that can be used for *in vivo* labeling of deep tissue functional and molecular processes [7–9]. However, in-depth optical observations remain complicated due to intense photon scattering that contributes to a significant resolution loss and limited quantification capacity beyond a few hundred microns depth.

Optoacoustic (photoacoustic) imaging is increasingly attracting the attention of the biomedical research community due to the important new features that it added to the existing imaging toolset. The technique capitalizes on the inherent advantages of both optics and ultrasound as it uses short-pulsed light radiation as probing energy and detects ultrasound generated by photon absorption and thermoelastic expansion [10]. As a result, optoacoustics reports on the versatile optical absorption contrast but relative to other optical methods provides a sort of ‘super-vision’ by exploiting the low scattering of ultrasound to break through the barriers imposed by optical diffusion. Furthermore, multi-spectral optoacoustic tomography (MSOT) readings based on multi-wavelength excitation enable identifying chemical composition of biological samples via spectroscopic analysis, and hence render additional information not captured by other modalities [11].

The label-free optical absorption contrast explored in biomedical optoacoustics readily provides ‘illuminating’ information regarding the presence of intrinsic tissue components such as oxy- and deoxy-haemoglobin, melanin, bilirubin, lipids and water [12]. The strong optical absorption of haemoglobin allows the visualization of vascular structures and hemodynamic responses, maintaining sub-millimeter resolutions at depths of several centimetres within highly scattering living tissues for near-infrared (NIR) wavelengths [13]. Furthermore, bio-chromophores have specific spectral signatures that allow them to be distinguished from each other within an integrated absorption signal, with their relative signals contributing diverse information about function and/or pathological status of the tissue being examined [14]. Another important property of the optoacoustic methodology is the great assortment of exogenous compounds that can be explored for specifically enhancing the absorption contrast. Due to the versatility and wide availability of optical labeling approaches, optoacoustic imaging studies of e.g. gene expression or targeted bio-markers can be done in a similar way by resolving the accumulation of agents with specific spectral signatures [12]. These include fluorescent molecular probes, fluo- and chromo-proteins, quantum dots, gold-, carbon-, and polymer-based nanoparticles, porphyrins or even contrast agents used in other imaging modalities, such as microbubbles or iron oxide particles. Finally, optoacoustics provides a unique multiscale imaging capacity, allowing bridging the gap between the microscopic and macroscopic realms with the same type of contrast [13].

Taken together, these key enabling properties have prompted the development of high throughput optoacoustic systems for *in vivo* pre-clinical and clinical imaging, further providing high sensitivity and spatial resolution, portability, as well as real-time operation capability. The temporal dimension has paramount importance in biological observations in

allowing the study of complex interactions that are otherwise invisible in single snapshots of living systems. In this context, real-time optoacoustic imaging in two or three dimensions has been made possible by simultaneous detection of dense tomographic information around the imaged object for each excitation laser pulse [15]. The most recent efforts in the field of optoacoustic functional and molecular imaging have established new technological platforms employing spherical matrix arrays, parallel acquisition hardware, GPU-based data processing and fast laser tuning systems in order to enable acquisition and visualization of spectroscopic information from entire tissue volumes at video rates. This has set the stage for the so-called five dimensional (real-time three-dimensional multi-spectral) optoacoustic imaging to emerge as a new tool poised to offer unprecedented insights in biological discovery [11]. This review highlights on the most recent advances that enable powerful new applications for visualizing multiscale *in vivo* dynamics, from neural activation and real-time kinetics at the organ level to whole-body longitudinal studies of tumour progression. Optoacoustic contrast agents are classified according to their *in vivo* stability, specificity, and dynamic contrast enhancement properties while multiple examples of novel applications involving visualization of multiscale *in vivo* dynamics are further introduced.

2. Optoacoustic approaches enabling imaging of biological dynamics

In this section, existing optoacoustic imaging approaches are reviewed, focusing on the temporal scales covered by each approach and the amount of information delivered. The principles of optoacoustic signal generation are first introduced along with the general limitations affecting the potentially achievable imaging rate. The dynamic capabilities of multi-dimensional imaging systems operating at microscopic to macroscopic spatial scales are then described.

2.1. Optoacoustic signal generation

Optoacoustic signals correspond to pressure waves generated thermoelastically by absorption of photons. Typically, a pulse of light gets absorbed in the tissue, depositing a tiny amount of heat in the optical absorption zone. The instantaneous thermal expansion causes an initial pressure increase and subsequent emission of stress (ultrasound) waves (Fig. 1).

If the characteristic thermal diffusion length of the medium is shorter than the spatial resolution of the imaging system during the laser pulse, the so-called thermal confinement regime is maintained. This corresponds to no leakage of energy out of the effective optical absorption zone, and maximal thermal energy densities are attained. Considering a typical thermal diffusivity of $D \sim 0.1$ mm^2/s in soft biological tissues, this condition can be readily met for typical biological imaging applications that use nanosecond-duration laser pulses [16]. In addition, a stress confinement regime is fulfilled if the laser pulse duration is shorter than the time required for the generated stress wave to propagate out of the heated region defined by the effective spatial resolution [16]. For instance, given a common speed of sound of ~1540 m/s in soft tissues, the stress confinement condition would be readily fulfilled for the laser pulse duration of ~10 ns and a typical diffraction-limited spatial resolution of ~100

μm of the imaging system (corresponding to ultrasonic detection bandwidth in the 10 MHz range).

Using pulse durations satisfying both thermal and stress confinement regimes, the initial local pressure rise p_0 induced by laser energy deposition and subsequent instantaneous heating can be simply expressed via [17]

$$p_0 = \Gamma \mu_a \Phi, \quad (1)$$

being μ_a and Φ the local optical absorption coefficient and light fluence, respectively. Γ is the dimensionless Grüneisen parameter, which lumps together the thermoelastic properties of the medium, i.e. [16]

$$\Gamma = \beta c^2 / C_p, \quad (2)$$

where β is the thermal expansion coefficient, c is the speed of sound and C_p is the specific (per unit mass) heat capacity at constant pressure. In simple terms, the locally-induced optoacoustic pressure is proportional to the thermoelastic constant of the medium, the local optical absorption coefficient and the amount of light energy reaching this point, the latter being basically proportional to the per-pulse laser energy. In the case of fluorescent agents, the optoacoustic generation efficiency is reduced since only non-radiative relaxations directly contribute to the elastic wave conversion, in which case the effective thermoelastic conversion efficiency Γ_{eff} can be expressed as [18, 19]

$$\Gamma_{\text{eff}} = (1 - QY)\Gamma, \quad (3)$$

with QY representing the quantum yield of the molecule. Note that light absorption in solid nanoparticles is further accompanied by a different heat conduction mechanism than for small molecules dissolved in a liquid. Thereby, the thermoelastic convertion efficiency is further conditioned by the heat propagation rate and the thermal resistance at the surface of nanoparticles, which can significantly affect Γ_{eff} [20].

Safe application of optoacoustic imaging to human subjects implies that the light fluence on the skin surface is maintained below the permissible exposure standards. ANSI safety limits establish that the per-pulse laser fluence must be kept below 20 mJ/cm^2 for wavelengths below 700 nm, increasing towards 100 mJ/cm^2 at 1050 nm [21]. Considering a typical value (Γ~0.2) of the Grüneisen parameter in soft biological tissues and the permissible fluence levels, the maximum local optoacoustic pressure that can be induced in blood is approximately 738 kPa at 584 nm and 26 kPa at 797 nm (two isosbestic wavelengths of haemoglobin). ANSI safety standards further establish the maximum mean laser intensity for continuous exposure of the same area. This limit is 200 mW/cm^2 for wavelengths below

700 nm, increasing to 1000 mW/cm^2 at 1050 nm [21]. The ANSI limits result in a trade-off between the maximal per-pulse energy and pulse repetition rate of the laser that fulfill both safety criteria.

The last part of the optoacoustic imaging problem concerns the propagation of the generated pressure waves towards the US detectors (Fig. 1). The distance from the absorbers to the measurement location is encoded by the time-of-flight of the detected US signals. On the other hand, the actual size of the absorber is encoded by the duration of the detected time-resolved signal, or equivalently by its frequency spectrum. In general, higher US frequencies are generated by smaller absorbers. Typical optoacoustic waveforms generated in highly heterogenous living tissues carry a mixture of signals generated by absorbers of different sizes. Thus, they generally contain a wide range of frequencies, from several tens of kHz up to several tens of MHz, which imposes wideband detection requirements on the detectors employed in the imaging system.

2.2. Optical-resolution microscopy

Since optoacoustics involves both optical excitation and acoustic detection, it offers a great diversity of possible embodiments of the imaging device. One common approach is based on selective excitation of a spot of the surface of the tissue by focusing the incident laser beam. This modality, often termed as optical-resolution photoacoustic microscopy (OR-PAM), can resolve optical absorption contrast in cellular and sub-cellular structures with spatial resolution limited by optical diffraction (Fig. 2). Note that point-by-point scanning of the tightly focused laser beam is employed, which implies no continuous illumination of the same spot. Thereby, limits on the mean power are not applicable and only the peak fluence needs to be capped. As a result, pulse energies below 1 μJ are typically employed to avoid tissue damage [10]. The light beam is generally shaped so that the depth range of interest is covered within the optical depth-of-field. In biological tissues, however, the reachable depth is limited by light scattering, which prevents effective focusing beyond ~1 mm depth [5], similarly to the optical microscopy techniques. Yet, in optoacoustic microscopy, one-dimensional (1D) image profiles along the depth direction can be readily obtained from the optoacoustic signal collected by a coaxially aligned ultrasound transducer following a single laser pulse [23, 24]. Two- (2D) or three-dimensional (3D) images are subsequently formed by raster-scanning the excitation beam along the region of interest and superimposing the 1D profiles acquired for each position.

The lateral resolution is given by the width of the focused light beam and is generally in the micrometer range [13]. In general, a tighter focus implies better lateral resolution at the expense of the depth of field. This can be achieved e.g. with a trans-illumination approach, where ultrasound signals are detected from the opposite side of the sample. Trans-illumination can be used to efficiently combine optical and optoacoustic microscopy into an integrated multi-modal system [25, 26]. However, an epi-illumination approach is generally preferred as it produces less acoustic distortions, particularly for thick samples. To date, multiple epi-illumination-based systems have been suggested [27–31]. The lateral resolution can further be enhanced with super-resolution approaches based on several non-linear mechanisms [32–37]. The axial (depth) resolution, typically on the order of tens of microns

[10], is determined by the frequency bandwidth of the collected optoacoustic signals. In principle, ultra-wideband detection (in the GHz range) of optoacoustic responses excited with very short (sub-nanosecond) laser pulses provides a way of bringing the axial resolution down to micron levels [38]. However, these ultrasound frequencies are strongly attenuated in tissues, which limits the effective penetration depth of this approach to a few tens of microns [39].

Much like in other raster-scan-based imaging methods, such as confocal or multi-photon microscopy, the time required to form an image is determined by the pulse repetition frequency of the laser and the number of scanning points. In contrast to those methods, no depth scanning is needed. However, the separation between subsequent laser pulses must be longer than the time-of-flight of ultrasound waves so that no overlap is generated between the acquired signals. For instance, it takes about 0.67μs for the acoustic wave to travel a distance of 1 mm in soft tissues, so that the laser pulse repetition rate must be kept below 1.5MHz to avoid overlap. Thus, in an ideal case scenario, a typical raster-scan of 500x500 points would require about 0.17 s if no signal averaging is applied. Faster imaging can be achieved if the scanning is limited to a single axis for rendering cross-sectional (B-mode) images, which has been used e.g. to track individual red blood cells in capillaries [40, 41]. Several approaches were suggested to further increase the imaging speed. For example, by combining multifocal illumination with a microlens array and parallel signal detection with an US array, the imaging speed was enhanced by a factor of 3 to 4 [42]. A different class of approaches consist in random-access scanning with a digital micro-mirror device (DMD), where only selected points in a 2D region are acquired [43], or in mechanical scanning along an arbitrary 3D trajectory [44].

2.3. Scanning-based acoustic-resolution approaches

Despite its excellent spatial resolution performance, the effective penetration depth of OR-PAM is severely limited by photon scattering, similarly to other optical microscopy techniques. For depths beyond ~1 mm, progressive randomizations of the propagation directions of photons prevent light focusing with standard optical elements. Optoacoustic imaging at greater depths can be instead achieved with acoustic resolution via raster-scanning of focused ultrasound detectors [45]. For this, higher pulse energies, typically in the millijoule range [10], are required to compensate for light scattering and attenuation in deep tissues. When using spherically-focused US detectors, 3D images can be formed in the same manner as in OR-PAM, i.e. by simply stacking depth profiles acquired from individual laser shots. Optoacoustically-generated waves in tissues typically exhibit an ultrawide bandwidth, thus cannot be efficiently focused, especially in the lower frequency range. Thereby, more sophisticated image formation approaches based on properly modelling the frequency-dependent sensitivity field of the transducer are generally preferred for optimizing image quality [46–48]. Resolution and imaging depth can be easily scaled by properly selecting the effective detection bandwidth of the ultrasound detector. Indeed, it is possible to operate at acoustic resolution covering spatial scales ranging from major vessels [49] to capillaries [50] all the way to individual cells [51]. Both axial and lateral resolutions are determined ultrasonically and hence can be enhanced using higher frequency detectors. Higher resolution however comes to the detriment of the achievable depth due to the

reduction of the depth-of-field of the transducer and the increase in acoustic attenuation. A hybrid optical-acoustic resolution optoacoustic microscopy approach has been realized using coaxial illumination and detection design [52]. This ascertains smooth transition between optical resolution in superficial microscopic imaging into ultrasonic resolution when imaging at greater depths within intensely scattering tissue layers.

Alternative scanning approaches based on signal acquisition at a set of projections around a biological sample have been suggested. This imaging approach, referred to as optoacoustic tomography, essentially replaces spherically focused detection with tomographic scanning of unfocused or cylindrically-focused detectors. Here image formation is based on reconstruction algorithms, such as e.g. back-projection or model-based inversions [54–57], analogous to those used in other tomographic imaging modalities. In fact, the first *in vivo* optoacoustic images from small animals were obtained with a tomographic optoacoustic system based on a cylindrically-focused transducer scanned around the head of a rat [58]. The same tomographic scanning geometry has also been used e.g. for imaging small animals of different sizes [59–61] or human fingers [62]. Other tomographic imaging approaches based on cylindrical [63] or spherical [64] trajectories have further been suggested. High energies per pulse, typically tens of millijoules [10], and large illumination areas are generally employed in optoacoustic tomography as unfocused detection is commonly used to reach deeper areas. An all-optical tomographic optoacoustic imaging system has been implemented which uses, in addition to the optoacoustic excitation light, a focused interrogation laser beam that is scanned along the surface of a Fabry-Pérot polymer film sensor that changes its local thickness in response to the impinging optoacoustic waves [65]. In this way, tomographic information along a planar surface is collected using unfocused (point) detection, resulting in accurate 3D reconstructions (Fig. 3). In some cases, the distinction between optoacoustic microscopy and optoacoustic tomography is rather vague. For example, a combination of raster-scans with a focused transducer at multiple orientations has also been suggested for high resolution imaging of zebrafish larvae [66].

Analogously to optoacoustic microscopy, the image acquisition speed in scanning optoacoustic tomography is determined by the number of measurement locations. Data acquisition can be accelerated by using compressed sensing schemes [67–69]. Parallelization of an all-optical detection approach was proposed by detecting optical integrating line detectors with a CCD camera [70]. Additional acceleration can be achieved by scanning ultrasound arrays instead of single detectors. Various scanning geometries have been proposed using linear and curved arrays in order to render whole-body 3D images from small animals [71–73] or from the human breast [74].

2.4. Cross-sectional array-based imaging

The tomographic optoacoustic methods described above are clearly fundamentally constrained by the need for mechanical scanning. This constraint can be completely or partially removed when rendering images using parallel optoacoustic data acquisition from multiple locations after every laser pulse. This is similar to B-mode ultrasonography based on linear arrays, which does not require mechanical scanning to form 2D images in real time. Cross-sectional optoacoustic imaging based on the same configuration has been

developed [75, 76], where the illumination of the tissue is provided from the lateral sides of the transducer array via fibre bundles [76] or via an integrated laser diode module [77]. If all signals are simultaneously collected without multiplexing, the imaging frame rate is determined by the pulse repetition rate of the laser. This essentially implies that the temporal resolution is theoretically limited by the time-of-flight of pressure waves across the imaged region [78]. The main advantage of this approach is that it can be readily integrated into a multi-modal imaging systems rendering co-registered ultrasound and optoacoustic images [79–81]. Furthermore, it is compatible with handheld operation, facilitating clinical translation. Conversely, while linear arrays are convenient for ultrasonography, they are highly suboptimal for optoacoustic imaging as the tomographic reconstructions manifest severe limited-view artefacts, which limit visibility of tissue morphology [82].

Indeed, it has been shown that accurate optoacoustic reconstructions imply collection of signals from a large tomographic view surrounding the imaged object [83]. For instance, MSOT small animal scanners use tomographic data collection with partial- or full-ring concave transducer arrays to render cross-sectional reconstructions in real time (Fig. 4) [84, 85]. The technique uses advanced lasers with fast wavelength tuning capacities in order to acquire tomographic information at multiple illumination wavelengths [86]. The distribution of the intrinsic tissue chromophores and extrinsically-administered contrast agents are subsequently mapped using spectral unmixing approaches [87]. 3D images of the entire animal can further be obtained by scanning the array along the elevational dimension [88]. The important advantages of this approach related to real-time image acquisition have led to its widespread use in biological research [89–92]. For example, dynamic imaging of fast biological events is possible at video rate of 50 frames per second or faster, essentially limited by the pulse repetition frequency of the laser [15]. In this configuration, imaging is facilitated by horizontal placement of the mouse on a membrane surface without direct contact with water, thus assuring ease of handling and high-throughput performance [88]. Handheld optoacoustic probes based on similar cylindrically-focused concave arrays have further been developed (Fig. 4), outperforming linear-array-based optoacoustic imaging in terms of quantification performance and image quality [86, 93].

2.5. Volumetric 4D and 5D imaging

The capability for real-time imaging introduced through the development of cross-sectional (2D) imaging systems represents a central milestone in dynamic optoacoustic imaging, yet does not address the requirement by many applications for rapid imaging across entire volumes. Cross-sectional imaging also has some associated drawbacks, like the need for focusing along the elevational dimension, which is responsible for highly anisotropic resolution on all axes and other artifacts associated with out-of-plane signals [95, 96]. It has been long recognized that the most efficient implementation of optoacoustic imaging implies simultaneous collection of time-resolved signals in 3D from as many locations (projections) around the imaged object as possible, thus avoiding limited-view effects and attaining excellent image quality [71]. Thereby, attempts to achieve high fidelity volumetric imaging were based on rotating (scanning) a set of unfocused detectors or sparse spherical detection arrays around the imaged object so that signals at a large number of locations are acquired for optimal 3D tomographic reconstruction [71, 74].

However, these scanning-based approaches hindered imaging of fast biological processes and were prone to image artifacts caused by *in vivo* motion, e.g. breathing or heartbeat. In response, four-dimensional (4D) optoacoustic tomography approaches have been recently developed that employ matrix arrays with a large number of unfocused detection elements distributed on a spherical aperture [97–99]. This configuration, having relatively large and densely-packed detection elements, further ensures optimal signal-to-noise ratio performance and ability to collect high quality real-time volumetric data for each illumination pulse without signal averaging (Fig. 5a). Furthermore, the particular orientation of the detection elements provides good sensitivity in the imaged region of interest located around the geometric centre of the spherical detection geometry. The 4D optoacoustic imaging approach has enabled tracking of contrast agent perfusion in entire organs [97], beat-by-beat imaging of fast beating murine heart [100] or monitoring the distribution of epileptic seizures in whole mouse brains [101]. The same configuration is further suitable for handheld operation mode, and human angiographic imaging at centimetre-scale depths was demonstrated attaining nearly isotropic spatial resolution on the order of 200 μm [102]. Hybrid combination of 4D optoacoustic and ultrasound imaging was further showcased by introducing passive absorbing elements [103].

Imaging across multiple spatial and temporal scales can be achieved by scanning the spherical array along a helical trajectory, a technique termed spiral volumetric optoacoustic tomography (SVOT) [73,104]. *In vivo* experiments in mice demonstrated a wide range of dynamic imaging capabilities for this method, from 3D high-frame-rate visualization of moving organs and contrast agent kinetics in selected areas to whole-body longitudinal studies with unprecedented image quality (Fig. 5b). The particular ability to deliver high resolution images at the whole-body scale while preserving ultrafast 3D imaging capability in smaller regions with the same type of contrast makes the SVOT technique unique among the existing pre-clinical imaging modalities.

In general, the biological information provided by optoacoustic imaging systems is encoded in five independent dimensions, namely, the three spatial dimensions, time and the optical excitation spectrum (wavelength). Multi-spectral 3D imaging is possible if a tunable laser or multiple laser sources operating at different wavelengths are used, while the temporal information can further be conveyed by subsequent acquisitions of the multi-spectral volumetric recordings. Recently, fast multi-spectral imaging capacity has been enabled with the introduction of fast-tunable lasers capable of facilitating real-time multispectral 3D imaging [11], all the five imaging dimensions can be simultaneously accessed (Fig. 6).

The effective multi-spectral imaging frame rate is determined by the pulse repetition rate of the laser and the number of wavelengths considered. State-of-the-art five-dimensional (5D) optoacoustic systems support acquisition of spectrally-enriched 3D information at a volumetric frame rate of 20Hz (considering imaging with five different wavelengths), providing unprecedented capabilities for imaging *in vivo* functional and molecular dynamics, also in a handheld configuration suitable for clinical application [105, 106].

It should be noted that 5D data acquisition can be compromised due to presence of significant motion between images acquired at the different wavelengths, e.g. due to

heartbeat, fast perfusion, or when operating the scanner in a handheld mode. To mitigate this problem, one may attempt using higher laser pulse repetition rates, which however may not be feasible due to data acquisition limitations or the safety limits on the average power exposure. An alternative solution consists in using multiple laser sources in a burst mode with a delay of a few microseconds [107]. The later approach enables functional optoacoustic imaging in the presence of very fast motion of up to 2 m/s maintaining relatively low laser pulse repetition frequencies so that the maximum permissible laser exposure levels are not exceeded.

Overall, the capacity to perform simultaneous imaging along all five dimensions comprises a unique enabling feature of the optoacoustic modality, poised to offer new insights into the workings of living organisms, particularly at the functional and molecular levels, as also elaborated in section 4 of this review.

3. Dynamic contrast enhancement approaches

Parallel to the rapid technological developments, substantial efforts have been devoted to the engineering and optimization of functional and molecular contrast agents for optoacoustic imaging. In general, the optical absorption mechanism underlying optoacoustic signal generation offers high versatility in mapping the distribution of endogenous or exogenous light absorbing substances and excellent reviews covering optoacoustic contrast agents are available [12, 18, 108–112]. Rather than distinguishing the agents based on their static chemical composition, herein we classify the contrast enhancement approaches according to the particular delivery method used, *in vivo* kinetics and biodistribution, as well as dynamic contrast modulation and molecular sensing properties.

3.1. Bio-marker delivery methods

3.1.1. Endogenous chromophores—Biological tissues contain a variety of endogenous chromophores with distinct absorption spectra that can be exploited for label-free structural and functional imaging with optoacoustics. In the visible and NIR ranges, light is mainly absorbed in living mammalian tissues by haemoglobin, melanin, lipids and water (Fig. 7). Differences in the absorption spectrum of haemoglobin associated to oxygen binding encode important information related to physiological activity. Since many diseases undergo structural changes at time scales ranging from days to weeks and months, imaging can be used to visualize and quantify these changes. For example, vascular structures can be mapped for depths of millimetres to centimetres within mammalian tissues [13] and accurate estimation of oxygen saturation is possible with proper models of light attenuation [113]. Due to the strong intrinsic haemoglobin contrast, optoacoustics represents a valuable tool to study the evolution of important hallmarks of cancer such as angiogenesis [53, 114] and hypermetabolism [115, 116]. Imaging the vascular fat deposition in atherosclerotic plaques is also possible at infrared wavelengths [117, 118], while the strong absorption of melanin can be exploited to characterize skin melanomas [49] and metastatic melanoma cells [106]. Measurable endogenous changes may also occur on significantly shorter time scales. For example, neuronal activity leads to complex hemodynamic responses in the brain via neurovascular coupling. Changes in blood oxygen saturation, total haemoglobin, blood

volume, oxygenized and deoxygenized forms of haemoglobin can be readily monitored with optoacoustic systems operating at sub-second temporal resolutions [119–121].

Note that the presence of strong endogenous (background) contrast may on the other hand represent a problem when considering enhancing the contrast extrinsically as carried out in molecular imaging applications. With a typical 2 mM concentration of haemoglobin in blood [128], vascular structures may conceal e.g. signals from genetically-expressed labels that can typically attain in vivo concentrations only in the order of μM, even at high expression levels [129]. Thereby, signal amplification approaches based on multispectral unmixing or dynamic contrast enhancement become essential in order to efficiently map the distribution of relatively low concentrations of contrast agents [87, 130]. Background absorption along with optical scattering are also responsible for the strong attenuation of light in biological tissues. Optical attenuation is significantly stronger as compared with acoustic attenuation for frequencies below 20–30 MHz, thus it represents the main limiting factor for deep tissue imaging [39]. Light penetration is maximized in the so-called near-infrared (NIR) window between 650 and 1350 nm [127], while it is significantly aggravated by strong absorption of blood at shorter wavelengths and water at longer wavelengths (Fig. 7). For deep-tissue imaging purposes, excitation optical wavelengths within this range are therefore commonly selected, where optoacoustic imaging with centimetre-scale penetration and beyond is enabled [102, 131]. The wavelength dependence of optical attenuation further contributes to the distortion (spectral colouring) of the optoacoustic signals originating from deep locations [132]. Thereby, the performance of the particularly employed unmixing approach, rather than the signal-to-noise performance of the imaging system, generally determines the minimum detectable concentration of extrinsically administered contrast agents.

3.1.2. Intravenous injection—Intravenous injection is the most common approach to administer probes for enhancing the absorption-based contrast. Ideally, exogenous contrast agents optimized for deep tissue *in vivo* optoacoustic imaging use should have 1) high absorption per molar concentration or per unit mass, preferably in the NIR window; 2) sharply peaked absorption spectrum or other distinctive features enabling unambiguous differentiation from background absorption; 3) high photostability under biologically relevant energy levels of the excitation light and 4) low toxicity and viable clearance from the body. Other desirable features are application-dependent. For example, exogenous probes can greatly enhance optoacoustic contrast, particularly in the NIR window, where the relatively weak absorption of haemoglobin hampers visibility of deep-seated vasculature. The highest contrast enhancement is achieved a few seconds after the intravenous injection, when the local concentration of the undiluted bolus is maximal [11]. A real-time optoacoustic imaging system is needed to accurately capture such perfusion transients [85, 97]. For unspecific vascular or organ perfusion studies, agents with rapid renal clearance are then preferable as this generally guarantees low toxicity. However, targeted agents are less likely to be delivered to the target tissue or cells if they are rapidly cleared, and a longer circulation time is desirable. The latter is affected by different physicochemical properties, such as the size, shape, chemical composition or surface modifications of the injected molecules or particles. The size or, alternatively, the hydrodynamic diameter (HD) is a

parameter of particular relevance as it directly influences the clearance mechanism. For example, ~6 nm is a known threshold for efficient renal clearance [133]. The circulation time for several optoacoustic contrast agents of different HDs is shown in Fig. 8a. Fig. 8b shows an example of the clearance of a small-molecule-based agent (Alexa-Fluor 750) through the renal system as visualized with SVOT. The size of the agent is also important to overcome important circulatory barriers. For instance, capillary pores in normal tissues have typical apertures of 5–10 nm, thus generally only small molecules are able to extravasate healthy vessels [134]. Even more restrictive is the blood brain barrier (BBB), which enables only the passage of molecules smaller than 400 Da (<1 nm) with high lipid solubility [135]. Permeability is enhanced in leaky neovasculature associated with several diseases, where larger fenestrations in the capillaries allow the passage of agents up to approximately ~100 nm in diameter [136].

Two distinct types of compounds used as extrinsically administered optoacoustic contrast agents are small-molecule dyes and nanoparticles. Many commercially-available biocompatible dyes, such as cyanine, squaraine, porphyrin derivatives, or boron-dipyrromethene (BODIPY) analogues, have been shown to absorb light at visible and NIR wavelengths [141]. Due to their small size (~1 nm), they can be fully and rapidly cleared from the body [138]. In fact, a number of organic dyes are FDA-approved and can be readily used in clinical trials involving optoacoustic imaging. These include methylene blue (absorption peak at ~664 nm) [142], Evans blue (absorption peak at ~620 nm) [143] and Indocyanine green (ICG, absorption peak at ~808 nm in plasma) [106]. Their small size and biocompatibility makes organic dyes adequate for extravascular and intracellular targeting [144]. Many dyes are also fluorescent and hence suitable for multimodal fluorescence-optoacoustic imaging. Note that fluorescence is optimized either with a high extinction coefficient ε or a high quantum yield QY, whereas the optoacoustic signal intensity is proportional to $\varepsilon(1-QY)$. As a result, high extinction coefficient benefits both modalities whereas high quantum yield is less optimal for optoacoustic imaging. In fact, most organic fluorescent dyes, especially those with peak absorption in the NIR, usually have a low QY, making them highly suitable for constrast-enhanced optoacoustic imaging. On the other hand, small-molecule dyes have a relatively low molar extinction coefficient (Fig. 9a) and many of them suffer from high plasma protein binding and undesired aggregation [141], which prevents rapid renal clearance.

To date, a myriad of different nanoparticles (NPs) have been used as optoacoustic contrast agents [146–151]. NPs refer to any structure with a size from 1 up to hundreds of nanometres that behaves as a unit. NPs have several advantages over small-molecule-based contrast agents. For example, their size, shape and chemical composition influence their functional properties and can be tailored according to specific needs [12]. Due to prolonged circulation time, NPs smaller than 100 nm are particularly suitable for passive targeting based on enhanced permeability and retention (EPR) [152]. Furthermore, their large surface allows attaching a large number of targeting moieties, thus increasing efficiency of binding to specific receptors. Some types of NPs can be further loaded with drugs or provide photothermal properties to be used as theranostic agents [153]. NPs provide significantly higher absorption per unit particle as compared with small-molecule dyes, although the absorption per mass is generally similar (Fig. 9a). Also important is the fact that the

optoacoustic signal generation mechanism in NPs is significantly affected by the heat propagation rate to the surrounding medium. Thereby, the relative optoacoustic signal intensities generated by different NPs can significantly differ from the corresponding relative optical absorbances (Figs. 9a and 9b).

Biocompatible NPs are classified into organic and inorganic compounds based on their chemical composition [146, 148, 149] and into plasmonic and non-plasmonic particles based on the optical absorption mechanism [109, 110, 112]. Organic NPs are composed of organic molecules grouped together in nanostructures or combined through chemical bonds. For example, organic dyes can be encapsulated in nanodroplets [154], liposomes [155] or virus-mimicking nano-constructs [156]. These nanostructures generally provide improved photostability and prolonged circulation time with respect to the free dyes [110]. Self-quenching effects can also be produced when fluorescent molecules are clustered, which can enhance the generated optoacoustic signal [157]. On the other hand, aggregation of fluorescent molecules was reported to induce widening of the absorption spectrum towards the NIR region [158]. Another type of organic nanoparticles are semiconductor polymer nanoparticles (SPNs) [159]. Recently, a new class of NIR SPNs has been shown to outperform highly-absorbing inorganic nanoparticles in terms of optoacoustic signal per unit mass (Fig. 9b) whilst providing high photostability [145]. Light absorbing porphyrin-lipid building blocks can self-assemble to form nano-vesicle structures (porphysomes) that can generate optoacoustic signals [160]. Other examples of organic NPs consisting e.g. of cellulose [161] or melanin [162, 163] have been also shown to create usable optoacoustic contrast.

Plasmonic particles are a particularly favourable type of NPs as they are known to generate the strongest optoacoustic signal on a per particle basis [12]. The surface plasmon resonance (SPR) effect in nobel metal NPs (e.g. gold or silver) enables strong and tunable optical absorption that is four to six orders of magnitude higher than that of single organic molecules [164]. Although silver NPs have been used as optoacoustic contrast agents [165, 166], gold NPs are considered preferable for *in vivo* optoacoustic imaging due to their better wavelength tunability properties and supposedly lower toxicity [167, 168]. The absorption spectrum of gold NPs can be tuned by controlling their size and shape during synthesis [169, 170]. Apart from standard nanospheres [171] and nanorods [139, 172], more complex gold NPs, such as nanocages [173, 174], nanoshells [175, 176], nanostars [177, 178], nanoprisms [179, 180] or nanovesicles [181], have been explored as optoacoustic contrast agents. Another key advantage of gold NPs is the ability to chemically modify their surface in order to achieve better biocompatibility and functionalization properties [182].

Another major type of inorganic NPs is based on different carbon-based structures, e.g. carbon nanotubes, graphene nanomaterials and nanodiamonds. Single-walled carbon nanotubes (SWNT) are the most widespread carbon NPs [183–185], with diameters of 1–3 nm and variable lengths, from nanometers to millimetres or even centimetres. They absorb light over a very broad spectrum and are also able to provide thermoacoustic contrast for electromagnetic waves in the GHz range [186], although the per-particle optoacoustic signal strength is lower in SWNT than in gold NPs (Fig. 9b). NIR dyes or a thin layer of gold can be attached to their surface to enhance the generated optoacoustic responses and make the

absorption spectra more distinct [187–189]. Other moieties can also be conjugated to SWNT for active molecular and cellular targeting [190–192]. Graphene- and graphene-oxide-based nanosheets have also been used as optoacoustic contrast agents [193–195], demonstrating better dispersibility in biological systems [108]. Carbon nanodiamonds are also efficient light absorbers. By introducing neutral vacancies into their crystal lattice, an even higher optoacoustic signal than for gold NPs or SWNT can be generated for a similar particle size [196].

Other types of inorganic NPs have been used as optoacoustic contrast agents. In particular, nanostructures providing high absorption in the NIR range include copper sulphide NPs [197–199], palladium nanosheets [200] or upconversion NPs [201–203]. Quantum dots are semiconductor nanocrystals with excellent fluorescence brightness that can also be used as optoacoustic contrast agents [204, 205], while carbon dots further represent a less toxic alternative with similar absorption characteristics [206]. Many NPs originally designed for non-optical imaging modalities may still have prominent light absorption properties, suggesting their use as multimodal contrast agents. Superparamagnetic iron oxide NPs are FDA-approved MRI contrast agents that were explored as standalone or combined agents in molecular optoacoustic imaging [207–210]. Microbubbles used in ultrasonography may additionally incorporate absorbing agents to change their optoacoustic contrast [211–215]. Porphysomes can further encapsulate fluorinated gases to be used as multimodal contrast agents for optoacoustics, fluorescence and ultrasound [216]. Similarly, encapsulation of gold NPs in liposomal or other types of nanostructures paves the way for devising contrast agents with multimodal and theranostic properties [217].

3.1.3. Interstitial delivery—Despite the general prevalence of the intravenous delivery methods, many probes are unable to reach the target when administered into the blood circulation, regardless of the level of chemical affinity. Depending on the investigated disease model or organ of interest, alternative administration routes may include subcutaneous, intratumoral or intracranial injections. The latter is important in brain imaging applications to label neurons or other cells that are otherwise unreachable with intravenous administration due to the high restrictiveness of the BBB [218]. The BBB can be overcome via an invasive procedure in which a small hole is drilled into the skull. By slowly inserting a small diameter injection needle or a pulled glass capillary (with tip-diameters of around 10–20 μm), contrast agents can be directly injected into the brain region of interest [219]. The main limitation of intracranial injections is the small volume that can be delivered (usually less than 1 μl in mice). Distribution of the probes into the brain tissue occurs only by diffusion. Thereby, the labelled or affected area may remain rather limited [220]. On the other hand, the injected probes have a very slow clearance rate, which enables longer effective imaging windows. Other less invasive methodologies have been reported for the purpose of temporary BBB disruption, e.g. burst-mode focused ultrasound [221].

Interstitial delivery has also been used in the field of cancer research, where the incompetent tumor vasculature often impedes efficient intravenous delivery of therapeutic and imaging agents. Intratumoral injection can be done by delivering the probe directly into the tumor microenvironment e.g. for targeted imaging or treatment monitoring purposes [222, 223]. In addition, subcutaneous or intradermal injections of contrast agents can be of interest for

imaging lymphatic vessels and nodes. For instance, the FDA-approved ICG dye has been shown to improve sentinel lymph node biopsy of axillary lymph nodes in a rat model [224]. A theranostic agent consisting of encapsulated conjugated oligomer nanoparticles was shown to accumulate in the sentinel lymph node after intradermal injection in the forepaw pad of a mouse, allowing for an accurate delineation of the lymph node margins [225]. Contrast-enhanced optoacoustic imaging of lymphatic vessels has also been performed after injection of Evans blue in the mouse tail [226]. MSOT in combination with a subcutaneous injection of ICG has proven to be valuable for the diagnosis of the metastatic state of sentinel lymph nodes in human melanomas [106], representing a promising clinical application of the method.

3.1.4. Genetic reporters—Genetically-encoded expression provides arguably the most versatile approach for specific labeling of cells within a living organism [3]. Reporter genes enable optoacoustic detection and quantification of gene expression by either coding for light absorbing proteins or for enzymes that convert clear substrates into chromophoric products. Since fluorescent substances undergo photothermal conversion in non-radiative relaxations, highly-optimized fluorescent proteins (FP) can further provide optoacoustic contrast (Fig. 10a). The initial feasibility to image FPs with optoacoustics has been demonstrated with small organisms such as Drosophila pupa or adult zebrafish expressing proteins from the family of the green fluorescent protein (GFP) [59]. However, the peak absorption of the GFP-based FPs has been so far only shifted to a maximum wavelength of 611 nm [227], hence their application in mammal organisms is still hampered by the high background haemoglobin absorption at wavelengths below 650 nm (Fig. 7). More recently, far-red- and NIR-shifted fluorescent proteins have been engineered to provide peak absorption above 680 nm [228]. In particular, the infra-red fluorescent proteins (iRFP) are derived from bacterial phytochromes [229]. In contrast to GFP, which only requires oxygen for chromophore maturation, phytochrome-derived proteins incorporate biliverdin as the chromophore. Optoacoustic detection of iRFP has been demonstrated in living mice [129, 230] and further validated against fluorescent measurements [19]. Due to their limited optoacoustic generation efficiency, detection of iRFPs has only been reported at shallow depths of several millimetres. Specifically-designed screening platforms are being used to optimize the performance of existing FPs and chromoproteins [231], facilitating the engineering of novel genetic reporters for optoacoustic imaging and sensing [232].

Enzymatic reporter genes have also been explored as a means for generating optical absorption contrast (Figs. 10b–d). This approach was first demonstrated by imaging expression of the *lacZ* gene [233], which encodes β-galactosidase converting 5-bromo-4-chloro-3-indolyl-b-D-galactoside (X-gal) into galactose and the stable insoluble blue product 5,5′-dibromo-4,4′-dichloro-indigo (Fig. 10b). This highly absorbing product was shown to generate a measurable optoacoustic signal at centimetre-scale depths within *ex vivo* biological tissues [234].

However, its *in vivo* use is limited due to toxicity associated with administration of the X-gal chromogenic substrate, which may cause skin irritation and inflammation in rodents. The most widely employed enzymatic reporter for generating optoacoustic contrast is tyrosinase (*Tyr*) (Fig. 10c), a key enzyme in melanogenesis [235]. *Tyr* alone is sufficient for producing

melanin in non-melanogenic cells from tyrosine without necessitating an extrinsic agent [236]. The tyrosinase homologue *melA* that produces melanin in bacteria has also been suggested [237]. Indeed, melanin is a dark and strongly absorbing pigment easily detectable with optoacoustic imaging systems. Melanin can further provide contrast in other modalities such as magnetic resonance imaging (MRI) [235, 238] or positron emission tomography (PET) [239] and has also been suggested as a potential thermal therapy agent [235]. Yet, its relatively flat absorption spectrum makes it difficult to distinguish from blood via spectral unmixing [240]. In addition, although it has been possible to monitor the growth of *Tyr*-expressing tumours over periods of several weeks [241], extensive melanin production is generally associated with increased cytotoxicity [242]. A viable alternative is the tetracycline-regulated inducible system, which further enables versatile control of gene expression [243, 244]. Another promising enzymatic product that can generate optoacoustic signals is the bacterial pigment Violacein [245], which results from the multi-enzyme-based oxidation pathway of L-tryptophan (Fig. 10d). The particular benefits of Violacein are its good photobleaching resistance and the highly distinct absorption spectrum extending above 650 nm [245]. In general, enzymatic reporter genes benefit from inherent signal amplification as each genetically-expressed enzyme can generate multiple products. On the other hand, quantification of gene expression may be hindered by dependence on the availability of the substrate.

3.2 Sensing mechanisms

Optoacoustic contrast agents can be designed to perform specific dynamic sensing tasks e.g. by altering their absorption properties in response to variations in physiological environment or due to binding to a certain molecular target. In fact, haemoglobin is an exogenously present optoacoustic sensor whose absorption spectrum is altered due to the oxygen binding, The heme group of the molecule undergoes conformational changes when oxygen binds to iron (Fig. 11a). Haemoglobin is thus frequently used as a powerful label-free optoacoustic sensing mechanism in brain imaging or cancer research.

Optoacoustic sensing of tissue hypoxia has been reported using methylene blue, whose lifetime is highly sensitive to the oxygen partial pressure [142]. The acidic pH is another important microenvironmental parameter that increases the potential of tumour migration and invasion, hampering efficacy of many drugs [246]. Optoacoustic sensing of pH was first suggested with the fluorescent pH indicator dye seminaphthrorhodafluors-5F [247, 248]. Recently, other optoacoustic pH sensors e.g. based on micelles [249], liposomes [250], self-assembled nanoprobes [251], semiconducting oligomer nanoparticles [252], dextran-based nanoprobes [253] or gold nanoparticles [254] have been developed.

Reporter genes can also be turned into powerful environmental sensors to deliver information on the presence and concentration of certain compounds in real time. GCaMP proteins are genetically encoded calcium indicators (GECIs) that undergo conformational changes when calcium is present (Fig. 11b). GCaMP was shown to exhibit optoacoustically measurable variations in its extinction coefficient due to the influx of calcium ions into neurons [255]. The calcium-sensitive dye Arsenazo III has also been used to detect calcium concentration changes in other types of cells [256].

The temperature dependency of the Grüneisen parameter affects the optoacoustic generation efficiency. Hence, any endogenous or exogenous chromophore can potentially serve as a thermal sensor. Measuring temperature variations is relevant for the understanding of many biological processes. For example, cellular division, enzymatic reactions or gene expression are typically associated to intracellular temperature changes that can be monitored with optoacoustic microscopy [257, 258].

Other types of optoacoustic sensing approaches have been reported. Protease-mediated fluorescent dyes are smart labels that can sense disease-related processes in cancer, rheumathoid arthritis or cardiovascular diseases. The commercially available MMPSense 680 probe, which is activated by metalloproteinases (MMPs), has shown promise in molecular optoacoustic imaging [259]. Smart probes based on activatable peptides attached to NIR chromophores can be tailored to target specific proteases and have shown to provide optoacoustic molecular sensing capacity [260, 261]. Reactive oxygen species can also be detected with semiconducting polymer nanoparticles [145]. Other examples are sensors of hyaluronidase [262] or copper (II) [263].

3.3 Contrast modulation approaches—Contrast modulation approaches are based on contrast agents whose optoacoustic signal generation is susceptible to external manipulation of the sample. Generally, it is preferable that the induced signal variations are reversible, although irreversible changes can still be used. Dynamic changes in the optoacoustic contrast can be exploited in order to enhance detection sensitivity of specific probes by removing contributions from time-invariant background absorbers. A number of approaches for optoacoustic contrast modulation exist. As mentioned above, optoacoustic signals are temperature dependent. Thus, the signal amplitude can be modulated by changing the temperature in the sample. This effect has been exploited for non-invasive temperature monitoring in clinical procedures involving radiofrequency ablation [264], high-intensity focused ultrasound (HIFU) [265], cryoablation [266] or laser-induced thermotherapy (LITT) [267]. At the microscopic level, temperature changes in individual cells can be measured with an accuracy of 0.2°C [257]. In principle, no exogenous agents are required for optoacoustic temperature mapping, although specifically-engineered probes with enhanced temperature sensitivity are also available, e.g. silica-coated gold nanorods [268]. Moreover, the absorption spectrum of the ordered Bchl-lipid dye aggregates can be reversibly switched by exceeding a certain temperature threshold [269].

Optoacoustic contrast can also be modulated with light. It was previously shown that pulsed light radiation may cause photobleaching of fluorescent probes and other photodegradation mechanisms for energy levels below safety standards [270]. Even though these effects are generally considered detrimental, they can be exploited for enhancing the resolution and contrast in optoacoustic microscopy by considering the signal difference before and after photodegradation [34]. Optoacoustic signal recovery after bleaching can be measured on a slower time scale, providing a better understanding of cellular dynamics [271].

Reversibly photoswitchable FPs are yet another versatile contrast modulation tool that involves no permanent photodegradation. The fluorescent protein Dronpa can be switched with light at different wavelengths between a *cis* conformation and a *trans* conformation

having different absorption spectra (Fig. 11c). Detection sensitivity can be greatly enhanced with this kind of probes by identifying the changes in the optoacoustic signal strength for the activated and deactivated states [130, 272]. This can be done by inducing time-varying optoacoustic responses, which can be temporally-unmixed from the time-invariant (constant) background absorption [130]. Furthermore, the optoacoustic signal decay rate is generally proportional to the local light fluence, a property that can be explored for estimating the light fluence distribution with photoswitchable agents [273]. Non-fluorescent particles have also been suggested as photoswitchable probes [274]. Optoacoustic contrast can be further modulated with a combination of pump and probe laser pulses. This approach was first suggested to capture transient optical absorption during the triplet state microsecond-level lifetime of methylene blue [275]. By using shorter delays between the pump and probe beams, the optoacoustic signal generated by fluorophores can be modulated due to stimulated emission [276].

Another promising source of energy for optoacoustic signal modulation is ultrasound. In particular, microbubbles and nanodroplets can be manipulated with ultrasound fields, leading to optoacoustic signal changes. It has been shown that the optoacoustic signal generated by microbubbles in a methylene blue solution is lower than that generated by the same concentration of bubble-free dye. Signal enhancement is thus achieved by bursting the microbubbles [214]. In addition, the signal generated by plasmonic particles conjugated to microbubbles is enhanced with respect to the unconjugated mixture or free nanoparticles [215, 277]. Reversible phase transitions can be also induced in a nanoemulsion of perfluorohexane droplets coated with gold nanospheres by combining light and ultrasound pulses [278, 279], which leads to an enhanced signal as compared laser-only excitation.

3.4 Photostability and toxicity

When selecting appropriate contrast agents for optoacoustic imaging, effects related to their photostability under pulsed nanosecond radiation, irreversible bleaching as well as *in vivo* toxicity have to be carefully considered. The light pulses employed in optoacoustic imaging induce photobleaching effects that considerably differ from those known from fluorescence imaging using single- or multi-photon microscopes [270, 280]. It has also been long recognized that pulsed laser radiation has different biological effects from those observed under continuous wave exposure [281]. For example, effects related to photochemical destruction and melting under nanosecond laser radiation have been reported for inorganic nanoparticles [282]. Shape alterations of gold NPs induced by prolonged nanosecond light exposure may lead to optoacoustic signal degradation [283]. In this regard, SWNT have significantly higher photostability than gold NPs [12] and SPNs can even outperform SWNT in long-lasting optoacoustic signal generation [145] (Fig. 12a). Many FPs are known for their lack of photostability, which can be seen in effects like dark states, blinking, transient absorption and photobleaching [284]. Furthermore, FPs are known to induce phototoxicity under certain excitation conditions [285]. While most of these effects are yet unexplored for realistic *in vivo* imaging conditions, optoacoustic signal degradation associated to photobleaching effects in FPs has already been observed under different imaging settings [270, 280] (Fig. 12b). Photobleaching may even take place for safe excitation energy levels [270] (Fig. 12c). Of particular interest are non-fluorescent chromoproteins or enzymatically-

amplified chromophores, which in comparison to FPs exhibit a higher optoacoustic efficiency due to the absence of radiative relaxation and ground state depopulation, and also higher photostability [245, 280].

The use of exogenous contrast agents, especially inorganic NPs, is also associated with a number of biocompatibility, cytotoxicity and long term accumulation issues. The relatively large size of most NPs prevents efficient renal clearance. Instead, they are generally taken up by the reticuloendothelial system (RES) and thus may accumulate in the body for long periods of time [138]. Many types of particles are also non-biodegradable with their potential toxicity effects remaining unknown. For example, severe long term toxicity concerns exist for SWNT [286], although it has been shown that they may be cleared through the kidneys due to their high aspect ratio [140]. On the other hand, a number of studies further support the low toxicity of carbon nanodiamonds [287, 288]. Surface coating e.g. with a silica layer is known to enhance photostability and heat dissipation and hence optoacoustic signal amplitudes [20, 289]. Furthermore, evidence exists that gold NPs accumulate in the RES and thus their long term toxicity remains a potential concern [290]. An exception to this are biodegradable nanoclusters encapsulating small (~5nm) gold NPs [291], which can be cleared through the kidneys.

4 Applications enabled by optoacoustic visualization of multiscale dynamics

Recent advances in optoacoustic imaging and sensing methods and in associated approaches have been accompanied by the advent of biomedical applications that benefit from the advantages of state-of-the-art systems, particularly for imaging dynamics. In this section, we survey novel applications involving imaging of multiscale dynamics.

4.1 Cell tracking

Tracking individual cells is important for understanding their longitudinal behaviour and response under different physiological and pathological conditions. For example, detecting and tracking the fate of circulating tumor cells *in vivo* is essential for early detection of metastatic spread, facilitating cancer treatment. Quantifying the vascular flow of blood cells is important for identification of microcirculation irregularities associated with cancer, diabetes or other conditions.

Optoacoustic detection of circulating tumor cells labelled with magnetic nanoparticles was demonstrated using and external magnetic field [294]. Magnetic trapping was shown feasible for flow velocities up to 5 cm/s, so that it may represent a promising approach for microsurgical extraction or laser ablation of these cells. Cell trapping has also been achieved with gradient acoustic forces induced by ultrasound and optoacoustic waves [292] (Fig. 13a). The motion of a population of blood cells can be characterized with optoacoustic Doppler velocimetry by analysing the correlation of single optoacoustic signals generated by two laser pulses with a millisecond-level delay [293] (Fig. 13b). A relatively low concentration of cells is essential for accurate estimations with this method, although velocity measurements in whole blood have been achieved under certain conditions [295].

Individual optoacoustic signals may further contain information on cell morphology. Irregular shapes of red blood cells were identified by analysing the frequency content of individual optoacoustic signals [296]. Potentially, the same methodology can be applied for detection of other types of morphological abnormalities in red blood cells occurring e.g. in malaria or sickle cell disease.

Three-dimensional optoacoustic imaging of single cells in motion is challenged by the harsh requirements for superb sensitivity, spatial and temporal resolution. High-speed 2D imaging with cellular resolution is possible with OR-PAM. Specifically, B-mode optoacoustic images could be obtained at a rate of 100 frames per second, which is sufficient to track the flow of red blood cells in capillaries [40]. This method has been used to analyse the microcirculation in cuticle capillaries. By using dual-wavelength excitation, it was possible to detect changes in oxygen saturation in flowing individual red blood cells [41] (Fig. 13c), which can shed light on the process of oxygen delivery to tissues in microvascular structures. Volumetric tracking of flowing particles in real time has also been achieved with four dimensional optoacoustic tomography [297], which holds potential for *in vivo* applicability with properly labeled cells.

4.2 Perfusion and organ function

Organ support and maintenance is a complex and intricate process which crucially relies upon their blood supply. Blood constitutes an excellent endogenous contrast for optoacoustics due to its photostability and well-characterized dependence of its absorption spectrum on oxygen saturation. Thus, optoacoustics is clearly a highly suitable imaging technique for the characterization of organ perfusion, providing high spatial and temporal resolution for interrogation of vascular structures at different scales.

Dynamic label-free optoacoustic imaging of blood perfusion in subdermal vessels has been carried out completely non-invasively. In particular, the ability to image perfusion of blood flow in subdermal capillaries across a wide field of view and down to the resolution of single cells has been demonstrated [24] (Fig. 14a). At the macroscopic level, restriction of blood supply in ischemic lesions was characterized along with the consequent changes in blood volume and oxygen saturation [298–300]. Combined with other imaging modalities, optoacoustics can further serve as a complementary tool to characterize blood flow [301].

Optoacoustic imaging of organ perfusion can be greatly enhanced by using contrast agents. For instance, perfusion of Evans blue was also used to characterize the functional state of capillaries early after the first developments in OR-PAM [143]. Video-rate visualization of kidney perfusion by intravenous injection of ICG was among the first application demonstrated with cross-sectional real-time MSOT systems [85]. By using multiple light wavelengths spanning between 750 and 900 nm, the ICG distribution could be efficiently unmixed from the background blood signal in the entire kidney region and over time. In a follow-up study, the capacity to image blood vessels, the kidneys, the liver and the gall bladder with 150 μm spatial resolution through entire mouse cross-sections was demonstrated [302]. The removal of ICG from the systemic circulation and its time-resolved uptake in the liver and gallbladder was characterized (Fig. 14b). Furthermore, it was possible to track the uptake of a carboxylate dye in separate regions of the kidneys. Alternatively,

negative contrast can also be used to visualize organ perfusion. A drop in the optoacoustic signal is generated by injecting a saline solution into organs, and the ensuing blood flow can then be readily visualised with the signal rapidly returning to its original level [303]. Arguably, the most complex challenge tackled in this area is imaging perfusion in the healthy or diseased heart in animal models, since this is a relatively large organ that moves at a high speed. Tackling this challenge using other whole-body tomographic imaging modalities necessitates gating the acquisitions but state-of-the-art high-frame-rate 4D optoacoustic imaging now enables imaging the heart in 3D on a beat-by-beat basis [100]. In this way, it was possible to visualize the flow of intravenously injected ICG from the right ventricle to the lungs and back into the left ventricle (Fig. 14c). Importantly, this image sequence provides an accurate measurement of the pulmonary transit time (PTT), a parameter that can serve as a functional indicator of ventricular dysfunction and which cannot be measured by other imaging methods relying on cardiac gating.

4.3 Neuroimaging

The massive prospects and opportunities for imaging central nervous system are only very partially addressed by existing neuroimaging methods despite decades of intense research and important advances. These methods either offer a very low spatio-temporal resolution or an extremely limited field of view and depth penetration. Current neuroimaging techniques suffer from additional major pitfalls: most rely on observing neural activity *indirectly* using effects mediated through complex neuro-vascular coupling processes that we are only beginning to truly understand, and they typically do not simultaneously assess all the relevant cerebral hemodynamic parameters. The vast advances in the development and application of optoacoustic imaging techniques now offers a viable alternative for dynamic high-resolution observations in the brain.

The endogenous optoacoustic contrast based on spectrally-distinct haemoglobin measurements provides a remarkable performance for label-free visualization of cerebral hemodynamics under different stimuli. OR-PAM enables assessing all the relevant cerebral hemodynamic parameters like oxygenated (HbO) and deoxygenated (HbR) haemoglobin, blood oxygenation (SO_2), total haemoglobin (HbT), cerebral blood flow (CBF) and, derived from these parameters, the oxygen extraction function (OEF) and the cerebral metabolic rate of oxygen ($CMRO_2$) [304]. The achievable spatial resolutions reach the capillary level and state-of-the-art systems offer temporal resolutions in the range of 100 kHz for 1D scans. The penetration depth is however limited to superficial cortical layers [22]. In one of its earliest embodiments, functional optoacoustic microscopy was able to provide an independent verification of the BOLD-fMRI ‘initial dip’ (Fig. 15a), demonstrating a decrease in blood oxygenation due to an increase in arteriole HbR in the first few 100s of milliseconds after an electrical paw stimulus [305].

While achieving adequate imaging performance with high-resolution OR-PAM normally necessitates removal of the scalp, tomographic systems such as those based on ring-shaped transducer arrays, are generally fully non-invasive and have been utilized to image resting state [121] (Fig. 15b) and stimulus-evoked [306] (Fig. 15c) brain activity. A 512-element full-ring ultrasonic transducer array with an in-plane resolution of 100 μm was used to

image glucose metabolism in the mouse cortex after intravenous injection of a glucose-analogue molecule providing optoacoustic contrast [306]. A lower resolution 64-element ring transducer array was used to image brain dynamics in awake, freely moving rats [307]. By directly mounting the array onto their head (with intact scalp and skull) longitudinal tracking of hemodynamic changes in a generalized epilepsy model was performed. Alternative real-time cross-sectional optoacoustic imaging systems were configured to acquire coronal sections of the brain of a mouse, which allows visualizing deep-seated structures [308].

As discussed above, the development of spherically-shaped transducer arrays with densely-packed elements has taken the tomographic concept a step further, allowing real-time recording of true 3D data. A 256-element detection array system, which can record data at rates up to 100 frames/s [119] and is capable of tuning the laser wavelength on a per-pulse basis, provides multispectral information for analysing hemodynamic changes deep inside the mouse brain. This has recently been demonstrated in a model of focal epilepsy in which the onset, spread and termination of 4-Aminopyridine-induced epileptic seizures were visualized, with concurrent electroencephalographic (EEG) recording of the aberrant neural activity [101] (Fig. 15d).

Notwithstanding this important progress in advanced hemodynamic imaging, modern neuroimaging work has largely steered towards the development and application of indicators that allow a much more *direct* monitoring of neuronal activity, most notably calcium- and voltage-sensitive indicators. Genetically encoded calcium indicators (GECIs), and primarily the GCaMP family of indicators have become the workhorse tool for visualizing distributed activity across neuronal populations. In a very recent study, functional optoacoustic neuro-tomography (FONT) has successfully demonstrated imaging of calcium-sensitive protein GCaMP5G expressed in a transgenic zebrafish model [255]. The study established a very strong correlation between the fluorescence and optoacoustic activity-dependent signals of the indicator. It was demonstrated in a generalized seizure-model that calcium neuronal dynamics recorded with optoacoustics could be analysed deep inside the scattering adult zebrafish brain. Conversely, these dynamics were not observable with concurrent fluorescence imaging, which rendered a blurry appearance lacking the depth information (Fig. 16).

4.4 Fast imaging based on photoswitchable probes

Several fluorescent proteins and organic dyes are known to change their photo-physical properties in response to optical excitation. For example, photoactivatable proteins can be activated from a non-fluorescent state and become fluorescent, while photoswitchable proteins can exhibit a change in their fluorescence emission and reversibly switchable proteins can be switched reversibly between a fluorescent and a non-fluorescent state. Photoswitchable probes play an essential role in super-resolution optical microscopy techniques such as photoactivation localization microscopy (PALM) or reversible saturable optical linear fluorescence transitions imaging (RESOLFT).

Detection of optoacoustic signal changes associated to activation and deactivation of photoswitchable probes was shown with the reversibly switchable FP Dronpa and its fast-

switching fatigue resistant variant Dronpa-M159T [130]. By using a systematic sequence of laser pulses at 420 and 488 nm, it was possible to dynamically modify the amount of activated molecules and hence generate specific temporal profiles in the corresponding sequence of images acquired with 4D optoacoustic tomography (Fig. 17a). These temporal profiles can be used to isolate (unmix) the signal generated by the probe so that it can be accurately mapped. The advantage of temporal unmixing in comparison to the more commonly-used spectral unmixing is that it can be inferred from a sequence of single-wavelength images, i.e., no spectral coloring effects are produced. Thereby, it is easy to distinguish the signals generated by the probe from the baseline signals (constant temporal background). Interestingly, the number of activated molecules decays exponentially as a function of time with the decay constant proportional to the local light fluence [273]. The measured decay rates thus enable an accurate estimation of the light fluence distribution, facilitating extraction of quantitative information on the chromophore concentration (Fig. 17b). Phytochromes exhibiting isomeric states have further been used as optoacoustic photoswitchable probes for NIR wavelengths [272, 310]. For example, the bacterial phytochrome BphP1 can be switched between two different states by light excitation at 630 and 780 nm. By calculating the difference between the images obtained for the two states, it was possible to detect BphP1-expressing U87 tumor cells at a depth of 8 mm with high sensitivity (Fig. 17c). Additionally, the reversible switching mechanism of BphP1 can be exploited for contrast enhancement in OR-PAM and to overcome the optical diffraction limit for super-resolution optoacoustic microscopy [272].

4.5 Molecular sensing

Optoacoustic imaging sensors are physical, chemical or biologically active probes that detect an environmental change and convert it into a signal or form of information which can be detected optoacoustically. This new layer of information can be readily coregistered with anatomical images to provide an accurate non-invasive mapping of distribution of molecular and functional markers *in vivo*.

Optoacoustic sensors have been used to probe tumour microenvironments and monitor treatments. A temperature sensitive nanoswitch probe was synthetized by intercalation of light-harvesting porphyrins within thermoresponsive nanovesicles [269]. The probe functions by absorbing light at two distinct wavelengths (680 and 824 nm) while its spectral features can be reversibly switched by exceeding a temperature threshold. Using this thermochromic property, localized temperature changes within tumour Xenografts were determined *in vivo* and non-invasively (Fig. 18a).

Similar strategies may be applied to detect other stimuli such as pH and enzymatic activity. Due to their high metabolic rate, malignant tumours are commonly characterised by lower than normal pH levels. A theranostic nanovehicle for targeting pancreatic cancer was designed based on mesoporous silica nanoparticles (MSN) that encapsulate Indocyanine Green for enhancing optoacoustic contrast [311]. The tumour specificity was improved with the addition of both chitosan, targeting acidic pH, and urokinase plasminogen activator (UPA), targeting UPAR. Accordingly, the signal increase due to acidic pH conditions resulted in a 20-fold stronger optoacoustic response. In vivo, MSN-UPA particles

demonstrated orthotopic pancreatic tumour specific accumulation compared to liver or kidney, as identified using real-time MSOT. By tracking *in vivo* nanoparticle biodistribution with MSOT, it was further confirmed that pH responsive, ligand targeted MSNs preferentially bind to pancreatic tumours for payload delivery (Fig. 18b).

Optoacoustic imaging has also been found capable of imaging oedema, whose different variants include cerebral, pulmonary, macular or lymphatic fluid build-ups within the body. One suitable probe for this is a nanoparticle based on semiconducting polymer particles (SPN1) [145]. It exhibits preferential narrowband absorption in the NIR and is resilient against photodegradation and oxidation. Most important is its ability to ratiometrically detect reactive oxygen species (ROS) at 700 and 820 nm (Fig. 18c). In fact, the increase in ROS has also been shown as a marker of apoptosis. In the same study, using a mouse model of acute oedema and Zymosan to simulate ROS generation, SNP1 was successfully used to monitor the ROS regulation process intra-muscularly.

Another promising application of dynamic optoacoustic molecular sensing is the monitoring of thyroid-related disorders. The thyroid gland regulates many of the most important functions of the body, from metabolism to breathing. Thyroid cancer is rare but benign nodules on the gland are common. Follicular thyroid carcinomas are very similar to benign nodules yet differ in terms of environmental conditions. One noticeable difference is the activity and presence of the matrix metalloproteinases (MMPs) and two members of this family (MMP-2 & MMP-9) were determined as biomarkers of malignant thyroid lesions. An MMP-activatable optoacoustic probe based on Alexa-Fluor 750 was successfully used to image FTC133 thyroid tumours subcutaneously implanted in nude mice *in vivo* [261]. Both MMP-2 & MMP-9 cleave the protein in a non-reversible fashion, which increases its optoacoustic and fluorescent signal.

4.6 Pharmacokinetic and bio-distribution analysis

The characterization of pharmacokinetic and biodistribution profiles is an essential step in the development process of new candidate drugs or imaging agents. In addition, targeted modifications of diagnostic and therapeutic probes can further facilitate selective probe delivery. The bio-distribution analysis is of particular importance in cancer research as angiogenesis and changes in vascular morphology significantly alter the probe uptake rates. The blood perfusion profiles are responsible for the establishment of multiple parameters within the tumour mass, such as hypoxic and nutrition gradients, cell viability, proliferation and drug response potentials. Tumour neovascularization typically exhibits leaky behaviour, which can be exploited for specific probe delivery. 4D and 5D optoacoustic tomography was reported to attain concurrent video-rate observations from entire tumour volumes [312]. Assisted with liposome particles encapsulating ICG (Lipo-ICG), simultaneous assessment of blood oxygenation gradients and vascularization in solid breast tumours was demonstrated further revealing different types of blood perfusion profiles *in-vivo*. The method greatly benefited from its ability for high resolution *in vivo* assessment of 3D maps of blood oxygenation in and around the tumours. In this way, vascular tracts of various sizes as well as less oxygenated areas within tumours could be efficiently resolved. Furthermore, analisys

of the perfusion kinetics of Lipo-ICG has allowed for an accurate classification of three different perfusion profiles in a subcutaneous tumour model of angiogenesis (Figs. 19a,b).

Solid nanoparticles are known to provide excellent optoacoustic contrast but can potentially induce toxicity. One way to improve their biocompatibility consists in wrapping a toxic compound into a biocompatible and non-toxic compound, such as poly(D, L-Lactide-co-glycolic acid) (PLGA), a biodegradable polymer commonly utilized for drug delivery. This however tends to change the kinetics and bio-distribution of the probe, so that whole-body small animal optoacoustic scanners are of great value for studying such novel constructs. A recent study explored the use of PLGA nanoparticles loaded with the 1,1′-dioctadecyltetramethyl indotricarbocyanine iodide (DiR) NIR-dye for optoacoustic contrast enhancement [313] (Fig. 19c). Differential kinetics and bio-distribution between an intravenous and intraperitoneal injection routes was studied. While in both cases the probe was taken up by the liver and spleen, a significantly higher amount was taken up into the spleen after intraperitoneal injection.

Surface modifications of nanoparticles may also assist in enhancing the optoacoustic contrast. For instance, in the case of gold nanorods, cellular uptake into the cells via endocytosis and high concentration in endosomes may lead to diminished optoacoustic signal intensities. However, a steric hindrance provided by silica coating of the nanorods leads to improved optoacoustic sensitivity [314]. In this study, the enhanced sensitivity allowed for monitoring labelled stem cells implanted into mice over 15 days with high spatial resolution, albeit dilutions of the nanorods in the cell cluster are produced with each cell division. The size of nanoparticles is an equally important parameter for determining the attained optoacoustic signal intensity. A particle size-dependent contrast enhancement effect was shown for copper sulfide nanoparticles with sizes between 3 and 7 nm [315]. While the *in vitro* contrast enhancement effect was proportional to the particle size, the latter has equally affected pharmacokinetics *in vivo*. After intravenous injection, copper sulfide nanoparticles smaller than 5 nm presented higher contrast enhancement, especially at the tumour boundaries.

In a different application, the thermoplastic expansion associated with the optoacoustic effect was used to destroy intracellular vesicles [316]. The idea behind this approach is to prevent unwanted intracellular vesicular compartmentalization of anticancer drugs in cancer cells, which may lead to chemoresistance of tumours. To achieve the disruption of vesicles, a folate-modified SWNT was first trapped inside acidic vesicles after entering lung cancer cells. Irradiation with NIR pulsed laser then led to optoacoustically-induced shockwaves that broke the vesicles, resulting in the release of anticancer drugs. A 12-fold enhancement of antitumor therapeutic efficacy in tumour-bearing mice was achieved.

4.7 Treatment monitoring

Optoacoustic imaging based on endogenous or exogenous contrast can be used in a great variety of treatment monitoring applications. For instance, using endogenous tissue contrast and the temperature-dependence of the optoacoustic signal, it was possible to dynamically monitor tissue ablation procedures. In endovenous laser therapy (ELT), elimination of incompetent truncal veins is achieved via intravenous laser coagulation leading to cell

destruction and collagen shrinkage, which was successfully monitored by 4D optoacoustics [267] (Fig. 20a). In this way, it was also possible to accurately follow the pull-back of the ablating laser catheter. Similarly, optoacoustics has also been used to monitor HIFU [265], and radiofrequency ablation [264], where multispectral imaging has also been used to identify spectral changes associated with tissue coagulation. Temperature monitoring during the cryoablation of a canine model of prostate cancer has been performed with an accuracy of 2°C for a temperature range from 35 to −15°C [266].

Endogenous haemoglobin optoacoustic contrast has also been used to follow up anti-angiogenic tumour therapy using acoustic-resolution optoacoustic microscopy. Here RNA silencing (siRNA) therapy was used to target tumour vasculature, whereas MSOT monitoring of the tumour response to anti-angiogenesis was done in a breast cancer mouse model [317] (Fig. 20b). The noninvasive imaging approach provided longitudinal monitoring of a successful therapy, seen e.g. by tumour shrinkage or reduced vessel density (over days to weeks).

Optoacoustics has also been used for monitoring brachytherapy in prostate cancer, which consists of implanting small sealed radiation sources, so-called seeds, inside or near the tumours. In this way, the radiation dose to cancerous tissue is maximized while sparing healthy tissue, yet factors such as seed migration, prostate motion, oedema, or implantation errors may lead to complications. In an *in vivo* canine study, seed locations were mapped with optoacoustic imaging using a transrectal ultrasound probe [318] (Fig. 20c). In this study, a new interstitial light delivery method and beamforming techniques were used to improve contrast from the metallic seeds. Another important diagnostic marker for cancer progression is the amount of cell death by tissue necrosis, which serves as a reliable indicator of rapid and aggressive tumour growth. In fact, some therapeutic approaches that are initially designed for inducing apoptosis may often result in the so-called secondary necrosis. An approach to assess the amount of necrosis during tumour progression or therapy is based on near infrared fluorescent carboxylated cyanine dyes with strong necrosis avidity [319]. By using non-invasive MSOT imaging in a mouse model, these dyes have been shown to accumulate in the deoxy-haemoglobin-rich tumour core (Fig. 20d). *Ex vivo* validation further confirmed the presence of tissue necrosis inside the tumours.

4.8 Cellular and sub-cellular function

Optical microscopy has become the workhorse of modern biological discovery. Despite its central role in nearly all biological and biochemical investigations, microscopic techniques have several significant drawbacks such as the need for labeling or the presence of unspecific endogenous autofluorescence. The fundamentally different intrinsic contrast explored in optoacoustic microscopy may thus turn advantageous for label-free observations. The high speed and subcellular resolution attained with state-of-the-art optoacoustic microscopy are thus poised to deliver new imaging capacities and biological insights at the cellular and sub-cellular levels.

Since optoacoustics is a truly spectroscopic imaging method, observations can be made by relying on numerous proteins and their subsidiary amino acids that absorb light at known wavelengths. For instance, DNA, cytochromes and mitochondria are known to have different

absorption spectra in the 250 to 420 nm wavelength range. Optoacoustic microscopy studies of unstained fibroblasts were performed where the cytoplasm could be readily identified from the nucleus [320] (Fig. 21a).

Recent studies demonstrated 3D renderings of single blood cells from purely endogenous contrast [51] (Fig. 21b). The only comparable method with equivalent 3D imaging capacity at this level is atomic force microscopy, which is however much slower and requires arduous sample and instrument preparation. In yet another study based on a two-photon absorption mechanism *in vivo* label-free optoacoustic microscopy was used to observe non-fluorescent melanin distribution within mouse skin with high frame rates and sub-femtoliter 3D resolution [37] (Fig. 21c).

Finally, super resolution methods have undoubtedly been the largest contributor to the recent progress in light microscopy, and have also been broadly adopted in optoacoustic microscopy. Whilst fluorescence-based super resolution requires the use of stochastically emitting fluorescent proteins or high powered laser illumination for stimulation depletion (increased phototoxicity), optoacoustic microscopy can take advantage of endogenous contrast to produce comparable results. A third-order label-free optoacoustic nanoscopy technique was shown capable of visualizing mitochondria in fibroblasts down to a lateral resolution of 88.0 +/− 12.5 nm [32] (Fig. 21d).

4.9 Developmental biology

Multiscale imaging is essential in developmental biology to understand the coordination of the multiple growth and development mechanisms at the molecular, cellular, organ and whole-organism levels. Developmental biology and experimental genetics often rely on insects or vertebrate models such as Drosophila melanogaster or zebrafish due to their low breeding complexity, well documented genetics and good representation of several common human diseases. Zebrafish embryos have been imaged with OR-PAM [25]. A hybrid focus optoacoustic microscope operating both in the ballistic and diffuse regime of light was used for volumetric tracking of migratory melanophores in zebrafish at different developmental stages [321] (Fig. 22a). Three-dimensional visualization of melanophores is challenging using optical microscopy due to the lack of fluorescence contrast, yet mechanisms of specification and regeneration of melanophores are important for the understanding of melanomas and other related human disorders. Tomographic optoacoustic imaging has also been used for studying embryo development in mouse models [322] (Fig. 22b). Here the strong blood contrast has enabled accurate characterization of the cardiovascular system development and malformations in the heart.

Although several organisms can be efficiently visualized by optical microscopy due to their transparency at the larval and embryonic developmental stages, light scattering considerably increases as the organism grows and expands, making those organisms inaccessible by optical microscopy at the juvenile or adult stages. In response, hybrid optoacoustic and optical imaging methods were developed in order to expand the time window of developmental observations [323]. Examples of the recently showcased combinations include optoacoustic and confocal microscopy [25] as well as optoacoustic tomography and selective plane illumination microscopy [324].

4.10 Longitudinal dynamics and disease progression

Disease progression can be monitored with endogenous or exogenous optoacoustic contrast. Genetically encoded optoacoustic contrast mechanisms can help to visualize otherwise invisible non-vascularized tissues. For example, the tyrosinase-based genetic reporter system was used to obtain 3D optoacoustic images of xenografts in mice at 10 mm depths [241] (Fig. 23a). For this, melanin-producing cells were inoculated in a mouse, and optoacoustic imaging was capable of following the angiogenesis and tumour expansion over several weeks in high detail. In another study, neovascularization of a developing implanted tumour could be visualized with high resolution and over time using OR-PAM [325]. Here repeated imaging of the same skin area without motion artefacts was achieved by using a surgically implanted skin clamp. Major features of tumour angiogenesis, like the change of vascular tortuosity, dilation of vessel diameters and increase of blood supply could clearly be analysed.

Optoacoustics is also particularly suited for monitoring the evolution of skin cancers. In particular, melanoma is the deadliest type of skin cancer, known for the early occurrence of sentinel lymph node (SLN) metastases. The chief motivation is the current lack of diagnostic means to detect metastases in transit from the primary tumour site to the SLNs. Micrometastases in the identified SLN were detected and tracked in an *in vivo* mouse model using handheld 5D optoacoustic tomography [91] (Fig. 23b), which was shown to be superior to PET, especially in detecting in-transit metastases. MSOT also helped in the differential diagnosis of melanoma lymph node metastases versus other lymphadenopathies.

Apart from cancer, other diseases can potentially be longitudinally monitored with optoacoustics. For example, diabetes, chronic renal failure, cardiovascular disease and neurological disorders are all associated with the accumulation of advanced glycation end-products (AGEs). AGEs are predictors of disease-associated with long-term complications, thus their early non-invasive detection is of paramount importance. Spectral optoacoustic measurements of AGE in a porcine skin model demonstrated promising prospects for the detection and quantification of AGE accumulation [327]. Optoacoustic monitoring of stroke progression in the whole brain of living mice in a model of middle cerebral artery occlusion (MCAO) was also suggested [299]. Hypoxia resulting from post-stroke ischemia could be identified *in vivo* with MSOT by assessing asymmetric dynamics of deoxygenated haemoglobin in the brain. The area surrounding the stroke was further identified non-invasively as hemodynamically-compromised. OR-PAM was further used for imaging amyloid plaques in an Alzheimer's transgenic mouse model [326] (Fig. 23c). Amyloid-beta plaques inside the brain are hallmarks of Alzheimer's disease that seem to play a major role in its development. While this application needed invasive imaging via a cranial window and a plaque-specific dye staining, plaques could readily be visualized in the presence of highly absorbing brain vasculature.

4.11 Clinical translation

The great potential of optoacoustic imaging showcased in preclinical research has encouraged the translation of this technology into the clinics with multiple applications envisioned, from intraoperative diagnostics to ophthalmology, dermatology and endoscopic

imaging. One of the key advantages of optoacoustic imaging is its intrinsic potential to deliver complete volumetric tomographic datasets from the imaged object with a single interrogating laser pulse, a possibility that does not exist in other clinical imaging modalities. This capacity also comes with important clinical advantages, such as the ability to dynamically visualize the bio-distribution of contrast agents in 3D and reduce out-of-plane and motion artefacts, thus facilitating clinical observations.

Dedicated handheld optoacoustic probes have recently been introduced for high performance imaging of human subjects. Those come with real-time tomographic imaging capacities in 2D [93, 97] and 3D [329] as well as integrated pulse-echo ultrasonography capabilities [103,330]. One promising application is the assessment of the metastatic status of sentinel lymph nodes in human melanoma. In the first-in-human study, cross-sectional and volumetric MSOT were used to image SLNs *ex vivo* and *in vivo* in patients with melanoma [106]. In comparison with the conventional protocols for analysis of excised SLNs, it was possible to significantly improve the tumour metastasis detection rate from 214 melanoma patients using MSOT. When combining non-invasive MSOT imaging with subcutaneous injection of the ICG contrast agent, visualization of the SLNs *in vivo* in 20 patients was further performed with up to 5-cm effective imaging depth (Fig. 24a). MSOT identified cancer-free SLNs *in vivo* and *ex vivo* without a single false negative (189 total lymph nodes), with 100% sensitivity and 48 to 62% specificity. The handheld optoacoustic imaging technology was also used in a feasibility study assessing peripheral blood supply and vascular disease in human feet. Such diagnosis is important in the context of peripheral arterial diseases, diabetic foot, and (autoimmune) vasculitis [331]. In this study, optoacoustic imaging has been shown to be superior to conventional imaging methods (e.g. duplex ultrasonography) in terms of resolution (capillaries as small as 100 μm in diameter were resolved) and its intrinsic spectroscopic capacity to differentiate between arteries and veins. Also, due to its imaging speed, optoacoustic imaging allowed to identify pulsation in arteries.

One potential valuable application of optoacoustics is the diagnosis of breast lesions. It is a favoured application due to the generally low light attenuation in the breast as compared with other tissues [128], which allows penetrating the entire human breast [74]. Indeed, breast cancer diagnosis was aimed with the very first implementations of optoacoustic tomography scanners [332, 333], which was recently followed by several designs optimized for deeper imaging and better detection sensitivity [334]. Several clinical breast imaging studies are ongoing and the method has shown potential for non-invasive detection of malignant lesions. In a clinical study on infiltrating ductal carcinoma, distinct optoacoustic patterns could be classified as mass-like, non-mass like and ring-shaped [328] (Fig. 24b). Ultimately, the comparison of these image features with those from contrast enhanced MRI and with vascular stained histopathology has led to the attribution of optoacoustic signal intensities to the presence of vascularity. However, optoacoustic patterns of malignancy still need to be compared in larger patient cohorts before definite optoacoustic image descriptors can be developed as diagnostic criteria.

Optoacoustic imaging is inherently limited by the effective depth of light penetration into living tissues, hindering whole-body human imaging. Instead, embodiments similar to

endoscopic or intravascular ultrasound are being developed [335]. Spectroscopic intravascular photoacoustic imaging has shown promise to detect and distinguish lipids in atherosclerotic human plaques *ex vivo* [336]. Initial feasibility of *in vivo* intravascular photoacoustic imaging using an integrated ultrasound and photoacoustic imaging catheter was also demonstrated in a rabbit model [337]. In addition, many types of cancers in e.g. lungs, colon, pancreas or prostate are located inside (or in close proximity to) the respiratory system or gastrointestinal tract, where endoscopic procedures are applicable. This has prompted the development of the simultaneous multi-spectral optoacoustic and ultrasonic dual-mode endoscopy, which has shown its ability to image the trachea and the oesophagus of a living rabbit, thus also illustrating its potential clinical application [338].

In the field of dermatology, new non-invasive skin imaging tools are essential to aid real-time diagnosis of skin tumours, chronic inflammation, alopecia, scarring, burns etc, thus minimizing the need for invasive skin biopsy. Optoacoustics offers the unique capacity for high resolution 3D optical mapping of tissue by further delivering highly specific optical contrast from a depth of several millimetres to centimetres in living tissues. A recent study performed on human volunteers, has shown capacity for non-invasive structural and functional analysis of intact hair follicles and pilosebaceous units by volumetric handheld MSOT [339]. On-the-fly assessment of key morphometric parameters of follicles and lipid content as well as functional oxygenation parameters of the associated capillary bed was demonstrated with high spatial resolution below 70μm.

One major limitation for clinical translation remains the lack of clinically-approved probes for contrast-enhanced optoacoustic imaging. ICG has been approved for human use since the 1960s. However, there are currently no other approved compounds that absorb light in the near infrared, which is essential for deep tissue imaging with optoacoustics. In addition, though regulatory-approved preclinical devices have already reached the market, medical device permissions in Europe, United States and other parts of the world are still pending. Once approved, multicenter trials in a number of key clinical applications will facilitate the transition of optoacoustics from a highly potent research platform to an accepted clinical imaging modality.

5 Summary and outlook

The physical effect underlying optoacoustic signal generation, the so-called *photophonic phenomenon*, was discovered in 1880 [340], but only at the turn of 21st century has optoacoustic technology reached the level of maturity that allows it to become a well-accepted biomedical imaging modality. Indeed, it has taken the development of suitable laser sources, sensitive and broadband ultrasound detection technology, as well as fast data acquisition and processing capacities in order to realize efficient and practical imaging devices [341]. The rich endogenous optoacoustic contrast of biological tissues enables non-invasive readings of key functional parameters, such as hemodynamic changes, haemoglobin concentration, oxygen saturation or metabolic rates. Intrinsic sensitivity to other chromophores, such as melanin and lipids, endows optoacoustics with label-free specificity to early markers of cancer or atherosclerosis. Much like other optical imaging modalities, optoacoustics is safe for both small animals and clinical use as it utilizes non-ionizing

radiation at the visible and NIR wavelengths. Technical progress in this area is mainly driven by a large array of unmet biological and medical needs that can be addressed by the unique contrast mechanisms and imaging performance available with optoacoustic methods. Pre-clinical applications have rapidly developed and both experimental and commercial imaging scanners can already be found in many laboratories around the globe. These systems are being used in studies spanning the entire palette of modern biology including cancer, cardiovascular diseases, neuroimaging, ophthalmology, immunology, diabetes and obesity, cell trafficking, and a multitude of other biological functions. The multi-disciplinary nature of optoacoustics is also evinced by the growing contribution from chemistry and nanotechnology, where innovations have taken place in areas of dedicated biomarker design, from nanoparticles and organic dyes, to targeted agents and genetically encoded markers [12].

Dynamic imaging at a high frame rate is of particular importance in neuroscience. The breakthrough multiscale imaging capabilities of optoacoustics can be better appreciated when comparing its dynamic imaging performance with other neuroimaging modalities (Fig. 25). Optical microscopy can provide diffraction-limited or even sub-diffraction spatial resolution on a sub-micron scale [5]. However, the imaging rate rendered with state-of-the-art volumetric microscopy methods is in the 1 mm^3/s range [342–344]. Moreover, photon scattering remains the fundamental physical limitation for those methods, thus the imaged volume cannot be extended beyond several 100s of microns in the depth direction, further impeding acquisition of dynamic information from large tissue volumes. Deep tissue optical imaging can be alternatively done by means of diffuse optical tomography techniques, which however suffer from severely impaired spatial resolution that degrades to about 5–10 mm at centimetre-scale depths [347], [348], depending on the type of imaged tissue. On the opposite edge of the performance scale are functional magnetic resonance imaging (fMRI) [345], [346] or functional ultrasound (fUS) [349]. These non-optical imaging methods are excellent in visualizing large tissue volumes, including the entire human brain. Yet the contrast is mainly representative of tissue morphology, its mechanical properties or hemodynamics. Despite significant efforts in the past decade, synthesis of targeted contrast agents remains difficult for those modalities, severely limiting their applicability in molecular or functional imaging studies. In addition, the relatively low temporal resolution in 3D together with susceptibility to motion artifacts often requires the use of gating approaches in other applications involving fast organ motion, such as cardiac imaging. Even the most advanced pulsed echo and Doppler US methods are prone to artefacts related to rapid motion, e.g. murine heart beat at a rate of 400–600 beats per minute, and fast dynamic imaging performance is still limited in these cases to cross-sectional (2D) scans.

Conventionally, a multi-modality approach has been employed to acquire information at multiple scales by e.g. combining optical microscopy with whole-body tomographic imaging modalities. However, the fundamentally different contrast mechanisms, sensitivity, and other metrics associated with different modalities often hamper efficient combination of the information obtained at several spatial or temporal scales [350]. Optoacoustic imaging is unique in its ability to bridge the gap between the microscopic and macroscopic realms with the same type of contrast, from microscopic observations at the single capillary and cell level to whole body imaging of small animals and deep tissue imaging of humans. By

adjusting the parameters of optical illumination and/or ultrasonic detection, the spatial resolution and imaging depths can be flexibly adapted to the particular application. As a rule of thumb, depth-to-resolution ratio of approximately 200 can be achieved for *in vivo* applications [13]. Imaging of dynamic biological events is continuously applicable all the way from video-rate volumetric acquisitions to longitudinal studies of disease progression and treatment monitoring lasting for days or weeks [73]. As anticipated, the temporal resolution generally scales inversely with the effective field of view (Fig. 25). Generally, the optimum trade-off between spatial resolution, temporal resolution and field of view depends on the particular application considered and the optoacoustic imaging system must be designed accordingly in terms of its different technical parameters – pulse repetition rate of the excitation laser, size of the illumination spot, number and bandwidth of the ultrasound detectors, signal range and sampling parameters of the digital acquisition system.

The way ahead is fascinating. Given the current progress in nanoparticle research and the versatility of optoacoustic contrast mechanisms, it is anticipated that future developments in light absorbing agents would bring the dynamic contrast enhancement approaches to a new level of performance. Novel smart agents that selectively change their optoacoustic contrast with environmental changes or theranostic agents releasing drugs at specific targets may all lead to paradigm shifts in biomedical research. Ideally, agents need to be optimized for more efficient optoacoustic signal generation, both in terms of the overall generated signal strength and spectral response. In this regard, development of novel dyes and genetic labels with preferential absorption in the far-red or NIR ranges for deep tissue optoacoustic imaging represents a highly promising research direction. To this end, the majority of new optoacoustic contrast agents have only been tested at a proof-of-principle level or early stages of exploration, thus further validations for biocompatibility, toxicity and targeting efficiency are necessary to establish *in vivo* applicability. In particular, biocompatibility issues may limit applicability if the maximum allowable administered dose is insufficient for generating a distinctive signal. Other circulatory and physiological barriers exist for large-sized agents with sizes of hundreds of nanometers [12]. Given the relatively early stage of most optoacoustic contrast agent developments, reproducibility of the results can be greatly facilitated if the developed agents are efficiently disseminated among the research laboratories, assisted with standardized methods of chemical synthesis that reduce the production costs.

From the technical point of view, much like other imaging modalities, optoacoustics comes with its own set of limitations that call for development of advanced solutions. Naturally, imaging depth is restricted due to light attenuation in optically opaque tissues, which also affects the minimal detectable concentrations of intrinsic tissue chromophores and extrinsically-administered contrast agents. Some of it can be compensated by increasing the deposited laser energy. However, for *in vivo* applications, especially those involving human subjects, illumination on the skin surface is limited by the laser exposure safety standards [21]. As a result, the effective imaging depth is usually restricted to regions where the light fluence is sufficiently high to generate detectable pressure variations, typically up to a few centimeters in most soft tissues. Imaging in deeper areas can be alternatively done using intravascular or endoscopic approaches. To this end, *in vivo* sensitivities in the sub-micromolar (for organic dyes and proteins) and picomolar (for solid nanoparticles) ranges

were reported [351]. In reality, sensitivity limits are not only affected by molecular weight of the probe employed but also by multiple additional factors, such as the total volume, the spectrum and absorption coefficient of the imaged chromophore, the noise equivalent pressure (NEP) of the detectors as well as the level and spectral dependence of background tissue absorption.

The highly heterogeneous nature of biological tissues may further lead to the appearance of significant image artifacts and compromise imaging performance and quantification. Related problems are acoustic mismatches between different soft tissues [352], [353] as well as additional effects related to the presence of strongly reflecting and scattering tissues [354], such as bones and lungs. In multispectral imaging applications, one further faces the challenge of the so-called ‘spectral coloring’. Due to the non-local and non-linear dependence of the light fluence distribution on the optical properties of the object [355], spectra of various tissue chromophores and agents, extracted by means of optoacoustics, might be corrupted [113]. For improving quantitative determination of chromophore concentrations, the light distribution in tissue needs to be accurately accounted for [356]. All those represent challenging problems in optoacoustic imaging and tomography and therefore very active research areas.

Quantitative rendering of chromophore concentration is perhaps among the most important yet challenging tasks of optoacoustic methods. Haemoglobin in its oxygenated and deoxygenated form is the most dominant intrinsic absorber in mammalian tissues in both the visible and most of the NIR range of the optical spectrum. On the one hand, this allows for the label-free quantitative determination of hemodynamics and blood oxygenation, which are related to a variety of physiological parameters. However, when imaging other chromophores or extrinsically-administered contrast agents, the strong blood background may hamper quantified extraction of biomarker concentrations. This prompts the development of new approaches for efficient separation/unmixing of the haemoglobin-related optoacoustic signals in the spectral, temporal or spatial domains.

Acknowledgments

Financial support is acknowledged from the European Research Council Grants *ERC-2010-StG-260991* and *ERC-2015-CoG-682379* (D.R), National Institute of Health grant *R21-EY026382-01* (D.R. and S.S), Human Frontier Science Program (HFSP) Grant RGY0070/2016 (D.R), German research Foundation Grant RA1848/5-1 (D.R.), German-Israeli Foundation (GIF) for Scientific Research and Development Grant *1142-46.10/2011* (D.R. and S.S.).

References

1. Weissleder R, Nahrendorf M. Advancing biomedical imaging. Proceedings of the National Academy of Sciences of the United States of America. 2015; 112:14424–14428. [PubMed: 26598657]
2. Osmanski BF, Pezet S, Ricobaraza A, Lenkei Z, Tanter M. Functional ultrasound imaging of intrinsic connectivity in the living rat brain with high spatiotemporal resolution. Nat Commun. 2014; 5
3. Giepmans BNG, Adams SR, Ellisman MH, Tsien RY. Review - The fluorescent toolbox for assessing protein location and function. Science. 2006; 312:217–224. [PubMed: 16614209]
4. Chudakov DM, Matz MV, Lukyanov S, Lukyanov KA. Fluorescent Proteins and Their Applications in Imaging Living Cells and Tissues. Physiol Rev. 2010; 90:1103–1163. [PubMed: 20664080]

5. Ntziachristos V. Going deeper than microscopy: the optical imaging frontier in biology. Nature methods. 2010; 7:603–614. [PubMed: 20676081]
6. Ale A, Ermolayev V, Herzog E, Cohrs C, de Angelis MH, Ntziachristos V. FMT-XCT: in vivo animal studies with hybrid fluorescence molecular tomography-X-ray computed tomography. Nature methods. 2012; 9:615-+. [PubMed: 22561987]
7. Hilderbrand SA, Weissleder R. Near-infrared fluorescence: application to in vivo molecular imaging. Curr Opin Chem Biol. 2010; 14:71–79. [PubMed: 19879798]
8. Shcherbakova DM, Verkhusha VV. Near-infrared fluorescent proteins for multicolor in vivo imaging. Nature methods. 2013; 10:751-+. [PubMed: 23770755]
9. Guo ZQ, Park S, Yoon J, Shin I. Recent progress in the development of near-infrared fluorescent probes for bioimaging applications. Chem Soc Rev. 2014; 43:16–29. [PubMed: 24052190]
10. Wang LV, Yao J. A practical guide to photoacoustic tomography in the life sciences. Nature methods. 2016; 13:627–638. [PubMed: 27467726]
11. Dean-Ben XL, Razansky D. Adding fifth dimension to optoacoustic imaging: volumetric time-resolved spectrally enriched tomography. Light-Sci Appl. 2014; 3
12. Weber J, Beard PC, Bohndiek SE. Contrast agents for molecular photoacoustic imaging. Nature methods. 2016; 13:639–650. [PubMed: 27467727]
13. Wang LHV, Hu S. Photoacoustic Tomography: In Vivo Imaging from Organelles to Organs. Science. 2012; 335:1458–1462. [PubMed: 22442475]
14. James ML, Gambhir SS. A Molecular Imaging Primer: Modalities, Imaging Agents, and Applications. Physiol Rev. 2012; 92:897–965. [PubMed: 22535898]
15. Taruttis A, Ntziachristos V. Advances in real-time multispectral optoacoustic imaging and its applications. Nat Photonics. 2015; 9:219–227.
16. Wang LV. Tutorial on photoacoustic microscopy and computed tomography. Ieee J Sel Top Quant. 2008; 14:171–179.
17. Wang, LV., Wu, H-i. Biomedical optics: principles and imaging. John Wiley & Sons; 2012.
18. Kim C, Favazza C, Wang LHV. In Vivo Photoacoustic Tomography of Chemicals: High-Resolution Functional and Molecular Optical Imaging at New Depths. Chemical reviews. 2010; 110:2756–2782. [PubMed: 20210338]
19. Deliolanis NC, Ale A, Morscher S, Burton NC, Schaefer K, Radrich K, Razansky D, Ntziachristos V. Deep-Tissue Reporter-Gene Imaging with Fluorescence and Optoacoustic Tomography: A Performance Overview. Molecular Imaging and Biology. 2014; 16:652–660. [PubMed: 24609633]
20. Chen YS, Frey W, Kim S, Kruizinga P, Homan K, Emelianov S. Silica-Coated Gold Nanorods as Photoacoustic Signal Nanoamplifiers. Nano Lett. 2011; 11:348–354. [PubMed: 21244082]
21. American National Standards for the Safe Use of Lasers ANSI Z136.1. American Laser Institute; 2000.
22. Yao J, Wang L, Yang J-M, Maslov KI, Wong TT, Li L, Huang C-H, Zou J, Wang LV. High-speed label-free functional photoacoustic microscopy of mouse brain in action. Nature Methods. 2015; 12:407–410. [PubMed: 25822799]
23. Maslov K, Zhang HF, Hu S, Wang LV. Optical-resolution photoacoustic microscopy for in vivo imaging of single capillaries. Opt Lett. 2008; 33:929–931. [PubMed: 18451942]
24. Hu S, Maslov K, Wang LV. Second-generation optical-resolution photoacoustic microscopy with improved sensitivity and speed. Opt Lett. 2011; 36:1134–1136. [PubMed: 21479007]
25. Rao B, Soto F, Kerschensteiner D, Wang LHV. Integrated photoacoustic, confocal, and two-photon microscope. Journal of biomedical optics. 2014; 19
26. Soliman D, Tserevelakis GJ, Omar M, Ntziachristos V. Combining microscopy with mesoscopy using optical and optoacoustic label-free modes. Sci Rep-Uk. 2015; 5
27. Shi W, Hajireza P, Shao P, Forbrich A, Zemp RJ. In vivo near-realtime volumetric optical-resolution photoacoustic microscopy using a high-repetition-rate nanosecond fiber-laser. Optics express. 2011; 19:17143–17150. [PubMed: 21935076]
28. Cao R, Kilroy JP, Ning B, Wang T, Hossack JA, Hu S. Multispectral photoacoustic microscopy based on an optical–acoustic objective. Photoacoustics. 2015; 3:55–59. [PubMed: 26236641]

29. Bai XS, Gong XJ, Hau W, Lin RQ, Zheng JX, Liu CB, Zeng CZ, Zou X, Zheng HR, Song L. Intravascular Optical-Resolution Photoacoustic Tomography with a 1.1 mm Diameter Catheter. PloS one. 2014; 9
30. Hai PF, Yao JJ, Maslov KI, Zhou Y, Wang LHV. Near-infrared optical-resolution photoacoustic microscopy. Opt Lett. 2014; 39:5192–5195. [PubMed: 25166107]
31. Maswadi SM, Ibey BL, Roth CC, Tsyboulski DA, Beier HT, Glickman RD, Oraevsky AA. All-optical optoacoustic microscopy based on probe beam deflection technique. Photoacoustics. 2016
32. Danielli A, Maslov K, Garcia-Uribe A, Winkler AM, Li CY, Wang LD, Chen Y, Dorn GW, Wang LV. Label-free photoacoustic nanoscopy. Journal of biomedical optics. 2014; 19
33. Nedosekin DA, Galanzha EI, Dervishi E, Biris AS, Zharov VP. Super-Resolution Nonlinear Photothermal Microscopy. Small. 2014; 10:135–142. [PubMed: 23864531]
34. Yao JJ, Wang LD, Li CY, Zhang C, Wang LHV. Photoimprint Photoacoustic Microscopy for Three-Dimensional Label-Free Subdiffraction Imaging. Physical review letters. 2014; 112
35. Wang LD, Zhang C, Wang LHV. Grueneisen Relaxation Photoacoustic Microscopy. Physical review letters. 2014; 113
36. Goy AS, Fleischer JW. Resolution enhancement in nonlinear photoacoustic imaging. Appl Phys Lett. 2015; 107
37. Lee SY, Lai YH, Huang KC, Cheng YH, Tseng TF, Sun CK. In vivo sub-femtoliter resolution photoacoustic microscopy with higher frame rates. Sci Rep-Uk. 2015; 5
38. Strohm EM, Berndl ES, Kolios MC. High frequency label-free photoacoustic microscopy of single cells. Photoacoustics. 2013; 1:49–53. [PubMed: 25302149]
39. Dean-Ben XL, Razansky D, Ntziachristos V. The effects of acoustic attenuation in optoacoustic signals. Physics in medicine and biology. 2011; 56:6129–6148. [PubMed: 21873768]
40. Wang LD, Maslov K, Wang LHV. Single-cell label-free photoacoustic flowoxigraphy in vivo. Proceedings of the National Academy of Sciences of the United States of America. 2013; 110:5759–5764. [PubMed: 23536296]
41. Hsu HC, Wang LD, Wang LV. In vivo photoacoustic microscopy of human cuticle microvasculature with single-cell resolution. Journal of biomedical optics. 2016; 21
42. Song LA, Maslov K, Wang LV. Multifocal optical-resolution photoacoustic microscopy in vivo. Opt Lett. 2011; 36:1236–1238. [PubMed: 21479041]
43. Liang JY, Zhou Y, Winkler AW, Wang LD, Maslov KI, Li CY, Wang LHV. Random-access optical-resolution photoacoustic microscopy using a digital micromirror device. Opt Lett. 2013; 38:2683–2686. [PubMed: 23903111]
44. Yeh C, Soetikno B, Hu S, Maslov KI, Wang LHV. Three-dimensional arbitrary trajectory scanning photoacoustic microscopy. Journal of biophotonics. 2015; 8:303–308. [PubMed: 25077689]
45. Park S, Lee C, Kim J, Kim C. Acoustic resolution photoacoustic microscopy. Biomedical Engineering Letters. 2014; 4:213–222.
46. Li M-L, Zhang HF, Maslov K, Stoica G, Wang LV. Improved in vivo photoacoustic microscopy based on a virtual-detector concept. Opt Lett. 2006; 31:474–476. [PubMed: 16496891]
47. Caballero MÁA, Rosenthal A, Gateau J, Razansky D, Ntziachristos V. Model-based optoacoustic imaging using focused detector scanning. Opt Lett. 2012; 37:4080–4082. [PubMed: 23027285]
48. Turner J, Estrada H, Kneipp M, Razansky D. Improved optoacoustic microscopy through three-dimensional spatial impulse response synthetic aperture focusing technique. Opt Lett. 2014; 39:3390–3393. [PubMed: 24978493]
49. Zhang HF, Maslov K, Stoica G, Wang LHV. Functional photoacoustic microscopy for high-resolution and noninvasive in vivo imaging. Nat Biotechnol. 2006; 24:848–851. [PubMed: 16823374]
50. Aguirre J, Schwarz M, Soliman D, Buehler A, Omar M, Ntziachristos V. Broadband mesoscopic optoacoustic tomography reveals skin layers. Opt Lett. 2014; 39:6297–6300. [PubMed: 25361338]
51. Strohm EM, Moore MJ, Kolios MC. Single cell photoacoustic microscopy: a review. IEEE Journal of Selected Topics in Quantum Electronics. 2016; 22:137–151.
52. Estrada H, Turner J, Kneipp M, Razansky D. Real-time optoacoustic brain microscopy with hybrid optical and acoustic resolution. Laser Phys Lett. 2014; 11:045601.

53. Laufer J, Johnson P, Zhang E, Treeby B, Cox B, Pedley B, Beard P. In vivo preclinical photoacoustic imaging of tumor vasculature development and therapy. Journal of biomedical optics. 2012; 17
54. Xu MH, Wang LHV. Universal back-projection algorithm for photoacoustic computed tomography. Phys Rev E. 2005; 71
55. Treeby BE, Cox BT. k-Wave: MATLAB toolbox for the simulation and reconstruction of photoacoustic wave fields. Journal of biomedical optics. 2010; 15
56. Rosenthal A, Razansky D, Ntziachristos V. Fast Semi-Analytical Model-Based Acoustic Inversion for Quantitative Optoacoustic Tomography. IEEE transactions on medical imaging. 2010; 29:1275–1285. [PubMed: 20304725]
57. Caballero MAA, Gateau J, Dean-Ben XL, Ntziachristos V. Model-Based Optoacoustic Image Reconstruction of Large Three-Dimensional Tomographic Datasets Acquired With an Array of Directional Detectors. IEEE transactions on medical imaging. 2014; 33:433–443. [PubMed: 24144658]
58. Wang XD, Pang YJ, Ku G, Xie XY, Stoica G, Wang LHV. Noninvasive laser-induced photoacoustic tomography for structural and functional in vivo imaging of the brain. Nat Biotechnol. 2003; 21:803–806. [PubMed: 12808463]
59. Razansky D, Distel M, Vinegoni C, Ma R, Perrimon N, Koster RW, Ntziachristos V. Multispectral opto-acoustic tomography of deep-seated fluorescent proteins in vivo. Nat Photonics. 2009; 3:412–417.
60. Gratt S, Passler K, Nuster R, Paltauf G. Photoacoustic section imaging with an integrating cylindrical detector. Biomedical optics express. 2011; 2:2973–2981. [PubMed: 22076260]
61. Ma R, Distel M, Dean-Ben XL, Ntziachristos V, Razansky D. Non-invasive whole-body imaging of adult zebrafish with optoacoustic tomography. Physics in medicine and biology. 2012; 57:7227–7237. [PubMed: 23075767]
62. van Es P, Biswas SK, Moens HJB, Steenbergen W, Manohar S. Initial results of finger imaging using photoacoustic computed tomography. Journal of biomedical optics. 2014; 19
63. Xi L, Jiang HB. High resolution three-dimensional photoacoustic imaging of human finger joints in vivo. Appl Phys Lett. 2015; 107
64. Wang XD, Chamberland DL, Carson PL, Fowlkes JB, Bude RO, Jamadar DA, Roessler BJ. Imaging of joints with laser-based photoacoustic tomography: An animal study. Medical physics. 2006; 33:2691–2697. [PubMed: 16964846]
65. Zhang E, Laufer J, Beard P. Backward-mode multiwavelength photoacoustic scanner using a planar Fabry-Perot polymer film ultrasound sensor for high-resolution three-dimensional imaging of biological tissues. Applied optics. 2008; 47:561–577. [PubMed: 18239717]
66. Omar M, Rebling J, Wicker K, Schmitt-Manderbach T, Schwarz M, Gateau J, López-Schier H, Mappes T, Ntziachristos V. Optical imaging of post-embryonic zebrafish using multi orientation raster scan optoacoustic mesoscopy. Light Science & Applications. 2017; 6:e16186.
67. Sandbichler M, Krahmer F, Berer T, Burgholzer P, Haltmeier M. A Novel Compressed Sensing Scheme for Photoacoustic Tomography. Siam J Appl Math. 2015; 75:2475–2494.
68. Arridge S, Beard P, Betcke M, Cox B, Huynh N, Lucka F, Ogunlade O, Zhang E. Accelerated high-resolution photoacoustic tomography via compressed sensing. Phys Med Biol. 2016; 61:8908–8940. [PubMed: 27910824]
69. Meng J, Jiang ZB, Wang LV, Park J, Kim C, Sun MJ, Zhang YK, Song L. High-speed, sparse-sampling three-dimensional photoacoustic computed tomography in vivo based on principal component analysis. Journal of biomedical optics. 2016; 21
70. Nuster R, Slezak P, Paltauf G. High resolution three-dimensional photoacoustic tomography with CCD-camera based ultrasound detection. Biomedical optics express. 2014; 5:2635–2647. [PubMed: 25136491]
71. Brecht HP, Su R, Fronheiser M, Ermilov SA, Conjusteau A, Oraevsky AA. Whole-body three-dimensional optoacoustic tomography system for small animals. Journal of biomedical optics. 2009; 14

72. Gateau J, Caballero MAA, Dima A, Ntziachristos V. Three-dimensional optoacoustic tomography using a conventional ultrasound linear detector array: Whole-body tomographic system for small animals. Medical physics. 2013; 40
73. Dean Ben XL, Fehm TF, Gottschalk S, Ford SJ, Razanksy D. Spiral volumetric optoacoustic tomography visualizes multi-scale dynamics in mice. Light Science & Applications. 2017; 6:e16247.
74. Kruger RA, Lam RB, Reinecke DR, Del Rio SP, Doyle RP. Photoacoustic angiography of the breast. Medical physics. 2010; 37:6096–6100. [PubMed: 21158321]
75. Kolkman RGM, Brands PJ, Steenbergen W, van Leeuwen TG. Real-time in vivo photoacoustic and ultrasound imaging. Journal of biomedical optics. 2008; 13
76. Kim C, Erpelding TN, Jankovic L, Pashley MD, Wang LHV. Deeply penetrating in vivo photoacoustic imaging using a clinical ultrasound array system. Biomedical optics express. 2010; 1:278–284. [PubMed: 21258465]
77. Daoudi K, van den Berg PJ, Rabot O, Kohl A, Tisserand S, Brands P, Steenbergen W. Handheld probe integrating laser diode and ultrasound transducer array for ultrasound/photoacoustic dual modality imaging. Optics express. 2014; 22:26365–26374. [PubMed: 25401669]
78. Sivasubramanian K, Pramanik M. High frame rate photoacoustic imaging at 7000 frames per second using clinical ultrasound system. Biomedical optics express. 2016; 7:312–323. [PubMed: 26977342]
79. Yuan J, Xu G, Yu Y, Zhou Y, Carson PL, Wang XD, Liu XJ. Real-time photoacoustic and ultrasound dual-modality imaging system facilitated with graphics processing unit and code parallel optimization. Journal of biomedical optics. 2013; 18
80. Alqasemi U, Li H, Yuan GQ, Kumavor P, Zanganeh S, Zhu Q. Interlaced photoacoustic and ultrasound imaging system with real-time coregistration for ovarian tissue characterization. Journal of biomedical optics. 2014; 19
81. Wei CW, Nguyen TM, Xia J, Arnal B, Wong EY, Pelivanov IM, O'Donnell M. Real-Time Integrated Photoacoustic and Ultrasound (PAUS) Imaging System to Guide Interventional Procedures: Ex Vivo Study. Ieee T Ultrason Ferr. 2015; 62:319–328.
82. Deán-Ben XL, Razansky D. On the link between the speckle free nature of optoacoustics and visibility of structures in limited-view tomography. Photoacoustics. 2016; 4:133–140. [PubMed: 28066714]
83. Xu Y, Wang LV, Ambartsoumian G, Kuchment P. Reconstructions in limited-view thermoacoustic tomography. Medical physics. 2004; 31:724–733. [PubMed: 15124989]
84. Gamelin J, Maurudis A, Aguirre A, Huang F, Guo PY, Wang LV, Zhu Q. A real-time photoacoustic tomography system for small animals. Optics express. 2009; 17:10489–10498. [PubMed: 19550444]
85. Buehler A, Herzog E, Razansky D, Ntziachristos V. Video rate optoacoustic tomography of mouse kidney perfusion. Opt Lett. 2010; 35:2475–2477. [PubMed: 20634868]
86. Buehler A, Kacprowicz M, Taruttis A, Ntziachristos V. Real-time handheld multispectral optoacoustic imaging. Opt Lett. 2013; 38:1404–1406. [PubMed: 23632499]
87. Tzoumas S, Deliolanis NC, Morscher S, Ntziachristos V. Unmixing Molecular Agents From Absorbing Tissue in Multispectral Optoacoustic Tomography. IEEE transactions on medical imaging. 2014; 33:48–60. [PubMed: 24001986]
88. Razansky D, Buehler A, Ntziachristos V. Volumetric real-time multispectral optoacoustic tomography of biomarkers. Nature protocols. 2011; 6:1121–1129. [PubMed: 21738125]
89. Wang J, Xie YD, Wang LM, Tang JL, Li JY, Kocaefe D, Kocaefe Y, Zhang ZW, Li YP, Chen CY. In vivo pharmacokinetic features and biodistribution of star and rod shaped gold nanoparticles by multispectral optoacoustic tomography. Rsc Adv. 2015; 5:7529–7538.
90. McNally LR, Mezera M, Morgan DE, Frederick PJ, Yang ES, Eltoum I-E, Grizzle WE. Current and Emerging Clinical Applications of Multispectral Optoacoustic Tomography (MSOT) in Oncology. Clin Cancer Res. 2016 clincanres. 0573.2016.
91. Neuschmelting V, Lockau H, Ntziachristos V, Grimm J, Kircher MF. Lymph Node Micrometastases and In-Transit Metastases from Melanoma: In Vivo Detection with Multispectral Optoacoustic Imaging in a Mouse Model. Radiology. 2016; 280:137–150. [PubMed: 27144537]

92. Tomaszewski, MR., Quiros-Gonzalez, I., Joseph, J., Bohndiek, SE. SPIE BiOS. International Society for Optics and Photonics; 2016. Measurement of changes in blood oxygenation using multispectral optoacoustic tomography (MSOT) allows assessment of tumor development; p. 97081F-97081F-97088.

93. Dima A, Ntziachristos V. Non-invasive carotid imaging using optoacoustic tomography. Optics express. 2012; 20:25044–25057. [PubMed: 23187270]

94. Scarfe L, Rak-Raszewska A, Geraci S, Darssan D, Sharkey J, Huang JG, Burton NC, Mason D, Ranjzad P, Kenny S, Gretz N, Levy R, Park BK, Garcia-Finana M, Woolf AS, Murray P, Wilm B. Measures of kidney function by minimally invasive techniques correlate with histological glomerular damage in SCID mice with adriamycin-induced nephropathy. Sci Rep-Uk. 2015; 5

95. Queiros D, Dean-Ben XL, Buehler A, Razansky D, Rosenthal A, Ntziachristos V. Modeling the shape of cylindrically focused transducers in three-dimensional optoacoustic tomography. Journal of biomedical optics. 2013; 18

96. Buehler A, Dean-Ben XL, Razansky D, Ntziachristos V. Volumetric Optoacoustic Imaging With Multi-Bandwidth Deconvolution. IEEE transactions on medical imaging. 2014; 33:814–821. [PubMed: 24058023]

97. Buehler A, Dean-Ben XL, Claussen J, Ntziachristos V, Razansky D. Three-dimensional optoacoustic tomography at video rate. Optics express. 2012; 20:22712–22719. [PubMed: 23037421]

98. Xiang LZ, Wang B, Ji LJ, Jiang HB. 4-D Photoacoustic Tomography. Sci Rep-Uk. 2013; 3

99. Dean-Ben XL, Razansky D. Portable spherical array probe for volumetric real-time optoacoustic imaging at centimeter-scale depths. Optics express. 2013; 21:28062–28071. [PubMed: 24514320]

100. Dean-Ben XL, Ford SJ, Razansky D. High-frame rate four dimensional optoacoustic tomography enables visualization of cardiovascular dynamics and mouse heart perfusion (vol 5, 10133, 2015). Sci Rep-Uk. 2015; 5

101. Gottschalk S, Fehm TF, Deán-Ben XL, Tsytsarev V, Razansky D. Correlation between volumetric oxygenation responses and electrophysiology identifies deep thalamocortical activity during epileptic seizures. Neurophotonics. 2017; 4:011007–011007. [PubMed: 27725948]

102. Dean-Ben XL, Fehm TF, Gostic M, Razansky D. Volumetric hand-held optoacoustic angiography as a tool for real-time screening of dense breast. Journal of biophotonics. 2016; 9:253–259. [PubMed: 25966021]

103. Fehm TF, Dean-Ben XL, Razansky D. Four dimensional hybrid ultrasound and optoacoustic imaging via passive element optical excitation in a hand-held probe. Appl Phys Lett. 2014; 105

104. Fehm TF, Deán-Ben XL, Ford SJ, Razanksy D. In vivo whole-body optoacoustic scanner with real-time volumetric imaging capacity. Optica. 2016; 3:1153–1159.

105. Deán-Ben X, Fehm TF, Razansky D. Universal hand-held three-dimensional optoacoustic imaging probe for deep tissue human angiography and functional preclinical studies in real time. JoVE (Journal of Visualized Experiments). 2014:e51864–e51864. [PubMed: 25408083]

106. Stoffels I, Morscher S, Helfrich I, Hillen U, Lehy J, Burton NC, Sardella TCP, Claussen J, Poeppel TD, Bachmann HS, Roesch A, Griewank K, Schadendorf D, Gunzer M, Klode J. Metastatic status of sentinel lymph nodes in melanoma determined noninvasively with multispectral optoacoustic imaging. Sci Transl Med. 2015; 7

107. Dean-Ben XL, Bay E, Razansky D. Functional optoacoustic imaging of moving objects using microsecond-delay acquisition of multispectral three-dimensional tomographic data. Sci Rep-Uk. 2014; 4

108. Nie LM, Chen XY. Structural and functional photoacoustic molecular tomography aided by emerging contrast agents. Chem Soc Rev. 2014; 43:7132–7170. [PubMed: 24967718]

109. Luke GP, Yeager D, Emelianov SY. Biomedical applications of photoacoustic imaging with exogenous contrast agents. Ann Biomed Eng. 2012; 40:422–437. [PubMed: 22048668]

110. Zackrisson S, van de Ven S, Gambhir S. Light in and sound out: emerging translational strategies for photoacoustic imaging. Cancer Res. 2014; 74:979–1004. [PubMed: 24514041]

111. Ntziachristos V, Razansky D. Molecular Imaging by Means of Multispectral Optoacoustic Tomography (MSOT). Chemical reviews. 2010; 110:2783–2794. [PubMed: 20387910]

112. Wu D, Huang L, Jiang MS, Jiang HB. Contrast Agents for Photoacoustic and Thermoacoustic Imaging: A Review. Int J Mol Sci. 2014; 15:23616–23639. [PubMed: 25530615]
113. Tzoumas S, Nunes A, Olefir I, Stangl S, Symvoulidis P, Glasl S, Bayer C, Multhoff G, Ntziachristos V. Eigenspectra optoacoustic tomography achieves quantitative blood oxygenation imaging deep in tissues. Nat Commun. 2016; 7
114. Omar M, Schwarz M, Soliman D, Symvoulidis P, Ntziachristos V. Pushing the Optical Imaging Limits of Cancer with Multi-Frequency-Band Raster-Scan Optoacoustic Mesoscopy (RSOM). Neoplasia. 2015; 17:208–214. [PubMed: 25748240]
115. Herzog E, Taruttis A, Beziere N, Lutich AA, Razansky D, Ntziachristos V. Optical Imaging of Cancer Heterogeneity with Multispectral Optoacoustic Tomography. Radiology. 2012; 263:461–468. [PubMed: 22517960]
116. Yao JJ, Maslov KI, Wang LHV. In vivo Photoacoustic Tomography of Total Blood Flow and Potential Imaging of Cancer Angiogenesis and Hypermetabolism. Technol Cancer Res T. 2012; 11:301–307.
117. Jansen K, van der Steen AFW, van Beusekom HMM, Oosterhuis JW, van Soest G. Intravascular photoacoustic imaging of human coronary atherosclerosis. Opt Lett. 2011; 36:597–599. [PubMed: 21368919]
118. Wang B, Su JL, Amirian J, Litovsky SH, Smalling R, Emelianov S. Detection of lipid in atherosclerotic vessels using ultrasound-guided spectroscopic intravascular photoacoustic imaging. Optics express. 2010; 18:4889–4897. [PubMed: 20389501]
119. Gottschalk S, Fehm TF, Dean-Ben XL, Razansky D. Noninvasive real-time visualization of multiple cerebral hemodynamic parameters in whole mouse brains using five-dimensional optoacoustic tomography. J Cerebr Blood F Met. 2015; 35:531–535.
120. Hu S. Listening to the Brain With Photoacoustics. Ieee J Sel Top Quant. 2016; 22
121. Nasiriavanaki M, Xia J, Wan HL, Bauer AQ, Culver JP, Wang LV. High-resolution photoacoustic tomography of resting-state functional connectivity in the mouse brain. Proceedings of the National Academy of Sciences of the United States of America. 2014; 111:21–26. [PubMed: 24367107]
122. Jacques, SL., Glickman, RD., Schwartz, JA. Photonics West'96. International Society for Optics and Photonics; 1996. Internal absorption coefficient and threshold for pulsed laser disruption of melanosomes isolated from retinal pigment epithelium; p. 468-477.
123. http://omlc.org/spectra.
124. Hale GM, Querry MR. Optical constants of water in the 200-nm to 200-μm wavelength region. Applied optics. 1973; 12:555–563. [PubMed: 20125343]
125. Van Veen R, Sterenborg HJ, Pifferi A, Torricelli A, Chikoidze E, Cubeddu R. Determination of visible near-IR absorption coefficients of mammalian fat using time-and spatially resolved diffuse reflectance and transmission spectroscopy. Journal of biomedical optics. 2005; 10:054004–054004–054006. [PubMed: 16292964]
126. Tsai C-L, Chen J-C, Wang W-J. Near-infrared absorption property of biological soft tissue constituents. Journal of Medical and Biological Engineering. 2001; 21:7–14.
127. Smith AM, Mancini MC, Nie S. Second window for in vivo imaging. Nature nanotechnology. 2009; 4:710.
128. Jacques SL. Optical properties of biological tissues: a review. Physics in medicine and biology. 2013; 58:R37–R61. [PubMed: 23666068]
129. Krumholz A, Shcherbakova DM, Xia J, Wang LHV, Verkhusha VV. Multicontrast photoacoustic in vivo imaging using near-infrared fluorescent proteins. Sci Rep-Uk. 2014; 4
130. Stiel AC, Dean-Ben XL, Jiang YY, Ntziachristos V, Razansky D, Westmeyer GG. High-contrast imaging of reversibly switchable fluorescent proteins via temporally unmixed multispectral optoacoustic tomography. Opt Lett. 2015; 40:367–370. [PubMed: 25680049]
131. Ku G, Wang LHV. Deeply penetrating photoacoustic tomography in biological tissues enhanced with an optical contrast agent. Opt Lett. 2005; 30:507–509. [PubMed: 15789718]
132. Cox B, Laufer JG, Arridge SR, Beard PC. Quantitative spectroscopic photoacoustic imaging: a review. Journal of biomedical optics. 2012; 17

133. Sun TM, Zhang YS, Pang B, Hyun DC, Yang MX, Xia YN. Engineered Nanoparticles for Drug Delivery in Cancer Therapy. Angew Chem Int Edit. 2014; 53:12320–12364.

134. Lee JH, Park G, Hong GH, Choi J, Choi HS. Design considerations for targeted optical contrast agents. Quantitative imaging in medicine and surgery. 2012; 2:266–273. [PubMed: 23289086]

135. Pardridge WM. The blood-brain barrier: bottleneck in brain drug development. NeuroRx. 2005; 2:3–14. [PubMed: 15717053]

136. Petros RA, DeSimone JM. Strategies in the design of nanoparticles for therapeutic applications. Nat Rev Drug Discov. 2010; 9:615–627. [PubMed: 20616808]

137. Song WT, Tang ZH, Zhang DW, Burton N, Driessen W, Chen XS. Comprehensive studies of pharmacokinetics and biodistribution of indocyanine green and liposomal indocyanine green by multispectral optoacoustic tomography. Rsc Adv. 2015; 5:3807–3813.

138. Longmire M, Choyke PL, Kobayashi H. Clearance properties of nano-sized particles and molecules as imaging agents: considerations and caveats. Nanomedicine-Uk. 2008; 3:703–717.

139. Lankveld DPK, Rayavarapu RG, Krystek P, Oomen AG, Verharen HW, van Leeuwen TG, De Jong WH, Manohar S. Blood clearance and tissue distribution of PEGylated and non-PEGylated gold nanorods after intravenous administration in rats. Nanomedicine-Uk. 2011; 6:339–349.

140. Ruggiero A, Villa CH, Bander E, Rey DA, Bergkvist M, Batt CA, Manova-Todorova K, Deen WM, Scheinberg DA, McDevitt MR. Paradoxical glomerular filtration of carbon nanotubes. Proceedings of the National Academy of Sciences of the United States of America. 2010; 107:12369–12374. [PubMed: 20566862]

141. Luo SL, Zhang EL, Su YP, Cheng TM, Shi CM. A review of NIR dyes in cancer targeting and imaging. Biomaterials. 2011; 32:7127–7138. [PubMed: 21724249]

142. Shao Q, Ashkenazi S. Photoacoustic lifetime imaging for direct in vivo tissue oxygen monitoring. Journal of biomedical optics. 2015; 20

143. Yao JJ, Maslov K, Hu S, Wang LHV. Evans blue dye-enhanced capillary-resolution photoacoustic microscopy in vivo. Journal of biomedical optics. 2009; 14

144. Resch-Genger U, Grabolle M, Cavaliere-Jaricot S, Nitschke R, Nann T. Quantum dots versus organic dyes as fluorescent labels. Nature methods. 2008; 5:763–775. [PubMed: 18756197]

145. Pu K, Shuhendler AJ, Jokerst JV, Mei J, Gambhir SS, Bao Z, Rao J. Semiconducting polymer nanoparticles as photoacoustic molecular imaging probes in living mice. Nature nanotechnology. 2014; 9:233–239.

146. Pan D, Kim B, Wang LV, Lanza GM. A brief account of nanoparticle contrast agents for photoacoustic imaging. Wiley Interdisciplinary Reviews: Nanomedicine and Nanobiotechnology. 2013; 5:517–543. [PubMed: 23983210]

147. Li K, Liu B. Polymer-encapsulated organic nanoparticles for fluorescence and photoacoustic imaging. Chem Soc Rev. 2014; 43:6570–6597. [PubMed: 24792930]

148. Zhang JC, Qiao ZY, Yang PP, Pan J, Wang L, Wang H. Recent Advances in Near-Infrared Absorption Nanomaterials as Photoacoustic Contrast Agents for Biomedical Imaging. Chinese J Chem. 2015; 33:35–52.

149. Chen H, Yuan Z, Wu C. Nanoparticle probes for structural and functional photoacoustic molecular tomography. BioMed research international. 2015; 2015

150. Wang D, Wu Y, Xia J. Review on photoacoustic imaging of the brain using nanoprobes. Neurophotonics. 2016; 3:010901–010901. [PubMed: 26740961]

151. Wang L, Yang PP, Zhao XX, Wang H. Self-assembled nanomaterials for photoacoustic imaging. Nanoscale. 2016; 8:2488–2509. [PubMed: 26757620]

152. Bertrand N, Wu J, Xu XY, Kamaly N, Farokhzad OC. Cancer nanotechnology: The impact of passive and active targeting in the era of modern cancer biology. Adv Drug Deliver Rev. 2014; 66:2–25.

153. Jokerst JV, Gambhir SS. Molecular Imaging with Theranostic Nanoparticles. Accounts Chem Res. 2011; 44:1050–1060.

154. Hannah A, Luke G, Wilson K, Homan K, Emelianov S. Indocyanine Green-Loaded Photoacoustic Nanodroplets: Dual Contrast Nanoconstructs for Enhanced Photoacoustic and Ultrasound Imaging. Acs Nano. 2014; 8:250–259. [PubMed: 24303934]

155. Beziere N, Lozano N, Nunes A, Salichs J, Queiros D, Kostarelos K, Ntziachristos V. Dynamic imaging of PEGylated indocyanine green (ICG) liposomes within the tumor microenvironment using multi-spectral optoacoustic tomography (MSOT). Biomaterials. 2015; 37:415–424. [PubMed: 25453969]

156. Gupta S, Chatni MR, Rao ALN, Vullev VI, Wang LHV, Anvari B. Virus-mimicking nano-constructs as a contrast agent for near infrared photoacoustic imaging. Nanoscale. 2013; 5:1772–1776. [PubMed: 23334567]

157. Lovell JF, Jin CS, Huynh E, Jin HL, Kim C, Rubinstein JL, Chan WCW, Cao WG, Wang LV, Zheng G. Porphysome nanovesicles generated by porphyrin bilayers for use as multimodal biophotonic contrast agents. Nat Mater. 2011; 10:324–332. [PubMed: 21423187]

158. An FF, Deng ZJ, Ye J, Zhang JF, Yang YL, Li CH, Zheng CJ, Zhang XH. Aggregation-Induced Near-Infrared Absorption of Squaraine Dye in an Albumin Nanocomplex for Photoacoustic Tomography in Vivo. Acs Appl Mater Inter. 2014; 6:17985–17992.

159. Wu C, Chiu DT. Highly fluorescent semiconducting polymer dots for biology and medicine. Angewandte Chemie International Edition. 2013; 52:3086–3109. [PubMed: 23307291]

160. Huynh E, Zheng G. Porphysome nanotechnology: A paradigm shift in lipid-based supramolecular structures. Nano Today. 2014; 9:212–222.

161. Jokerst JV, Van de Sompel D, Bohndiek SE, Gambhir SS. Cellulose nanoparticles are a biodegradable photoacoustic contrast agent for use in living mice. Photoacoustics. 2014; 2:119–127. [PubMed: 25225633]

162. Fan QL, Cheng K, Hu X, Ma XW, Zhang RP, Yang M, Lu XM, Xing L, Huang W, Gambhir SS, Cheng Z. Transferring Biomarker into Molecular Probe: Melanin Nanoparticle as a Naturally Active Platform for Multimodality Imaging. Journal of the American Chemical Society. 2014; 136:15185–15194. [PubMed: 25292385]

163. Liopo A, Su R, Oraevsky AA. Melanin nanoparticles as a novel contrast agent for optoacoustic tomography. Photoacoustics. 2015; 3:35–43. [PubMed: 25893172]

164. Jain PK, Lee KS, El-Sayed IH, El-Sayed MA. Calculated absorption and scattering properties of gold nanoparticles of different size, shape, and composition: Applications in biological imaging and biomedicine. J Phys Chem B. 2006; 110:7238–7248. [PubMed: 16599493]

165. Homan K, Shah J, Gomez S, Gensler H, Karpiouk A, Brannon-Peppas L, Emelianov S. Silver nanosystems for photoacoustic imaging and image-guided therapy. Journal of biomedical optics. 2010; 15

166. Homan KA, Souza M, Truby R, Luke GP, Green C, Vreeland E, Emelianov S. Silver Nanoplate Contrast Agents for in Vivo Molecular Photoacoustic Imaging. Acs Nano. 2012; 6:641–650. [PubMed: 22188516]

167. Li WW, Chen XY. Gold nanoparticles for photoacoustic imaging. Nanomedicine-Uk. 2015; 10:299–320.

168. Asharani PV, Yi LW, Gong ZY, Valiyaveettil S. Comparison of the toxicity of silver, gold and platinum nanoparticles in developing zebrafish embryos. Nanotoxicology. 2011; 5:43–54. [PubMed: 21417687]

169. Grzelczak M, Perez-Juste J, Mulvaney P, Liz-Marzan LM. Shape control in gold nanoparticle synthesis. Chem Soc Rev. 2008; 37:1783–1791. [PubMed: 18762828]

170. Liz-Marzan LM. Nanometals formation and color. Mater Today. 2004; 7:26–31.

171. Lu W, Huang Q, Geng KB, Wen XX, Zhou M, Guzatov D, Brecht P, Su R, Oraevsky A, Wang LV, Li C. Photoacoustic imaging of living mouse brain vasculature using hollow gold nanospheres. Biomaterials. 2010; 31:2617–2626. [PubMed: 20036000]

172. Eghtedari M, Oraevsky A, Copland JA, Kotov NA, Conjusteau A, Motamedi M. High sensitivity of in vivo detection of gold nanorods using a laser optoacoustic imaging system. Nano Lett. 2007; 7:1914–1918. [PubMed: 17570730]

173. Kim C, Cho EC, Chen JY, Song KH, Au L, Favazza C, Zhang QA, Cobley CM, Gao F, Xia YN, Wang LHV. In Vivo Molecular Photoacoustic Tomography of Melanomas Targeted by Bioconjugated Gold Nanocages. Acs Nano. 2010; 4:4559–4564. [PubMed: 20731439]

174. Li WY, Brown PK, Wang LHV, Xia YN. Gold nanocages as contrast agents for photoacoustic imaging. Contrast Media Mol I. 2011; 6:370–377.

175. Rouleau L, Berti R, Ng VWK, Matteau-Pelletier C, Lam T, Saboural P, Kakkar AK, Lesage F, Rheaume E, Tardif JC. VCAM-1-targeting gold nanoshell probe for photoacoustic imaging of atherosclerotic plaque in mice. Contrast Media Mol I. 2013; 8:27–39.

176. Lee HJ, Liu Y, Zhao J, Zhou M, Bouchard RR, Mitcham T, Wallace M, Stafford RJ, Li C, Gupta S, Melancon MP. In vitro and in vivo mapping of drug release after laser ablation thermal therapy with doxorubicin-loaded hollow gold nanoshells using fluorescence and photoacoustic imaging. J Control Release. 2013; 172:152–158. [PubMed: 23920038]

177. Kim C, Song HM, Cai X, Yao JJ, Wei A, Wang LHV. In vivo photoacoustic mapping of lymphatic systems with plasmon-resonant nanostars. J Mater Chem. 2011; 21:2841–2844. [PubMed: 21660122]

178. Nie LM, Wang SJ, Wang XY, Rong PF, Bhirde A, Ma Y, Liu G, Huang P, Lu GM, Chen XY. In Vivo Volumetric Photoacoustic Molecular Angiography and Therapeutic Monitoring with Targeted Plasmonic Nanostars. Small. 2014; 10:1585–1593. [PubMed: 24150920]

179. Bao CC, Beziere N, del Pino P, Pelaz B, Estrada G, Tian FR, Ntziachristos V, de la Fuente JM, Cui DX. Gold Nanoprisms as Optoacoustic Signal Nanoamplifiers for In Vivo Bioimaging of Gastrointestinal Cancers. Small. 2013; 9:68–74. [PubMed: 23001862]

180. Han JS, Zhang JJ, Yang M, Cui DX, de la Fuente JM. Glucose-functionalized Au nanoprisms for optoacoustic imaging and near-infrared photothermal therapy. Nanoscale. 2016; 8:492–499. [PubMed: 26632451]

181. Huang P, Lin J, Li WW, Rong PF, Wang Z, Wang SJ, Wang XP, Sun XL, Aronova M, Niu G, Leapman RD, Nie ZH, Chen XY. Biodegradable Gold Nanovesicles with an Ultrastrong Plasmonic Coupling Effect for Photoacoustic Imaging and Photothermal Therapy. Angew Chem Int Edit. 2013; 52:13958–13964.

182. Dreaden EC, Alkilany AM, Huang XH, Murphy CJ, El-Sayed MA. The golden age: gold nanoparticles for biomedicine. Chem Soc Rev. 2012; 41:2740–2779. [PubMed: 22109657]

183. De La Zerda A, Zavaleta C, Keren S, Vaithilingam S, Bodapati S, Liu Z, Levi J, Smith BR, Ma TJ, Oralkan O, Cheng Z, Chen XY, Dai HJ, Khuri-Yakub BT, Gambhir SS. Carbon nanotubes as photoacoustic molecular imaging agents in living mice. Nature Nanotechnology. 2008; 3:557–562.

184. Liu ZA, Yang K, Lee ST. Single-walled carbon nanotubes in biomedical imaging. J Mater Chem. 2011; 21:586–598.

185. Tsyboulski DA, Liopo AV, Su R, Ermilov SA, Bachilo SM, Weisman RB, Oraevsky AA. Enabling in vivo measurements of nanoparticle concentrations with three-dimensional optoacoustic tomography. Journal of biophotonics. 2014; 7:581–588. [PubMed: 23554158]

186. Bauer DR, Wang X, Vollin J, Xin H, Witte RS. Broadband Spectroscopic Thermoacoustic Characterization of Single-Walled Carbon Nanotubes. J Spectrosc. 2015

187. Kim JW, Galanzha EI, Shashkov EV, Moon HM, Zharov VP. Golden carbon nanotubes as multimodal photoacoustic and photothermal high-contrast molecular agents. Nature Nanotechnology. 2009; 4:688–694.

188. de la Zerda A, Bodapati S, Teed R, May SY, Tabakman SM, Liu Z, Khuri-Yakub BT, Chen XY, Dai HJ, Gambhir SS. Family of Enhanced Photoacoustic Imaging Agents for High-Sensitivity and Multiplexing Studies in Living Mice. Acs Nano. 2012; 6:4694–4701. [PubMed: 22607191]

189. Zanganeh S, Li H, Kumavor PD, Alqasemi U, Aguirre A, Mohammad I, Stanford C, Smith MB, Zhu Q. Photoacoustic imaging enhanced by indocyanine green-conjugated single-wall carbon nanotubes. Journal of biomedical optics. 2013; 18

190. Hong H, Gao T, Cai WB. Molecular imaging with single-walled carbon nanotubes. Nano Today. 2009; 4:252–261. [PubMed: 21754949]

191. Meng LJ, Zhang XK, Lu QH, Fei ZF, Dyson PJ. Single walled carbon nanotubes as drug delivery vehicles: Targeting doxorubicin to tumors. Biomaterials. 2012; 33:1689–1698. [PubMed: 22137127]

192. Wang C, Ma XX, Ye SQ, Cheng L, Yang K, Guo L, Li CH, Li YG, Liu Z. Protamine Functionalized Single-Walled Carbon Nanotubes for Stem Cell Labeling and In Vivo Raman/Magnetic Resonance/Photoacoustic Triple-Modal Imaging. Adv Funct Mater. 2012; 22:2363–2375.

193. Lalwani G, Cai X, Nie L, Wang LV, Sitharaman B. Graphene-based contrast agents for photoacoustic and thermoacoustic tomography. Photoacoustics. 2013; 1:62–67. [PubMed: 24490141]

194. Rong PF, Yang K, Srivastan A, Kiesewetter DO, Yue XY, Wang F, Nie LM, Bhirde A, Wang Z, Liu Z, Niu G, Wang W, Chen XY. Photosensitizer Loaded Nano-Graphene for Multimodality Imaging Guided Tumor Photodynamic Therapy. Theranostics. 2014; 4:229–239. [PubMed: 24505232]

195. Patel MA, Yang H, Chiu PL, Mastrogiovanni DDT, Flach CR, Savaram K, Gomez L, Hemnarine A, Mendelsohn R, Garfunkel E, Jiang HB, He HX. Direct Production of Graphene Nanosheets for Near Infrared Photoacoustic Imaging. Acs Nano. 2013; 7:8147–8157. [PubMed: 24001023]

196. Zhang T, Cui HZ, Fang CY, Su LJ, Ren SQ, Chang HC, Yang XM, Forrest ML. Photoacoustic contrast imaging of biological tissues with nanodiamonds fabricated for high near-infrared absorbance. Journal of biomedical optics. 2013; 18

197. Ku G, Zhou M, Song SL, Huang Q, Hazle J, Li C. Copper Sulfide Nanoparticles As a New Class of Photoacoustic Contrast Agent for Deep Tissue Imaging at 1064 nm. Acs Nano. 2012; 6:7489–7496. [PubMed: 22812694]

198. Yang K, Zhu L, Nie LM, Sun XL, Cheng L, Wu CX, Niu G, Chen XY, Liu Z. Visualization of Protease Activity In Vivo Using an Activatable Photo-Acoustic Imaging Probe Based on CuS Nanoparticles. Theranostics. 2014; 4:134–141. [PubMed: 24465271]

199. Mou J, Li P, Liu CB, Xu HX, Song L, Wang J, Zhang K, Chen Y, Shi JL, Chen HR. Ultrasmall Cu2-xS Nanodots for Highly Efficient Photoacoustic Imaging-Guided Photothermal Therapy. Small. 2015; 11:2275–2283. [PubMed: 25641784]

200. Nie LM, Chen M, Sun XL, Rong PF, Zheng NF, Chen XY. Palladium nanosheets as highly stable and effective contrast agents for in vivo photoacoustic molecular imaging. Nanoscale. 2014; 6:1271–1276. [PubMed: 24317132]

201. Maji SK, Sreejith S, Joseph J, Lin MJ, He TC, Tong Y, Sun HD, Yu SWK, Zhao YL. Upconversion Nanoparticles as a Contrast Agent for Photoacoustic Imaging in Live Mice. Adv Mater. 2014; 26:5633-+. [PubMed: 24913756]

202. He F, Yang GX, Yang PP, Yu YX, Lv RC, Li CX, Dai YL, Gai SL, Lin J. A New Single 808 nm NIR Light-Induced Imaging-Guided Multifunctional Cancer Therapy Platform. Adv Funct Mater. 2015; 25:3966–3976.

203. Du B, Cao XH, Zhao FF, Su XJ, Wang YH, Yan XS, Jia SN, Zhou J, Yao HC. Multimodal imaging-guided, dual-targeted photothermal therapy for cancer. J Mater Chem B. 2016; 4:2038–2050.

204. Shashkov EV, Everts M, Galanzha EI, Zharov VP. Quantum Dots as Multimodal Photoacoustic and Photothermal Contrast Agents. Nano Lett. 2008; 8:3953–3958. [PubMed: 18834183]

205. Hembury M, Chiappini C, Bertazzo S, Kalber TL, Drisko GL, Ogunlade O, Walker-Samuel S, Krishna KS, Jumeaux C, Beard P, Kumar CSSR, Porter AE, Lythgoe MF, Boissiere C, Sanchez C, Stevens MM. Gold-silica quantum rattles for multimodal imaging and therapy. Proceedings of the National Academy of Sciences of the United States of America. 2015; 112:1959–1964. [PubMed: 25653336]

206. Ge JC, Jia QY, Liu WM, Guo L, Liu QY, Lan MH, Zhang HY, Meng XM, Wang PF. Red-emissive carbon dots for fluorescent, photoacoustic, and thermal theranostics in living mice. Adv Mater. 2015; 27:4169–4177. [PubMed: 26045099]

207. Alwi R, Telenkov S, Mandelis A, Leshuk T, Gu F, Oladepo S, Michaelian K. Silica-coated super paramagnetic iron oxide nanoparticles (SPION) as biocompatible contrast agent in biomedical photoacoustics. Biomedical optics express. 2012; 3:2500–2509. [PubMed: 23082291]

208. Grootendorst DJ, Jose J, Fratila RM, Visscher M, Velders AH, Ten Haken B, Van Leeuwen TG, Steenbergen W, Manohar S, Ruers TJM. Evaluation of superparamagnetic iron oxide nanoparticles (Endorem (R)) as a photoacoustic contrast agent for intra-operative nodal staging. Contrast Media Mol I. 2013; 8:83–91.

209. Li JW, Arnal B, Wei CW, Shang J, Nguyen TM, O'Donnell M, Gao XH. Magneto-Optical Nanoparticles for Cyclic Magnetomotive Photoacoustic Imaging. Acs Nano. 2015; 9:1964–1976. [PubMed: 25658655]

210. Liu T, Shi SX, Liang C, Shen SD, Cheng L, Wang C, Song XJ, Goel S, Barnhart TE, Cai WB, Liu Z. Iron Oxide Decorated MoS2 Nanosheets with Double PEGylation for Chelator-Free Radio labeling and Multimodal Imaging Guided Photothermal Therapy. Acs Nano. 2015; 9:950–960. [PubMed: 25562533]
211. Xu RX. Multifunctional microbubbles and nanobubbles for photoacoustic imaging. Contrast Media Mol I. 2011; 6:401–411.
212. Wang YH, Liao AH, Chen JH, Wang CRC, Li PC. Photoacoustic/ultrasound dual-modality contrast agent and its application to thermotherapy. Journal of biomedical optics. 2012; 17
213. Wei CW, Lombardo M, Larson-Smith K, Pelivanov I, Perez C, Xia J, Matula T, Pozzo D, O'Donnell M. Nonlinear contrast enhancement in photoacoustic molecular imaging with gold nanosphere encapsulated nanoemulsions. Appl Phys Lett. 2014; 104
214. Jeon M, Song WT, Huynh E, Kim J, Kim J, Helfield BL, Leung BYC, Goertz DE, Zheng G, Oh J, Lovell JF, Kim C. Methylene blue microbubbles as a model dual-modality contrast agent for ultrasound and activatable photoacoustic imaging. Journal of biomedical optics. 2014; 19
215. Dixon AJ, Hu S, Klibanov AL, Hossack JA. Oscillatory Dynamics and In Vivo Photoacoustic Imaging Performance of Plasmonic Nanoparticle-Coated Microbubbles. Small. 2015; 11:3066–3077. [PubMed: 25703465]
216. Huynh E, Leung BYC, Helfield BL, Shakiba M, Gandier JA, Jin CS, Master ER, Wilson BC, Goertz DE, Zheng G. In situ conversion of porphyrin microbubbles to nanoparticles for multimodality imaging. Nature Nanotechnology. 2015; 10:325–332.
217. Lozano N, Al-Jamal WT, Taruttis A, Beziere N, Burton NC, Van den Bossche J, Mazza M, Herzog E, Ntziachristos V, Kostarelos K. Liposome-Gold Nanorod Hybrids for High-Resolution Visualization Deep in Tissues. Journal of the American Chemical Society. 2012; 134:13256–13258. [PubMed: 22852749]
218. Sim N, Gottschalk S, Pal R, Delbianco M, Degtyaruk O, Razansky D, Westmeyer GG, Ntziachristos V, Parker D, Mishra A. Wavelength-dependent optoacoustic imaging probes for NMDA receptor visualisation. Chem Commun. 2015; 51:15149–15152.
219. Lowery RL, Majewska AK. Intracranial injection of adeno-associated viral vectors. JoVE (Journal of Visualized Experiments). 2010:e2140–e2140.
220. Mamedov I, Canals S, Henig J, Beyerlein M, Murayama Y, Mayer HA, Logothetis NK, Angelovski G. In Vivo Characterization of a Smart MRI Agent That Displays an Inverse Response to Calcium Concentration. Acs Chem Neurosci. 2010; 1:819–828. [PubMed: 22778817]
221. Chu P-C, Liu H-L, Lai H-Y, Lin C-Y, Tsai H-C, Pei Y-C. Neuromodulation accompanying focused ultrasound-induced blood-brain barrier opening. Sci Rep-Uk. 2015; 5
222. Li WW, Rong PF, Yang K, Huang P, Sun K, Chen XY. Semimetal nanomaterials of antimony as highly efficient agent for photoacoustic imaging and photothermal therapy. Biomaterials. 2015; 45:18–26. [PubMed: 25662491]
223. Jin YS, Li YY, Ma XB, Zha ZB, Shi LL, Tian J, Dai ZF. Encapsulating tantalum oxide into polypyrrole nanoparticles for X-ray CT/photoacoustic bimodal imaging-guided photothermal ablation of cancer. Biomaterials. 2014; 35:5795–5804. [PubMed: 24746966]
224. Kim C, Erpelding TN, Maslov K, Jankovic L, Akers WJ, Song LA, Achilefu S, Margenthaler JA, Pashley MD, Wang LHV. Handheld array-based photoacoustic probe for guiding needle biopsy of sentinel lymph nodes. Journal of biomedical optics. 2010; 15
225. Cai XL, Liu XF, Liao LD, Bandla A, Ling JM, Liu YH, Thakor N, Bazan GC, Liu B. Encapsulated Conjugated Oligomer Nanoparticles for Real-Time Photoacoustic Sentinel Lymph Node Imaging and Targeted Photothermal Therapy. Small. 2016; 12:4873–4880. [PubMed: 27439884]
226. Martel C, Yao JJ, Huang CH, Zou J, Randolph GJ, Wang LV. Photoacoustic lymphatic imaging with high spatial-temporal resolution. Journal of biomedical optics. 2014; 19
227. Morozova KS, Piatkevich KD, Gould TJ, Zhang JH, Bewersdorf J, Verkhusha VV. Far-Red Fluorescent Protein Excitable with Red Lasers for Flow Cytometry and Superresolution STED Nanoscopy. Biophys J. 2010; 99:L13–L15. [PubMed: 20643047]

228. Shu XK, Royant A, Lin MZ, Aguilera TA, Lev-Ram V, Steinbach PA, Tsien RY. Mammalian Expression of Infrared Fluorescent Proteins Engineered from a Bacterial Phytochrome. Science. 2009; 324:804–807. [PubMed: 19423828]

229. Shcherbakova DM, Baloban M, Verkhusha VV. Near-infrared fluorescent proteins engineered from bacterial phytochromes. Curr Opin Chem Biol. 2015; 27:52–63. [PubMed: 26115447]

230. Filonov GS, Krumholz A, Xia J, Yao JJ, Wang LHV, Verkhusha VV. Deep-Tissue Photoacoustic Tomography of a Genetically Encoded Near-Infrared Fluorescent Probe. Angew Chem Int Edit. 2012; 51:1448–1451.

231. Li Y, Forbrich A, Wu JH, Shao P, Campbell RE, Zemp R. Engineering Dark Chromoprotein Reporters for Photoacoustic Microscopy and FRET Imaging. Sci Rep-Uk. 2016; 6

232. Ha SH, Carson AR, Kim K. Ferritin as a novel reporter gene for photoacoustic molecular imaging. Cytom Part A. 2012; 81A:910–915.

233. Li L, Zemp RJ, Lungu G, Stoica G, Wang LHV. Photoacoustic imaging of lacZ gene expression in vivo. Journal of biomedical optics. 2007; 12

234. Cai X, Li L, Krumholz A, Guo ZJ, Erpelding TN, Zhang C, Zhang Y, Xi YN, Wang LHV. Multi-Scale Molecular Photoacoustic Tomography of Gene Expression. PloS one. 2012; 7

235. Stritzker J, Kirscher L, Scadeng M, Deliolanis NC, Morscher S, Symvoulidis P, Schaefer K, Zhang Q, Buckel L, Hess M, Donat U, Bradley WG, Ntziachristos V, Szalay AA. Vaccinia virus-mediated melanin production allows MR and optoacoustic deep tissue imaging and laser-induced thermotherapy of cancer. Proceedings of the National Academy of Sciences of the United States of America. 2013; 110:3316–3320. [PubMed: 23401518]

236. Krumholz A, VanVickle-Chavez SJ, Yao JJ, Fleming TP, Gillanders WE, Wang LHV. Photoacoustic microscopy of tyrosinase reporter gene in vivo. Journal of biomedical optics. 2011; 16

237. Paproski RJ, Li Y, Barber Q, Lewis JD, Campbell RE, Zemp R. Validating tyrosinase homologue melA as a photoacoustic reporter gene for imaging Escherichia coli. Journal of biomedical optics. 2015; 20

238. Paproski RJ, Forbrich AE, Wachowicz K, Hitt MM, Zemp RJ. Tyrosinase as a dual reporter gene for both photoacoustic and magnetic resonance imaging. Biomedical optics express. 2011; 2:771–780. [PubMed: 21483602]

239. Qin CX, Cheng K, Chen K, Hu X, Liu Y, Lan XL, Zhang YX, Liu HG, Xu YD, Bu LH, Su XH, Zhu XH, Meng SX, Cheng Z. Tyrosinase as a multifunctional reporter gene for Photoacoustic/MRI/PET triple modality molecular imaging. Sci Rep-Uk. 2013; 3

240. Paproski RJ, Heinmiller A, Wachowicz K, Zemp RJ. Multi-wavelength photoacoustic imaging of inducible tyrosinase reporter gene expression in xenograft tumors. Sci Rep-Uk. 2014; 4

241. Jathoul AP, Laufer J, Ogunlade O, Treeby B, Cox B, Zhang E, Johnson P, Pizzey AR, Philip B, Marafioti T, Lythgoe MF, Pedley RB, Pule MA, Beard P. Deep in vivo photoacoustic imaging of mammalian tissues using a tyrosinase-based genetic reporter. Nat Photonics. 2015; 9:239–246.

242. Urabe K, Aroca P, Tsukamoto K, Mascagna D, Palumbo A, Prota G, Hearing VJ. The inherent cytotoxicity of melanin precursors: a revision. Biochimica et Biophysica Acta (BBA)-Molecular Cell Research. 1994; 1221:272–278. [PubMed: 8167148]

243. Kirscher L, Dean-Ben XL, Scadeng M, Zaremba A, Zhang Q, Kober C, Fehm TF, Razansky D, Ntziachristos V, Stritzker J, Szalay AA. Doxycycline Inducible Melanogenic Vaccinia Virus as Theranostic Anti-Cancer Agent. Theranostics. 2015; 5:1045–1057. [PubMed: 26199644]

244. Feng HY, Xia XT, Li CJ, Song YL, Qin CX, Zhang YX, Lan XL. TYR as a multifunctional reporter gene regulated by the Tet-on system for multimodality imaging: an in vitro study. Sci Rep-Uk. 2015; 5

245. Jiang YY, Sigmund F, Reber J, Dean-Ben XL, Glasl S, Kneipp M, Estrada H, Razansky D, Ntziachristos V, Westmeyer GG. Violacein as a genetically-controlled, enzymatically amplified and photobleaching-resistant chromophore for optoacoustic bacterial imaging. Sci Rep-Uk. 2015; 5

246. Estrella V, Chen T, Lloyd M, Wojtkowiak J, Cornnell HH, Ibrahim-Hashim A, Bailey K, Balagurunathan Y, Rothberg JM, Sloane BF. Acidity generated by the tumor microenvironment drives local invasion. Cancer Res. 2013; 73:1524–1535. [PubMed: 23288510]

247. Horvath TD, Kim G, Kopelman R, Ashkenazi S. Ratiometric photoacoustic sensing of pH using a “sonophore”. Analyst. 2008; 133:747–749. [PubMed: 18493674]

248. Chatni MR, Yao JJ, Danielli A, Favazza CP, Maslov KI, Wang LHV. Functional photoacoustic microscopy of pH. Journal of biomedical optics. 2011; 16

249. Wang TT, Wang DG, Yu HJ, Wang MW, Liu JP, Feng B, Zhou FY, Yin Q, Zhang ZW, Huang YZ, Li YP. Intracellularly Acid-Switchable Multifunctional Micelles for Combinational Photo/Chemotherapy of the Drug-Resistant Tumor. Acs Nano. 2016; 10:3496–3508. [PubMed: 26866752]

250. Guha S, Shaw GK, Mitcham TM, Bouchard RR, Smith BD. Croconaine rotaxane for acid activated photothermal heating and ratiometric photoacoustic imaging of acidic pH. Chem Commun. 2016; 52:120–123.

251. Chen Q, Liu XD, Zeng JF, Cheng ZP, Liu Z. Albumin-NIR dye self-assembled nanoparticles for photoacoustic pH imaging and pH-responsive photothermal therapy effective for large tumors. Biomaterials. 2016; 98:23–30. [PubMed: 27177219]

252. Miao QQ, Lyu Y, Ding D, Pu KY. Semiconducting oligomer nanoparticles as an activatable photoacoustic probe with amplified brightness for in vivo imaging of pH. Adv Mater. 2016; 28:3662–3668. [PubMed: 27000431]

253. Huang GJ, Si Z, Yang SH, Li C, Xing D. Dextran based pH-sensitive near-infrared nanoprobe for in vivo differential-absorption dual-wavelength photoacoustic imaging of tumors. J Mater Chem. 2012; 22:22575–22581.

254. Song J, Kim J, Hwang S, Jeon M, Jeong S, Kim C, Kim S. “Smart” gold nanoparticles for photoacoustic imaging: an imaging contrast agent responsive to the cancer microenvironment and signal amplification via pH-induced aggregation. Chem Commun. 2016; 52:8287–8290.

255. Deán-Ben XL, Sela G, Lauri A, Kneipp M, Ntziachristos V, Westmeyer GG, Shoham S, Razansky D. Functional optoacoustic neuro-tomography (FONT) for scalable whole-brain monitoring of calcium indicators. Light: Science & Applications. 2016; 5:e16201.

256. Dana N, Fowler RA, Allen A, Zoldan J, Suggs L, Emelianov S. In vitro photoacoustic sensing of calcium dynamics with arsenazo III. Laser Phys Lett. 2016; 13

257. Gao L, Wang LD, Li CY, Liu Y, Ke HX, Zhang C, Wang LHV. Single-cell photoacoustic thermometry. Journal of biomedical optics. 2013; 18

258. Gao L, Zhang C, Li CY, Wang LHV. Intracellular temperature mapping with fluorescence-assisted photoacoustic-thermometry. Appl Phys Lett. 2013; 102

259. Razansky D, Harlaar NJ, Hillebrands JL, Taruttis A, Herzog E, Zeebregts CJ, van Dam GM, Ntziachristos V. Multispectral Optoacoustic Tomography of Matrix Metalloproteinase Activity in Vulnerable Human Carotid Plaques. Molecular Imaging and Biology. 2012; 14:277–285. [PubMed: 21720908]

260. Levi J, Kothapalli SR, Ma TJ, Hartman K, Khuri-Yakub BT, Gambhir SS. Design, Synthesis, and Imaging of an Activatable Photoacoustic Probe. Journal of the American Chemical Society. 2010; 132:11264–11269. [PubMed: 20698693]

261. Levi J, Kothapalli SR, Bohndiek S, Yoon JK, Dragulescu-Andrasi A, Nielsen C, Tisma A, Bodapati S, Gowrishankar G, Yan XR, Chan C, Starcevic D, Gambhir SS. Molecular Photoacoustic Imaging of Follicular Thyroid Carcinoma. Clin Cancer Res. 2013; 19:1494–1502. [PubMed: 23349314]

262. Li WJ, Zheng CF, Pan ZY, Chen C, Hu DH, Gao GH, Kang SD, Cui HD, Gong P, Cai LT. Smart hyaluronidase-actived theranostic micelles for dual-modal imaging guided photodynamic therapy. Biomaterials. 2016; 101:10–19. [PubMed: 27262027]

263. Li H, Zhang P, Smaga LP, Hoffman RA, Chan J. Photoacoustic Probes for Ratiometric Imaging of Copper(II). Journal of the American Chemical Society. 2015; 137:15628–15631. [PubMed: 26652006]

264. Pang GA, Bay E, DEÁN-BEN X, Razansky D. Three-Dimensional Optoacoustic Monitoring of Lesion Formation in Real Time During Radiofrequency Catheter Ablation. J Cardiovasc Electr. 2015; 26:339–345.

265. Gray J, Dana N, Dextraze K, Maier F, Emelianov S, Bouchard R. Multi-Wavelength Photoacoustic Visualization of High Intensity Focused Ultrasound Lesions. Ultrasonic Imaging. 2015 0161734615593747.

266. Petrova, EV., Motamedi, M., Oraevsky, AA., Ermilov, SA. SPIE BiOS. International Society for Optics and Photonics; 2016. In vivo cryoablation of prostate tissue with temperature monitoring by optoacoustic imaging. pp. 97080G–97080G–97088

267. Fehm TF, Deán-Ben XL, Schaur P, Sroka R, Razansky D. Volumetric optoacoustic imaging feedback during endovenous laser therapy–an ex vivo investigation. Journal of biophotonics. 2015

268. Chen YS, Frey W, Walker C, Aglyamov S, Emelianov S. Sensitivity enhanced nanothermal sensors for photoacoustic temperature mapping. Journal of biophotonics. 2013; 6:534–542. [PubMed: 23450812]

269. Ng KK, Shakiba M, Huynh E, Weersink RA, Roxin A, Wilson BC, Zheng G. Stimuli-Responsive Photoacoustic Nanoswitch for in Vivo Sensing Applications. Acs Nano. 2014; 8:8363–8373. [PubMed: 25046406]

270. Gottschalk S, Estrada H, Degtyaruk O, Rebling J, Klymenko O, Rosemann M, Razansky D. Short and long-term phototoxicity in cells expressing genetic reporters under nanosecond laser exposure. Biomaterials. 2015; 69:38–44. [PubMed: 26280948]

271. Li CY, Zhang C, Gao L, Garcia-Uribe A, Wang LHV. Photoacoustic recovery after photothermal bleaching in living cells. Journal of biomedical optics. 2013; 18

272. Yao JJ, Kaberniuk AA, Li L, Shcherbakova DM, Zhang RY, Wang LD, Li G, Verkhusha VV, Wang LHV. Multiscale photoacoustic tomography using reversibly switchable bacterial phytochrome as a near-infrared photochromic probe. Nature methods. 2016; 13:67-+. [PubMed: 26550774]

273. Dean-Ben XL, Stiel AC, Jiang YY, Ntziachristos V, Westmeyer GG, Razansky D. Light fluence normalization in turbid tissues via temporally unmixed multispectral optoacoustic tomography. Opt Lett. 2015; 40:4691–4694. [PubMed: 26469596]

274. Galanzha EI, Nedosekin DA, Sarimollaoglu M, Orza AI, Biris AS, Verkhusha VV, Zharov VP. Photoacoustic and photothermal cytometry using photoswitchable proteins and nanoparticles with ultrasharp resonances (vol 8, pg 81, 2015). Journal of biophotonics. 2015; 8:687–687. [PubMed: 26246361]

275. Ashkenazi S, Huang SW, Horvath T, Koo YEL, Kopelman R. Photoacoustic probing of fluorophore excited state lifetime with application to oxygen sensing (vol 13, art no 034023, 2008). Journal of biomedical optics. 2008; 13

276. Mark J, Schmitt FJ, Theiss C, Dortay H, Friedrich T, Laufer J. Photoacoustic imaging of fluorophores using pump-probe excitation. Biomedical optics express. 2015; 6:2522–2535. [PubMed: 26203378]

277. Dove JD, Murray TW, Borden MA. Enhanced photoacoustic response with plasmonic nanoparticle-templated microbubbles. Soft Matter. 2013; 9:7743–7750.

278. Arnal B, Perez C, Wei C-W, Xia J, Lombardo M, Pelivanov I, Matula TJ, Pozzo LD, O'Donnell M. Sono-photoacoustic imaging of gold nanoemulsions: Part I. Exposure thresholds. Photoacoustics. 2015; 3:3–10. [PubMed: 25893169]

279. Arnal B, Wei C-W, Perez C, Nguyen T-M, Lombardo M, Pelivanov I, Pozzo LD, O'Donnell M. Sono-photoacoustic imaging of gold nanoemulsions: Part II. Real time imaging. Photoacoustics. 2015; 3:11–19. [PubMed: 25893170]

280. Laufer J, Jathoul A, Pule M, Beard P. *In vitro* characterization of genetically expressed absorbing proteins using photoacoustic spectroscopy. Biomedical optics express. 2013; 4:2477–2490. [PubMed: 24298408]

281. Niemz, MH. Laser-tissue interactions: fundamentals and applications. Springer Science & Business Media; 2013.

282. Gao L, Wang LD, Li CY, Garcia-Uribe A, Wang LHV. Photothermal bleaching in time-lapse photoacoustic microscopy. Journal of biophotonics. 2013; 6:543–548. [PubMed: 23184422]

283. Chang SS, Shih CW, Chen CD, Lai WC, Wang CRC. The shape transition of gold nanorods. Langmuir. 1999; 15:701–709.

284. Nienhaus GU. Chromophore photophysics and dynamics in fluorescent proteins of the GFP family. Eur Biophys J Biophy. 2015; 44:S85–S85.
285. Liao ZX, Li YC, Lu HM, Sung HW. A genetically-encoded KillerRed protein as an intrinsically generated photosensitizer for photodynamic therapy. Biomaterials. 2014; 35:500–508. [PubMed: 24112805]
286. Gong H, Peng R, Liu Z. Carbon nanotubes for biomedical imaging: The recent advances. Adv Drug Deliver Rev. 2013; 65:1951–1963.
287. Kaur R, Badea I. Nanodiamonds as novel nanomaterials for biomedical applications: drug delivery and imaging systems. Int J Nanomed. 2013; 8:203–220.
288. Zhu Y, Li J, Li WX, Zhang Y, Yang XF, Chen N, Sun YH, Zhao Y, Fan CH, Huang Q. The Biocompatibility of Nanodiamonds and Their Application in Drug Delivery Systems. Theranostics. 2012; 2:302–312. [PubMed: 22509196]
289. Chen YS, Frey W, Kim S, Homan K, Kruizinga P, Sokolov K, Emelianov S. Enhanced thermal stability of silica-coated gold nanorods for photoacoustic imaging and image-guided therapy. Optics express. 2010; 18:8867–8877. [PubMed: 20588732]
290. Khlebtsov N, Dykman L. Biodistribution and toxicity of engineered gold nanoparticles: a review of in vitro and in vivo studies. Chem Soc Rev. 2011; 40:1647–1671. [PubMed: 21082078]
291. Tam JM, Murthy AK, Ingram DR, Nguyen R, Sokolov KV, Johnston KP. Kinetic Assembly of Near-IR-Active Gold Nanoclusters Using Weakly Adsorbing Polymers to Control the Size. Langmuir. 2010; 26:8988–8999. [PubMed: 20361735]
292. Galanzha EI, Viegas MG, Malinsky TI, Melerzanov AV, Juratli MA, Sarimollaoglu M, Nedosekin DA, Zharov VP. In vivo acoustic and photoacoustic focusing of circulating cells. Sci Rep-Uk. 2016; 6
293. Brunker J, Beard P. Acoustic resolution photoacoustic Doppler velocimetry in blood-mimicking fluids. Sci Rep-Uk. 2016; 6
294. Galanzha EI, Shashkov EV, Kelly T, Kim JW, Yang LL, Zharov VP. In vivo magnetic enrichment and multiplex photoacoustic detection of circulating tumour cells. Nature Nanotechnology. 2009; 4:855–860.
295. Brunker J, Beard P. Velocity measurements in whole blood using acoustic resolution photoacoustic Doppler. Biomedical optics express. 2016; 7:2789–2806. [PubMed: 27446707]
296. Strohm EM, Berndl ESL, Kolios MC. Probing Red Blood Cell Morphology Using High-Frequency Photoacoustics. Biophys J. 2013; 105:59–67. [PubMed: 23823224]
297. Deán-Ben XL, Ding L, Razansky D. Dynamic particle enhancement in limited-view optoacoustic tomography. Optics Letters. 2017; 42:827–830. [PubMed: 28198875]
298. Deng Z, Wang Z, Yang X, Luo Q, Gong H. In vivo imaging of hemodynamics and oxygen metabolism in acute focal cerebral ischemic rats with laser speckle imaging and functional photoacoustic microscopy. Journal of biomedical optics. 2012; 17:0814151–0814159.
299. Kneipp M, Turner J, Hambauer S, Krieg SM, Lehmberg J, Lindauer U, Razansky D. Functional Real-Time Optoacoustic Imaging of Middle Cerebral Artery Occlusion in Mice. PloS one. 2014; 9
300. Liao LD, Liu YH, Lai HY, Bandla A, Shih YYI, Chen YY, Thakor NV. Rescue of cortical neurovascular functions during the hyperacute phase of ischemia by peripheral sensory stimulation. Neurobiol Dis. 2015; 75:53–63. [PubMed: 25573087]
301. Daly SM, Leahy MJ. “Go with the flow”: A review of methods and advancements in blood flow imaging. Journal of biophotonics. 2013; 6:217–255. [PubMed: 22711377]
302. Taruttis A, Morscher S, Burton NC, Razansky D, Ntziachristos V. Fast multispectral optoacoustic tomography (MSOT) for dynamic imaging of pharmacokinetics and biodistribution in multiple organs. PloS one. 2012; 7:e30491. [PubMed: 22295087]
303. Dima A, Gateau J, Claussen J, Wilhelm D, Ntziachristos V. Optoacoustic imaging of blood perfusion: Techniques for intraoperative tissue viability assessment. Journal of biophotonics. 2013; 6:485–492. [PubMed: 23494993]
304. Hu S. Listening to the Brain With Photoacoustics. Ieee J Sel Top Quant. 2016; 22:1–10.

305. Liao LD, Lin CT, Shih YYI, Duong TQ, Lai HY, Wang PH, Wu R, Tsang S, Chang JY, Li ML, Chen YY. Transcranial imaging of functional cerebral hemodynamic changes in single blood vessels using in vivo photoacoustic microscopy. J Cerebr Blood F Met. 2012; 32:938–951.

306. Yao JJ, Xia J, Maslov KI, Nasiriavanaki M, Tsytsarev V, Demchenko AV, Wang LV. Noninvasive photoacoustic computed tomography of mouse brain metabolism in vivo. NeuroImage. 2013; 64:257–266. [PubMed: 22940116]

307. Tang JB, Xi L, Zhou JL, Huang H, Zhang T, Carney PR, Jiang HB. Noninvasive high-speed photoacoustic tomography of cerebral hemodynamics in awake-moving rats. J Cerebr Blood F Met. 2015; 35:1224–1232.

308. Burton NC, Patel M, Morscher S, Driessen WHP, Claussen J, Beziere N, Jetzfellner T, Taruttis A, Razansky D, Bednar B, Ntziachristos V. Multispectral Opto-acoustic Tomography (MSOT) of the Brain and Glioblastoma Characterization. NeuroImage. 2013; 65:522–528. [PubMed: 23026761]

309. Akerboom J, Vélez Rivera JD, Rodríguez Guilbe MM, Alfaro Malavé EC, Hernandez HH, Tian L, Hires SA, Marvin JS, Looger LL, Schreiter ER. Crystal structures of the GCaMP calcium sensor reveal the mechanism of fluorescence signal change and aid rational design. J Biol Chem. 2009; 284:6455–6464. [PubMed: 19098007]

310. Dortay, H., Märk, J., Wagener, A., Zhang, E., Grötzinger, C., Hildebrandt, P., Friedrich, T., Laufer, J. SPIE BiOS. International Society for Optics and Photonics; 2016. Dual-wavelength photoacoustic imaging of a photoswitchable reporter protein. pp. 970820–970820–970827

311. Gurka MK, Pender D, Chuong P, Fouts BL, Sobelov A, McNally MW, Mezera M, Woo SY, McNally LR. Identification of pancreatic tumors in vivo with ligand-targeted, pH responsive mesoporous silica nanoparticles by multispectral optoacoustic tomography. J Control Release. 2016; 231:60–67. [PubMed: 26763377]

312. Ermolayev V, Dean-Ben XL, Mandal S, Ntziachristos V, Razansky D. Simultaneous visualization of tumour oxygenation, neovascularization and contrast agent perfusion by real-time three-dimensional optoacoustic tomography. European radiology. 2016; 26:1843–1851. [PubMed: 26334513]

313. Egusquiaguirre SP, Beziere N, Pedraz JL, Hernández RM, Ntziachristos V, Igartua M. Optoacoustic imaging enabled biodistribution study of cationic polymeric biodegradable nanoparticles. Contrast Media Mol Imag. 2015; 10:421–427.

314. Comenge J, Fragueiro O, Sharkey J, Taylor A, Held M, Burton NC, Park BK, Wilm B, Murray P, Brust M, Levy R. Preventing Plasmon Coupling between Gold Nanorods Improves the Sensitivity of Photoacoustic Detection of Labeled Stem Cells in Vivo. Acs Nano. 2016; 10:7106–7116. [PubMed: 27308890]

315. Ding K, Zeng JF, Jing LH, Qiao RR, Liu CY, Jiao MX, Li Z, Gao MY. Aqueous synthesis of PEGylated copper sulfide nanoparticles for photoacoustic imaging of tumors. Nanoscale. 2015; 7:11075–11081. [PubMed: 26055816]

316. Chen AP, Xu C, Li M, Zhang HL, Wang DC, Xia M, Meng G, Kang B, Chen HY, Wei JW. Photoacoustic “nanobombs” fight against undesirable vesicular compartmentalization of anticancer drugs. Sci Rep-Uk. 2015; 5

317. Ruan Q, Xi L, Boye SL, Han S, Chen ZJ, Hauswirth WW, Lewin AS, Boulton ME, Law BK, Jiang WG. Development of an anti-angiogenic therapeutic model combining scAAV2-delivered siRNAs and noninvasive photoacoustic imaging of tumor vasculature development. Cancer Lett. 2013; 332:120–129. [PubMed: 23196055]

318. Bell MAL, Kuo NP, Song DY, Kang JU, Boctor EM. In vivo visualization of prostate brachytherapy seeds with photoacoustic imaging. Journal of biomedical optics. 2014; 19:126011–126011. [PubMed: 25531797]

319. Xie B, Stammes MA, van Driel PB, Cruz LJ, Knol-Blankevoort VT, Löwik MA, Mezzanotte L, Que I, Chan A, van den Wijngaard JP. Necrosis avid near infrared fluorescent cyanines for imaging cell death and their use to monitor therapeutic efficacy in mouse tumor models. Oncotarget. 2015; 6:39036. [PubMed: 26472022]

320. Zhang C, Zhang YS, Yao DK, Xia YN, Wang LHV. Label-free photoacoustic microscopy of cytochromes. Journal of biomedical optics. 2013; 18

321. Kneipp M, Estrada H, Lauri A, Turner J, Ntziachristos V, Westmeyer GG, Razansky D. Volumetric tracking of migratory melanophores during zebrafish development by optoacoustic microscopy. Mech Develop. 2015; 138:300–304.
322. Laufer J, Norris F, Cleary J, Zhang E, Treeby B, Cox B, Johnson P, Scambler P, Lythgoe M, Beard P. In vivo photoacoustic imaging of mouse embryos. Journal of biomedical optics. 2012; 17
323. Ripoll J, Koberstein-Schwarz B, Ntziachristos V. Unleashing Optics and Optoacoustics for Developmental Biology. Trends Biotechnol. 2015; 33:679–691. [PubMed: 26435161]
324. Lin HCA, Chekkoury A, Omar M, Schmitt-Manderbach T, Koberstein-Schwarz B, Mappes T, Lopez-Schier H, Razansky D, Ntziachristos V. Selective plane illumination optical and optoacoustic microscopy for postembryonic imaging. Laser Photonics Rev. 2015; 9:L29–L34.
325. Lin R, Chen J, Wang H, Yan M, Zheng W, Song L. Longitudinal label-free optical-resolution photoacoustic microscopy of tumor angiogenesis in vivo. Quantitative imaging in medicine and surgery. 2014; 5:23–29.
326. Hu S, Yan P, Maslov K, Lee J-M, Wang LV. Intravital imaging of amyloid plaques in a transgenic mouse model using optical-resolution photoacoustic microscopy. Opt Lett. 2009; 34:3899–3901. [PubMed: 20016651]
327. Ghazaryan A, Omar M, Tserevelakis GJ, Ntziachristos V. Optoacoustic detection of tissue glycation. Biomedical optics express. 2015; 6:3149–3156. [PubMed: 26417487]
328. Heijblom M, Piras D, Brinkhuis M, Van Hespen J, Van den Engh F, Van der Schaaf M, Klaase J, van Leeuwen T, Steenbergen W, Manohar S. Photoacoustic image patterns of breast carcinoma and comparisons with Magnetic Resonance Imaging and vascular stained histopathology. Sci Rep-Uk. 2015; 5
329. Deán-Ben XL, Razansky D. Functional optoacoustic human angiography with handheld video rate three dimensional scanner. Photoacoustics. 2013; 1:68–73. [PubMed: 25302151]
330. Merčep E, Jeng G, Morscher S, Li P-C, Razansky D. Hybrid optoacoustic tomography and ultrasonography using concave arrays. IEEE Trans Untrason Ferr Freq Cont. 2015; 62:1651–1661.
331. Taruttis A, Timmermans AC, Wouters PC, Kacprowicz M, van Dam GM, Ntziachristos V. Optoacoustic Imaging of Human Vasculature: Feasibility by Using a Handheld Probe. Radiology. 2016; 281:256–263. [PubMed: 27379543]
332. Manohar S, Kharine A, van Hespen JCG, Steenbergen W, van Leeuwen TG. Photoacoustic mammography laboratory prototype: imaging of breast tissue phantoms. Journal of biomedical optics. 2004; 9:1172–1181. [PubMed: 15568937]
333. Ermilov SA, Khamapirad T, Conjusteau A, Leonard MH, Lacewell R, Mehta K, Miller T, Oraevsky AA. Laser optoacoustic imaging system for detection of breast cancer. Journal of biomedical optics. 2009; 14
334. Valluru KS, Wilson KE, Willmann JK. Photoacoustic Imaging in Oncology: Translational Preclinical and Early Clinical Experience. Radiology. 2016; 280:332–349. [PubMed: 27429141]
335. He H, Wissmeyer G, Ovsepian SV, Buehler A, Ntziachristos V. Hybrid optical and acoustic resolution optoacoustic endoscopy. Opt Lett. 2016; 41:2708–2710. [PubMed: 27304269]
336. Jansen K, Wu M, van der Steen AF, van Soest G. Photoacoustic imaging of human coronary atherosclerosis in two spectral bands. Photoacoustics. 2014; 2:12–20. [PubMed: 25302152]
337. Karpiouk AB, Wang B, Amirian J, Smalling RW, Emelianov SY. Feasibility of in vivo intravascular photoacoustic imaging using integrated ultrasound and photoacoustic imaging catheter. Journal of biomedical optics. 2012; 17:0960081–0960086.
338. Yang J-M, Favazza C, Chen R, Yao J, Cai X, Maslov K, Zhou Q, Shung KK, Wang LV. Simultaneous functional photoacoustic and ultrasonic endoscopy of internal organs in vivo. Nature medicine. 2012; 18:1297–1302.
339. Ford SJ, Bigliardi PL, Sardella TC, Urich A, Burton NC, Kacprowicz M, Bigliardi M, Olivo M, Razansky D. Structural and functional analysis of intact hair follicles and pilosebaceous units by volumetric multispectral optoacoustic tomography. J Invest Dermatol. 2016; 136:753–761. [PubMed: 26743603]

340. Bell AG. On the production and reproduction of sound by light. American Journal of Science. 1880:305–324.

341. Beard P. Biomedical photoacoustic imaging. Interface Focus. 2011; 1:602–631. [PubMed: 22866233]

342. Kong L, Tang J, Little JP, Yu Y, Lämmermann T, Lin CP, Germain RN, Cui M. Continuous volumetric imaging via an optical phase-locked ultrasound lens. Nature methods. 2015; 12:759–762. [PubMed: 26167641]

343. Bouchard MB, Voleti V, Mendes CS, Lacefield C, Grueber WB, Mann RS, Bruno RM, Hillman EMC. Swept confocally-aligned planar excitation (SCAPE) microscopy for high-speed volumetric imaging of behaving organisms. Nat Photonics. 2015; 9:113–119. [PubMed: 25663846]

344. Prevedel R, Yoon YG, Hoffmann M, Pak N, Wetzstein G, Kato S, Schrodel T, Raskar R, Zimmer M, Boyden ES, Vaziri A. Simultaneous whole-animal 3D imaging of neuronal activity using light-field microscopy. Nature methods. 2014; 11:727-U161. [PubMed: 24836920]

345. Bosshard SC, Stuker F, von Deuster C, Schroeter A, Rudin M. BOLD fMRI of C-Fiber Mediated Nociceptive Processing in Mouse Brain in Response to Thermal Stimulation of the Forepaws. PloS one. 2015; 10

346. Moeller S, Yacoub E, Olman CA, Auerbach E, Strupp J, Harel N, Ugurbil K. Multiband Multislice GE-EPI at 7 Tesla, With 16-Fold Acceleration Using Partial Parallel Imaging With Application to High Spatial and Temporal Whole-Brain FMRI. Magnet Reson Med. 2010; 63:1144–1153.

347. Eggebrecht AT, Ferradal SL, Robichaux-Viehoever A, Hassanpour MS, Dehghani H, Snyder AZ, Hershey T, Culver JP. Mapping distributed brain function and networks with diffuse optical tomography. Nat Photonics. 2014; 8:448–454. [PubMed: 25083161]

348. Jiang H, Iftimia N, Xu Y, Klove KL. Near-infrared optical imaging of the breast with model-based reconstruction. Acad Radiol. 2002; 9:186–194. [PubMed: 11918371]

349. Mace E, Montaldo G, Cohen I, Baulac M, Fink M, Tanter M. Functional ultrasound imaging of the brain. Nature methods. 2011; 8:662–U685. [PubMed: 21725300]

350. Cherry SR. Multimodality in vivo imaging systems: Twice the power or double the trouble? Annual Review of Biomedical Engineering. 2006; 8:35–62.

351. Yao J, Wang LV. Sensitivity of photoacoustic microscopy. Photoacoustics. 2014; 2:87–101. [PubMed: 25302158]

352. Yuan Z, Zhang Q, Jiang H. Simultaneous reconstruction of acoustic and optical properties of heterogeneous media by quantitative photoacoustic tomography. Opt Exp. 2006; 14:6749–6754.

353. Deán-Ben XL, Ntziachristos V, Razansky D. Effects of small variations of speed of sound in optoacoustic tomographic imaging. Med Phys. 2014; 41:073301. [PubMed: 24989414]

354. Deán-Ben XL, Ma R, Razansky D, Ntziachristos V. Statistical approach for optoacoustic image reconstruction in the presence of strong acoustic heterogeneities. IEEE Transactions on Medical Imaging. 2011; 30:401–408. [PubMed: 20876007]

355. Yin L, Wang Q, Zhang Q, Jiang H. Tomographic imaging of absolute optical absorption coefficient in turbid media using combined photoacoustic and diffusing light measurements. Opt Lett. 2007; 32:2556–2558. [PubMed: 17767303]

356. Yuan Z, Jiang H. Simultaneous recovery of tissue physiological and acoustic properties and uniqueness in multi-spectral photoacoustic tomography. Opt Lett. 2009; 34:1714–1716. [PubMed: 19488158]

357. Shaner NC, Patterson GH, Davidson MW. Advances in fluorescent protein technology. J Cell Science. 2007; 120:4247–4260. [PubMed: 18057027]

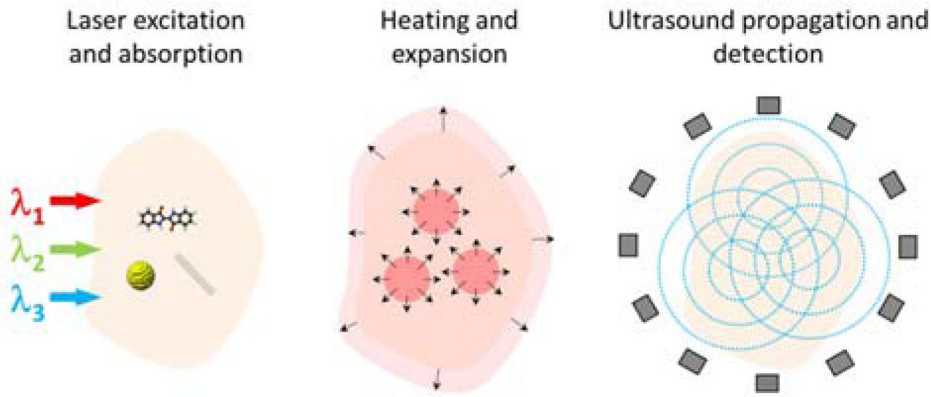

Fig 1.

Schematic illustration of the optoacoustic signal generation and detection. Short light pulses at selected optical wavelengths are absorbed by the tissue chromophores and contrast agents, leading to instantaneous heating and thermal expansion. As a result, ultrasound pressure waves are excited and measured around the imaged object.

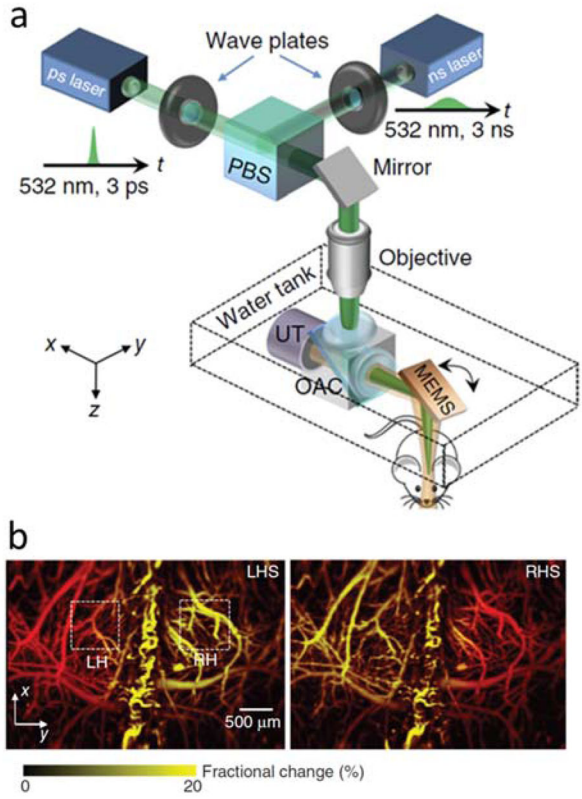

Fig 2.

Dynamic imaging with optical-resolution photoacoustic microscopy (OR-PAM). (a) Lay-out of the imaging system. (b) Fractional change in the optoacoustic images of the left (LH) and right (RH) hemispheres of the mouse brain in response to left (LHS – left) and right (RHS – right) hind limb stimulation. Adapted with permission from [22]. © 2015 - Macmillan Publishers Ltd.

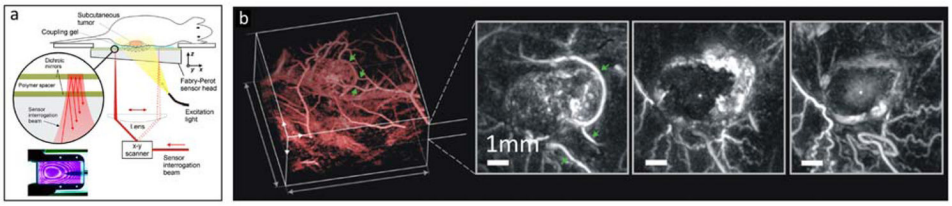

Fig 3.

All-optical optoacoustic scanner based on a Fabry-Pérot ultrasound sensor. (a) Lay-out of the imaging system. (b) Longitudinal optoacoustic images of tumor vasculature showing the effect of the vascular disrupting therapeutic agent OXi4503 before (left), 24 hours (center) and 48 hours (right) after treatment. Adapted with permission from [53], © 2012 Society of Photo Optical Instrumentation Engineers.

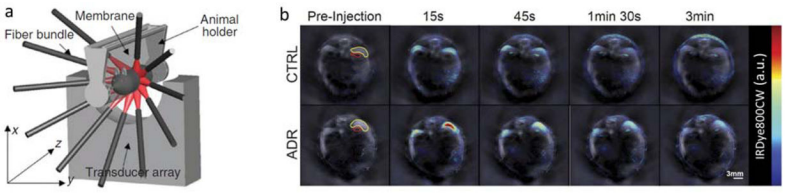

Fig 4.

Small animal imaging with multi-spectral optoacoustic tomography (MSOT). (a) Schematic of the real-time cross-sectional imaging system. Adapted with permission from [88]. © 2011 - Macmillan Publishers Ltd. (b) Time-lapse MSOT images of a mouse administered with an anthracycline antibiotic adriamycin (ADR) (bottom) and control mouse (top) before and after injection of the near-infrared dye IRDye800CW. Gray-scale background represents single-wavelength optoacoustic reconstructions whereas the spectrally-unmixed dye distribution is superimposed in color. Figure is used under the Creative Commons Attribution 4.0 International License from [94]. A scale bar was added and image identification was altered.

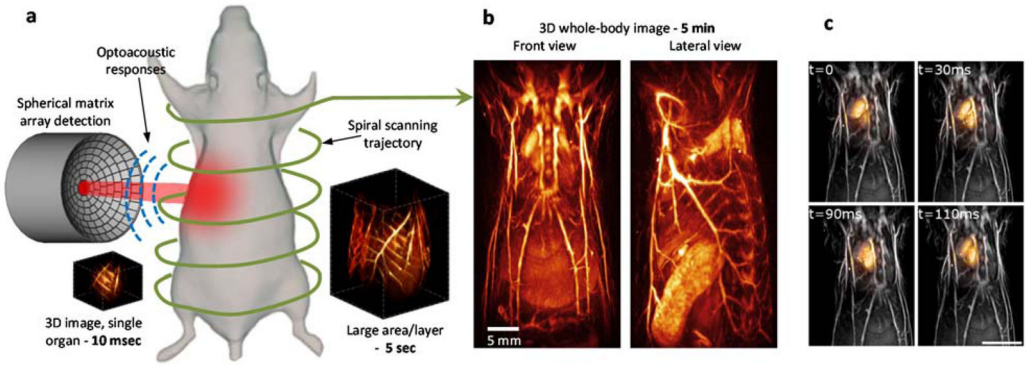

Fig 5.

Multi-scale four dimensional (4D) optoacoustic imaging. (a) Lay-out of the spiral volumetric optoacoustic tomography (SVOT) imaging concept. Whole-body tomographic data acquisition is performed along a spiral (helical) scanning trajectory by means of a spherical matrix ultrasound detection array, further capable of real-time 3D imaging. (b) It takes about 5 minutes to acquire whole-body image data by combining all images acquired along the entire spiral trajectory. Adapted with permission from [73] © 2017 - Macmillan Publishers Ltd. (c) Whole-body optoacoustic images (gray scale) superimposed with images of a beating heart (orange) acquired in real time for a single position of the spherical array. Scale bar – 1cm. Adapted with permission from [104] © 2016 Optical Society of America.

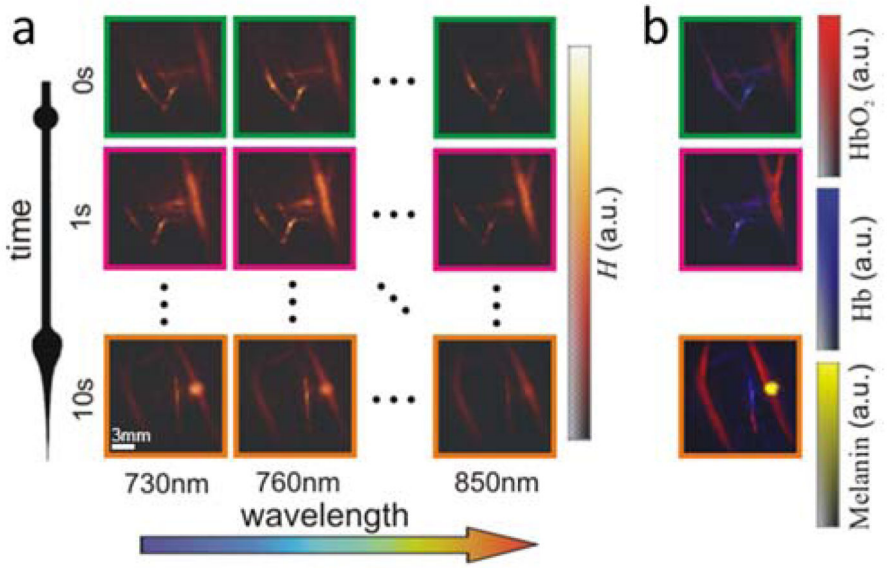

Fig 6.

Five dimensional (5D) optoacoustic imaging of the forearm of a healthy volunteer. (a) The imaging concept is based on per-pulse tuning of the laser wavelength and rapid collection of multi-spectral volumetric data using a handheld spherical matrix array scanner. (b) Spectral unmixing of the 3D images for different instants and wavelengths renders the distribution of different tissue chromophores in real time. Adapted with permission from [11], © 2014 - Macmillan Publishers Ltd.

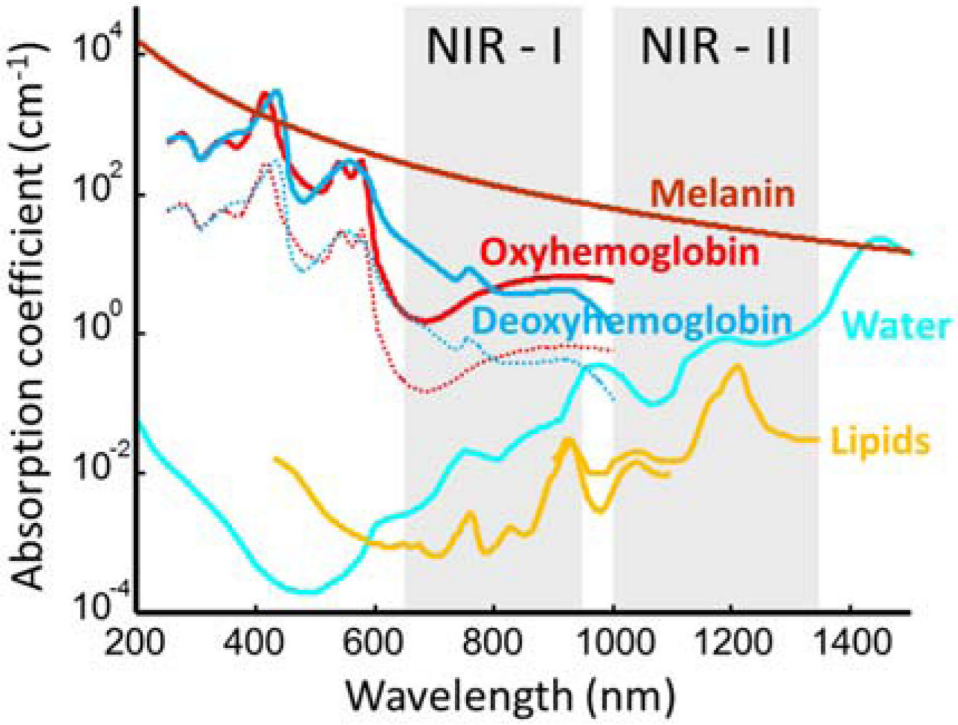

Fig 7.

Optical absorption spectra of major endogenous chromophores at typical concentrations occurring in living mammalian tissues. Melanin spectrum (brown) is shown for typical concentrations in the skin [122]; haemoglobin (red – oxygenated, blue – deoxygenated) for typical concentrations in whole blood (150 g/l – continuous lines) and average soft tissues (15 g/l – dashed lines) [123]; water (cyan) for a typical concentration of 80% by volume in soft tissues [124]; lipids (yellow) for a concentration of 20% by volume [125–126]. The first (NIR – I) and second (NIR – II) windows [127], where optical absorption is minimized, are indicated.

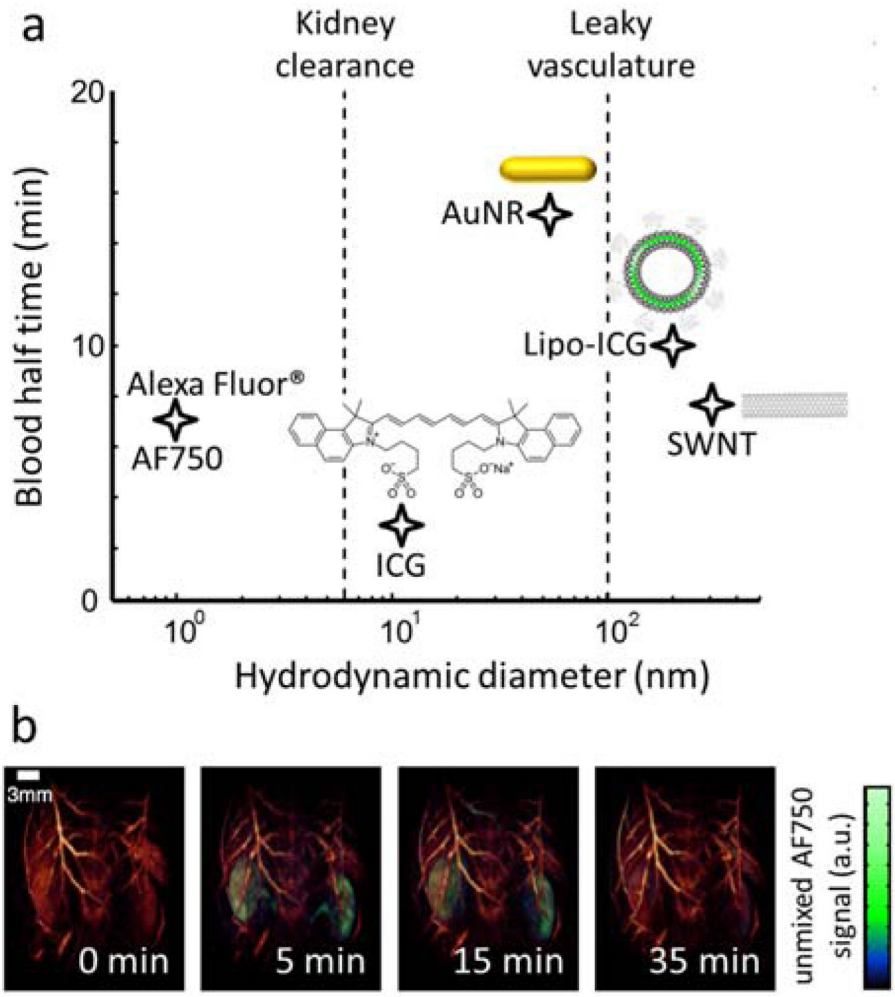

Fig 8.

Clearance constants of the common optoacoustic contrast agents from the blood circulation. (a) Blood half-life versus hydrodynamic diameter are shown for AF750 [73]; ICG [137] (note that ICG small molecules bind to albumin in blood, resulting in a hydrodynamic diameter of 11 nm that prevents kidney clearance [138]); gold nanorods (AuNR) [139]; liposomal ICG (Lipo-ICG) [137] and single-walled carbon nanotubes (SWNT) [140]. (b) Renal clearance of AF750 as visualized with spiral volumetric optoacoustic tomography (SVOT). Adapted with permission from [73] © 2017 - Macmillan Publishers Ltd.

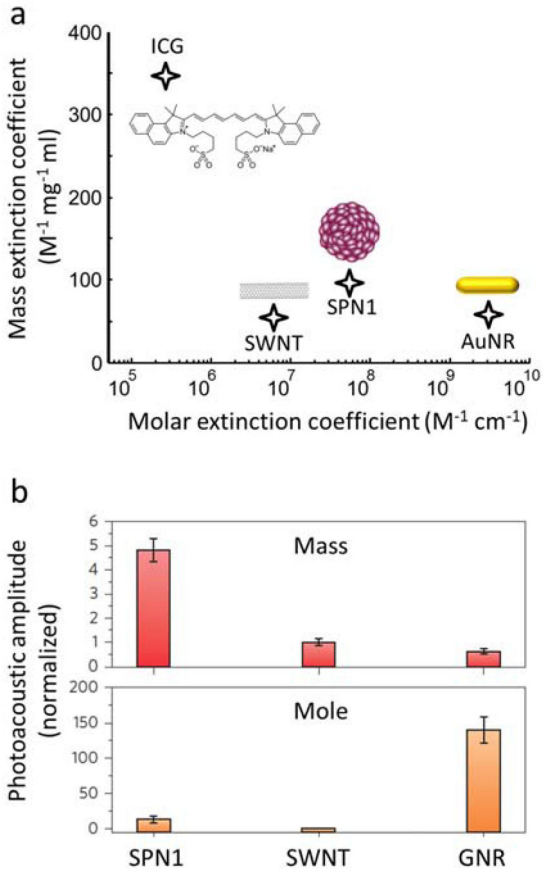

Fig 9.

Relation between the mass and molar extinctions of the agent and the generated optoacoustic signal. (a) Mass versus molar extinction for some commonly used optoacoustic contrast agents: small-molecule-based ICG [123]; single walled carbon nanotubes (SWNT) [145]; semiconducting polymer particles (SPN1) [145]; gold nanorods (AuNR) [145]. The data is provided at the peak absorption wavelengths. (b) Comparison of the generated optoacoustic signals per mass and per molar concentration for the different types of nanoparticles. Adapted with permission from [145]. © 2014 - Macmillan Publishers Ltd.

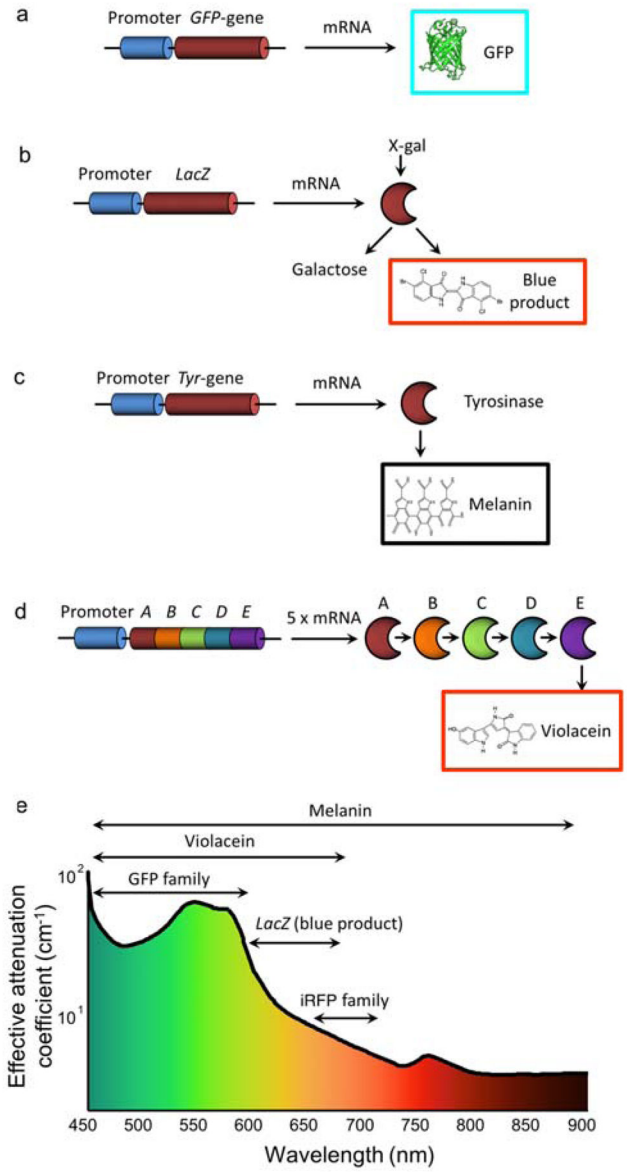

Fig 10.

Genetic labeling approaches in optoacoustic imaging. (a) Green fluorescent protein (GFP) synthetized directly from the GFP gene using mRNA. (b) Blue product (5,5′-dibromo-4,4′-dichloro-indigo) generated by hydrolysis of 5-bromo-4-chloro-3-indolyl-b-D-galactoside (X-gal) and catalyzed by the β-galactosidase enzyme. (c) Melanin enzymatically produced from endogenous tyrosine. (d) Violacein produced from the oxidative conversion of endogenous L-tryptophan by a 5-step enzymatic reaction. (e) Wavelength range covered by optoacoustic genetic reporters plotted along with the average optical attenuation in soft tissues. Reproduced with permission from [128]. © 2013 IOP Publishing.

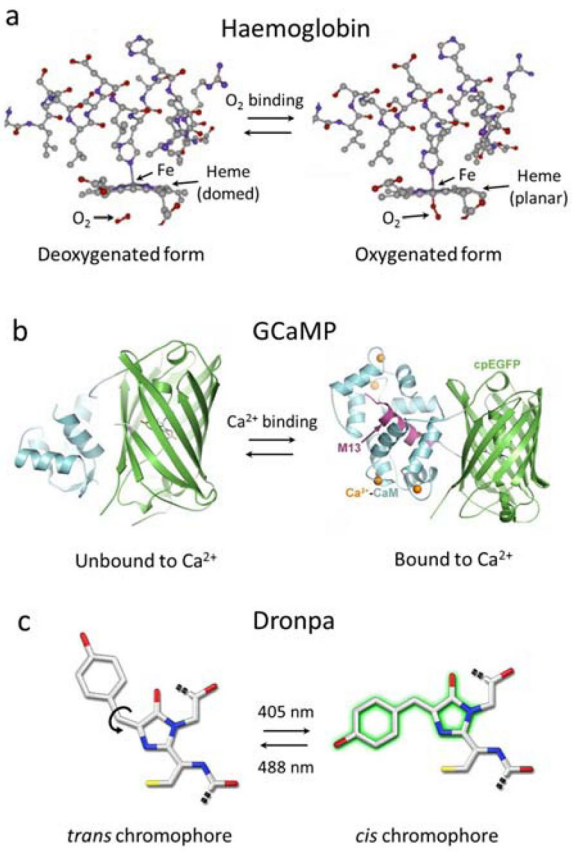

Fig 11.

Examples of molecular conformational changes leading to changes in the optical absorption spectrum that can be exploited for optoacoustic molecular sensing. (a) The heme group of haemoglobin changes its configuration when oxygen binds to iron. (b) The calcium-binding messenger calmodulin (CaM) in the genetically-encoded calcium indicator GCaMP undergoes a conformational change when calcium is present. Figure is used under the Creative Commons Attribution 4.0 International License from [309]. (c) The fluorescent protein Dronpa can be switched between its *cis* and *trans* conformations using light at different wavelengths. Adapted with permission from [357]. © 2007 The Company of Biologists Ltd.

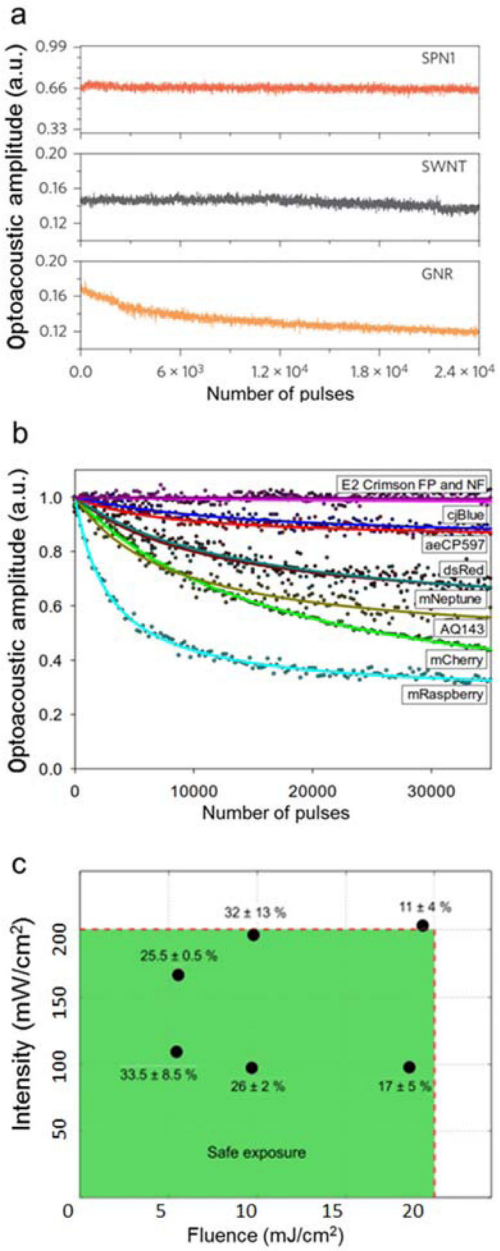

Fig 12.

Photodegradation of optoacoustic agents under nanosecond light exposure. (a) Signal decline in semiconducting polymer particles (SPN1), single walled carbon nanotubes (SWNT) and gold nanorods (GNR) due to exposure to pulsed laser radiation (9 mJ/cm^2 fluence), indicating their susceptibility to laser-induced deformation. Adapted with permission from [145]. © 2014 - Macmillan Publishers Ltd. (b) Photobleaching of fluorescent proteins and chromoproteins under prolonged exposure to nanosecond laser pulses. The fluence at the sample ranged from 1.5 to 1.7 mJ/cm^2. Adapted with permission from [280]. © 2013 Optical Society of America. (c) Loss of fluorescence signal (shown in %) due to photobleaching of mCherry-expressing cells under different illumination

conditions (average intensity and fluence) within ANSI exposure limits for 10 second exposure with 10000 pulses. Adapted with permission from [270]. © 2015 Elsevier.

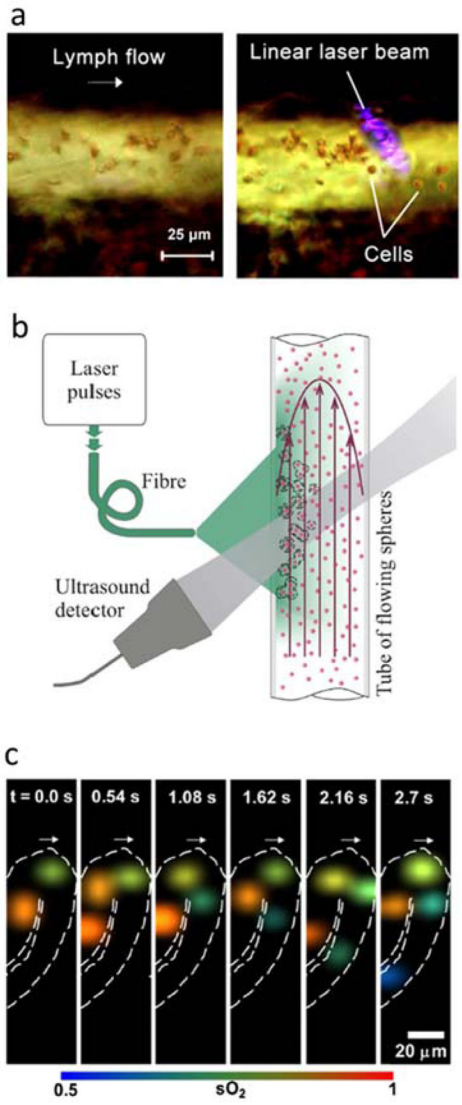

Fig 13.

Optoacoustic tracking of moving cells. (a) Cells in lymph flow of a mouse mesentery vessel before (left) and after (right) being trapped with gradient acoustic forces induced by optoacoustic waves generated by irradiation with a linear laser beam. Adapted with permission from [292]. © 2016 - Macmillan Publishers Ltd. (b) Optoacoustic set-up for measuring the flow velocity of cells via time correlation of the optoacoustic signals generated by two consecutive laser pulses. Adapted with permission from [293]. © 2016 - Macmillan Publishers Ltd. (c) Selected time-lapse images showing the oxygen saturation of individual red blood cells in cuticle capillaries obtained with high-speed optical-resolution photoacoustic microscopy (OR-PAM). Adapted with permission from [41]. © 2013 Society of Photo Optical Instrumentation Engineers.

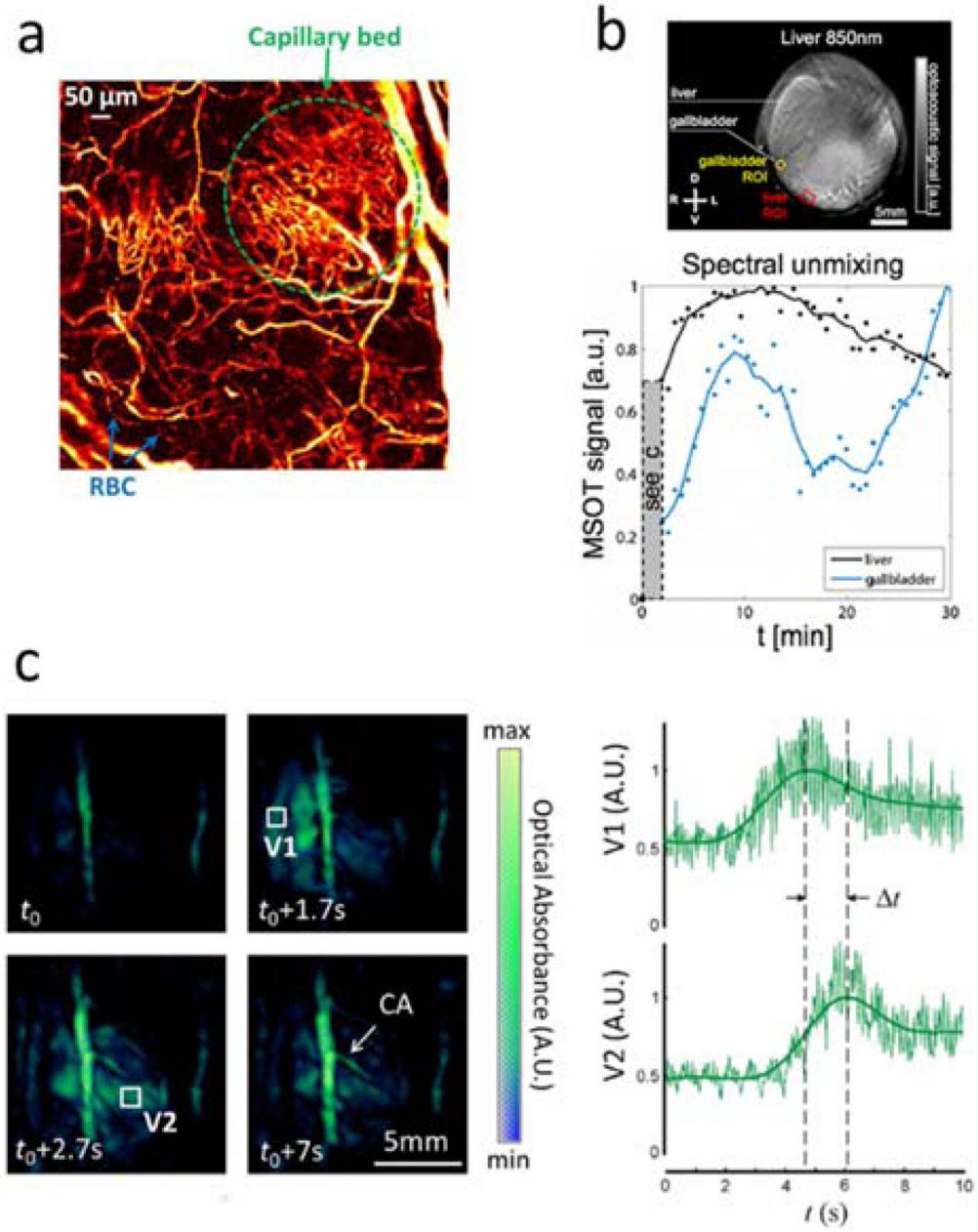

Fig 14.

Optoacoustic visualization of perfusion and organ function. (a) Capillary bed and individual red blood cells (RBC) traveling along a capillary imaged with optical-resolution photoacoustic microscopy (OR-PAM). Adapted with permission from [24]. © 2011 Optical Society of America. (b) Cross-sectional optoacoustic image of a mouse in the liver area obtained with MSOT. Time-lapse profiles of the unmixed ICG signal in liver and gallbladder are shown below. Figure is used under the Creative Commons Attribution 4.0 International License from [302]. A scale bar was added and image identification was altered. (c) Four snapshots from the high-frame-rate sequence of volumetric images of a beating mouse heart

taken during ICG injection with the 4D optoacoustic tomography (left) along with the time profiles of the signals for the right (V1) and left (V2) ventricles. The pulmonary transit time Δt is indicated. Figure is used under the Creative Commons Attribution International License from [100]. No changes were made.

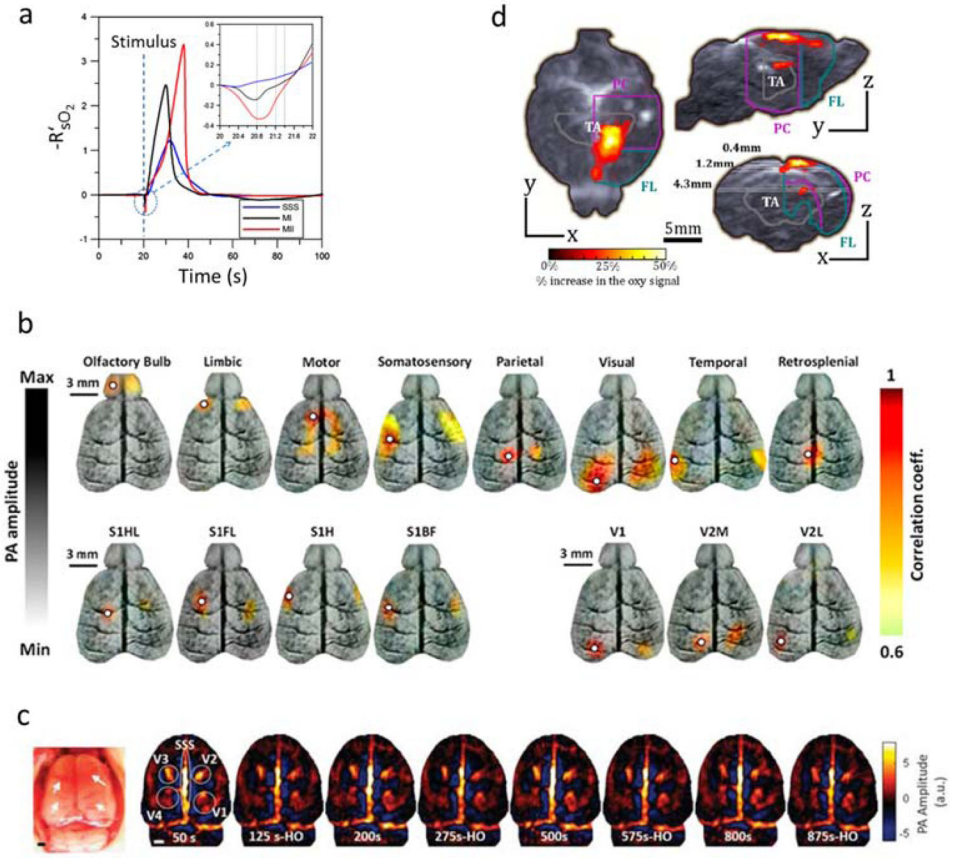

Fig 15.

Optoacoustic imaging of hemodynamic changes in the rodent brain. (a) Oxygen saturation changes of the superior sagittal sinus (SSS) and the contralateral MI and MII arterioles as a function of time obtained from A-line (1D) optoacoustic signals. Adapted with permission from [305]. © 2012 Sage Publications. (b) Functional connectivity maps in a live mouse brain acquired with cross-sectional optoacoustic tomography indicating eight main functional regions in the cortex. Figure adapted with permission from [121], © 2013 National Academy of Sciences. (c) Time series of rat brain images obtained with wearable cross-sectional optoacoustic tomography under alternating normoxia and hyperoxia (HO) conditions. Scale bar – 1mm. Adapted with permission from [306]. © 2015 Sage Publications. (d) Intensity plots of the epileptic-seizure-related activity as identified by correlating electroencephalogram (EEG) traces with optoacoustic hemodynamic responses obtained using 5D optoacoustic tomography. Adapted with permission from [101]. © 2017 Society of Photo Optical Instrumentation Engineers.

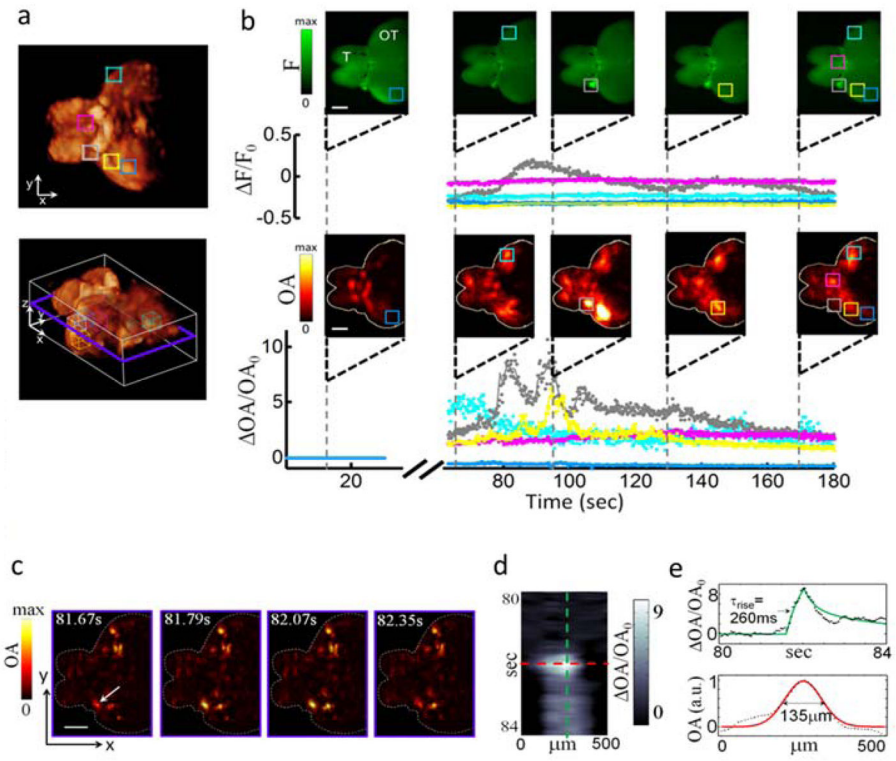

Fig 16.

Functional optoacoustic neurotomography (FONT) visualizes neuronal activity using the genetically-encoded calcium indicator GCaMP5G [255]. (a) Volumetric optoacoustic images of an adult zebrafish brain. (b) Real-time imaging of calcium activity with epi-fluorescence (top) and optoacoustics (bottom) after injection of the neurostimulant agent pentylenetetrazole (PTZ) into the brain. Temporal traces in the 5 marked regions of interest are shown. The fluorescence images have very blurry appearance indicating that the intense light scattering in large brains makes them inaccessible by optical microscopy methods. In contrast, FONT is able to provide high-resolution three-dimensional information regarding real-time neuronal activity in the entire scattering brain. (c) Time-resolved images from a single slice through the 3D data, as indicated in violet in (a). (d) Close-up spatio-temporal resolution analysis of a single line, whose orientation is indicated by an arrow in (c). (e) Temporal and spatial profiles through the image in (d). Scale bars − 500 μm. Adapted with permission from [255]. © 2016 - Macmillan Publishers Ltd.

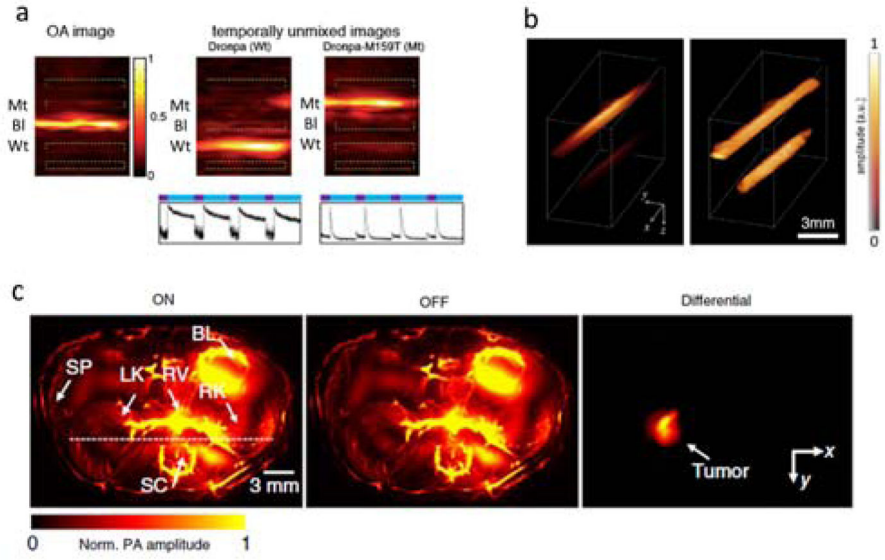

Fig 17.

Optoacoustic imaging of photoswitchable probes. (a) Temporal unmixing of Dronpa (middle) and its mutant variant Dronpa-M159T (right) from blood (left) as obtained from a time-lapse sequence of images acquired with 4D optoacoustic tomography. Adapted with permission from [130]. © 2015 Optical Society of America. (b) 3D optoacoustic images of two tubings containing Dronpa-M159T located at different depths in a light scattering medium before (left) and after (right) normalization with the calculated decay rates. Adapted with permission from [273]. © 2015 Optical Society of America. (c) Cross-sectional optoacoustic tomography images of a mouse with injected U87 tumor cells expressing the bacterial phytochrome BphP1 in its activated (left) and deactivated (middle) states along with the difference between the two images (right). Adapted with permission from [272]. © 2016 - Macmillan Publishers Ltd.

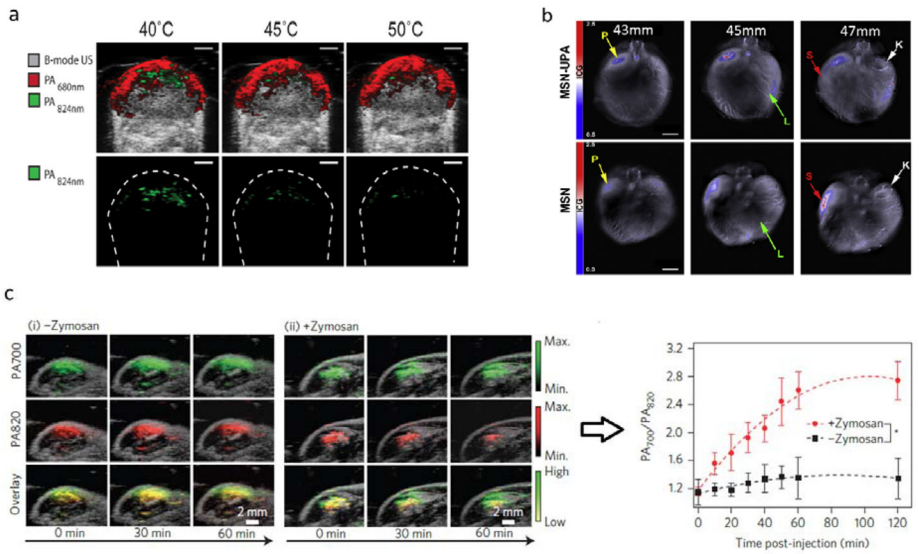

Fig 18.

Optoacoustic molecular imaging and sensing. (a) Temperature threshold sensing in tumour xenografts injected with J-aggregating bacteriopheophorbide a-lipid nanoparticles JPN16 by comparison of cross-sectional optoacoustic images at two different wavelengths. Figure is used under the License from Standard ACS AuthorsChoice/Editors' Choice Usage Agreement from [269]. A 1mm scale bar was added and image identification was altered. (b) Multispectral optoacoustic tomography (MSOT) images of a mouse implanted with S2VP10 pancreatic cancer cells after injection of mesoporous silica nanoparticles (MSN) with chitosan and urokinase plasmonigen activator (MSN-UPA) (top) or untargeted MSN (bottom). Scale bar – 5 mm. Adapted with permission from [311]. © 2015 Elsevier. (c) Optoacoustic sensing of reactive oxygen species (ROS) by comparison of cross-sectional optoacoustic images for saline-treated (left) and zymosan-treated (middle) regions in a mouse and the time profiles of the optoacoustic amplitude ratios for two wavelengths (right) after injection of ratiometric semiconducting polymer nanoparticles (RSPN). Adapted with permission from [145]. © 2014 - Macmillan Publishers Ltd.

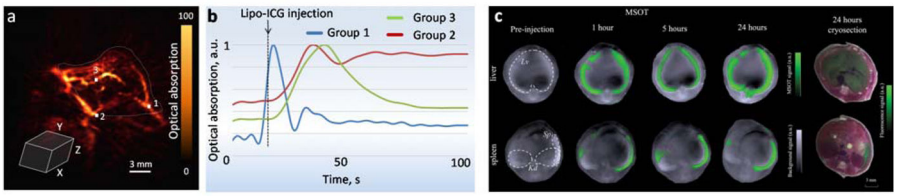

Fig 19.

Optoacoustic imaging of pharmacokinetics and bio-distribution. (a) Images of a subcutaneous 4T1 breast tumour in a mouse obtained with 4D optoacoustic tomography after injection of liposomal indocyanine green (Lipo-ICG). The corresponding temporal profiles for the three marked regions of interest are shown in (b). Adapted with permission from [312]. © 2015 European Society of Radiology with permission of Springer. (c) MSOT imaging of bio-distribution of a 1,1’-dioctadecyltetramethyl indotricarbocyanine iodide (DiR)-loaded polyethyleneimine functionalized poly(lactic-coglycolic acid) (PEI-PLGA) nanoparticles in a CD1 mouse. Green colour scale corresponds to the unmixed distribution of the probe. Adapted with permission from [313]. © 2015 John Wiley & Sons.

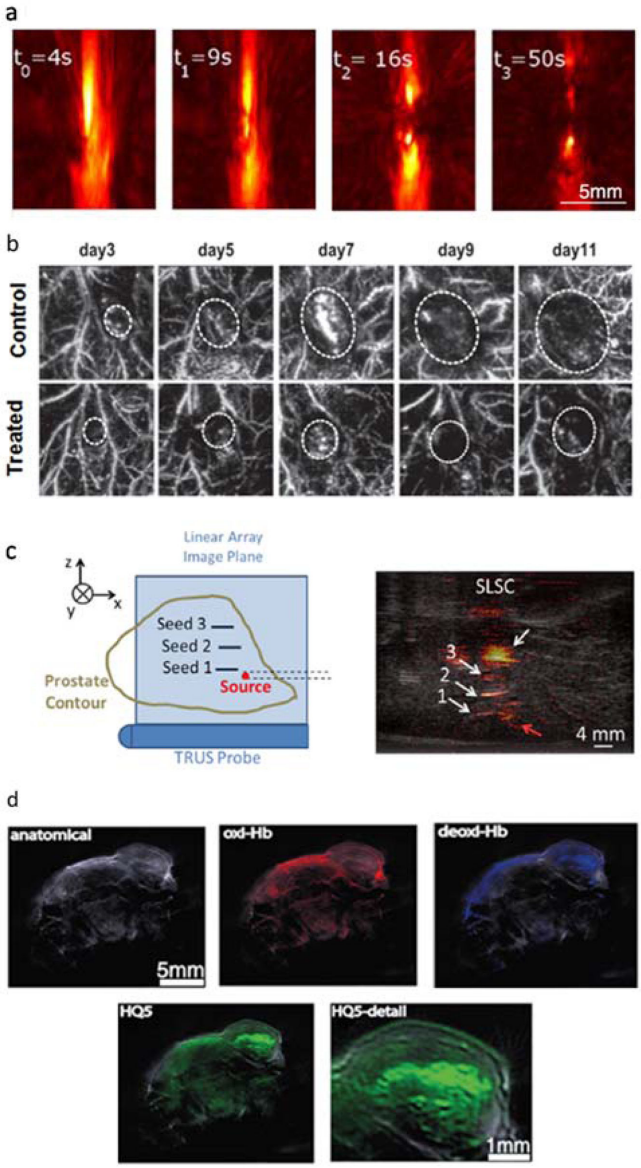

Fig 20.

Optoacoustic monitoring of treatments. (a) 4D optoacoustic monitoring of endovenous laser therapy (ELT) treatment aimed at eliminating incompetent truncal veins. Adapted with permission from [267]. © 2015 John Wiley & Sons, Inc. (b) Optoacoustic images of breast cancer xenografts receiving scrambled control (top) and intratumoral self-complementary AAV serotype 2 (scAAV2) septuplet-tyrosine mutant vectors encoding siRNAs against ATF6 (bottom). Adapted with permission from [317]. © 2013 Elsevier. A scale bar was added. (c) Optoacoustic images of brachytherapy seeds implanted in a canine prostate as obtained by means of a transrectal ultrasound probe. Adapted with permission from [318]. © 2014 Society of Photo Optical Instrumentation Engineers. (d) Multispectral optoacoustic tomography (MSOT) images of spontaneous 4T1-luc2 tumour necrosis with the carboxylated cyanine HQ5. Adapted with permission from [319]. © 2015 Impact Journals.

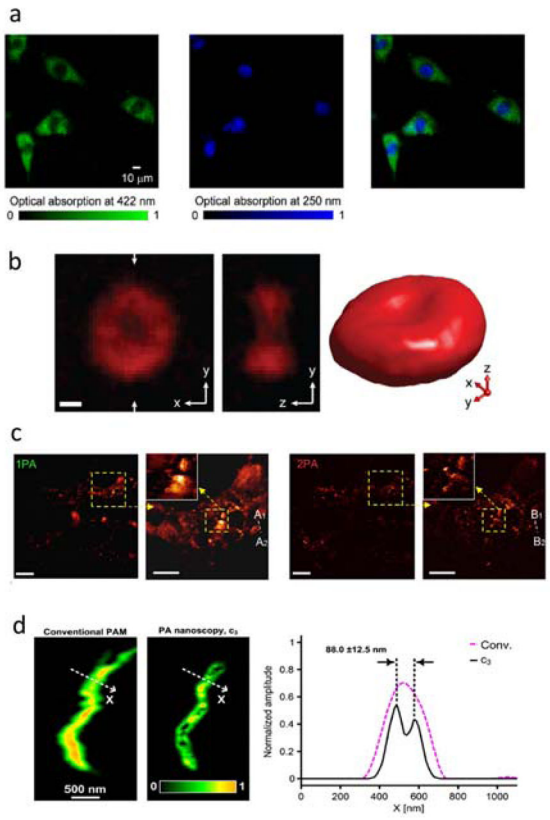

Fig 21.

Optoacoustic imaging of cellular and sub-cellular function. (a) OR-PAM images of the cytoplasms (green) and nuclei (blue) of fibroblasts. Adapted with permission from [320]. © 2013 Society of Photo Optical Instrumentation Engineers. (b) 3D images of red blood cells obtained with ultra-high frequency acoustic-resolution optoacoustic microscopy. Scale bar – 2μm. Adapted with permission from [51]. © 2017 IEEE. (c) *In vivo* images of the melanin distribution near the basal layer of the epidermis obtained with single-photon absorption (1PA) (left) and two-photon absorption (2PA) (right) optoacoustic microscopy. Scale bar – 50μm. Figure is used under the Creative Commons Attribution 3.0 International License from [37]. (d) Images of mitochondria in NIH 3T3 fibroblasts obtained with OR-PAM (left) and optoacoustic nanoscopy (middle) showing the enhanced resolution rendered with the latter approach for the indicated profiles (right). Adapted with permission from [32]. © 2014 Society of Photo Optical Instrumentation Engineers.

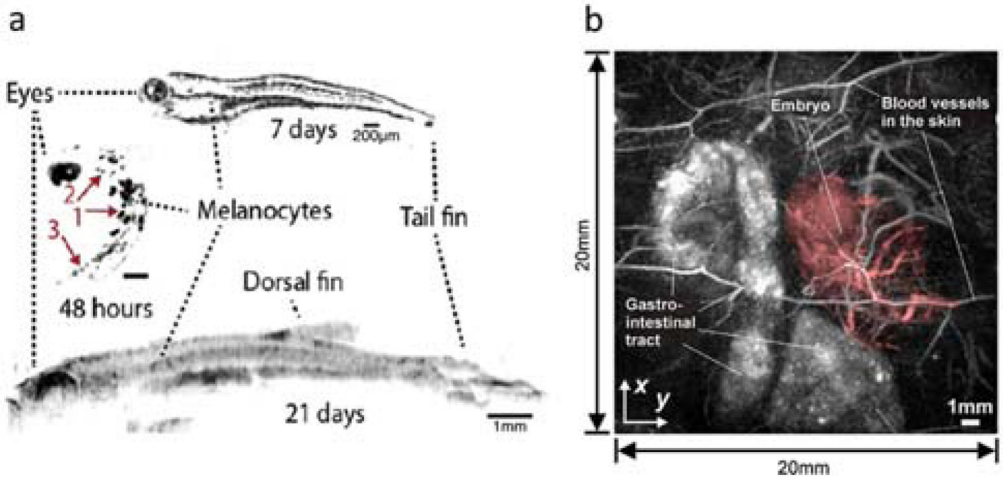

Fig 22.

Optoacoustic imaging of development. (a) Zebrafish images through stages of larval developmental obtained with hybrid focus optoacoustic microscopy (HFOAM). Adapted with permission from [321]. © 2015 Elsevier. (b) Optoacoustic images of a mouse embryo obtained with a Fabry-Pérot-based optoacoustic scanner. Adapted with permission from [322]. © 2012 Society of Photo Optical Instrumentation Engineers.

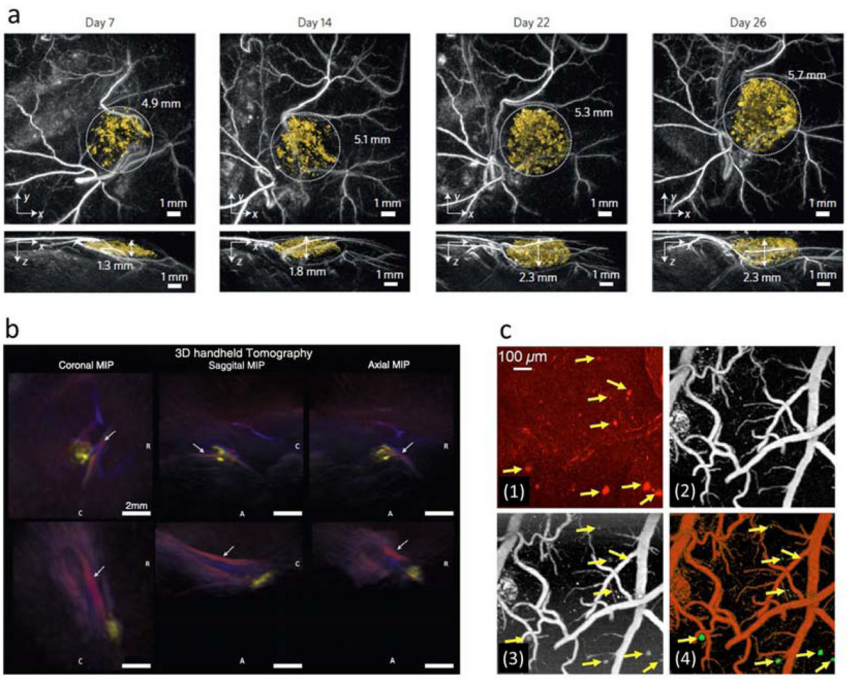

Fig 23.

Optoacoustic imaging of longitudinal dynamics and disease progression. (a) Images of implanted Tyr-expressing 293T cells at different time points post inoculation, acquired with the Fabry-Pérot-based optoacoustic scanner. Adapted with permission from [241]. © 2015 - Macmillan Publishers Ltd. (b) Optoacoustic imaging of melanoma micrometastasis in popliteal lymph node basin (top) and a large in-transit metastasis at upper third of lower thigh distal to popliteal basin (bottom) as obtained with handheld volumetric optoacoustic tomography scanner. Adapted with permission from [91]. © 2016 Radiological Society of North America. (c) In vivo imaging of amyloid plaques in a brain region of APPswe/PS1dE9 mouse injected with Congo-red. Images acquired with multiphoton microscopy (1) and dual-wavelength OR-PAM (2, 3, 4) are shown. Adapted with permission from [326]. © 2009 Optical Society of America.

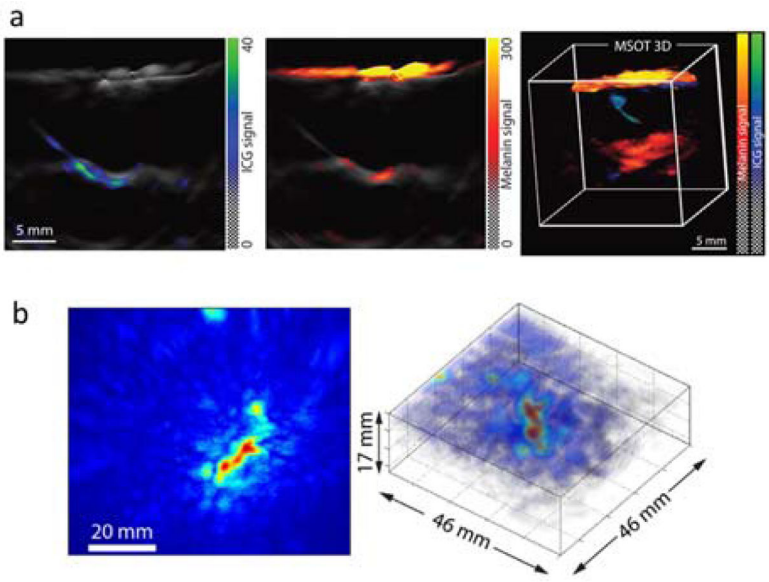

Fig 24.

Examples of clinical optoacoustic studies in oncology. (a) Metastatic status of sentinel lymph nodes in melanoma patients determined noninvasively with multispectral optoacoustic tomography (MSOT). Preoperative non-invasive assessment of ICG (green scale) and melanin (orange) distribution in suspected metastatic sentinel lymph nodes using handheld cross-sectional and volumetric MSOT scanners. Penetration of up to 5cm was claimed with 100% sensitivity and 48 to 62% lesion detection specificity. Adapted with permission from [106]. © 2015 AAAS (b) 3D optoacoustic images of a highly suspect cancer lesion in the breast of a female patient. Figure is used under the Creative Commons Attribution International License from [328]. Image identification was altered.

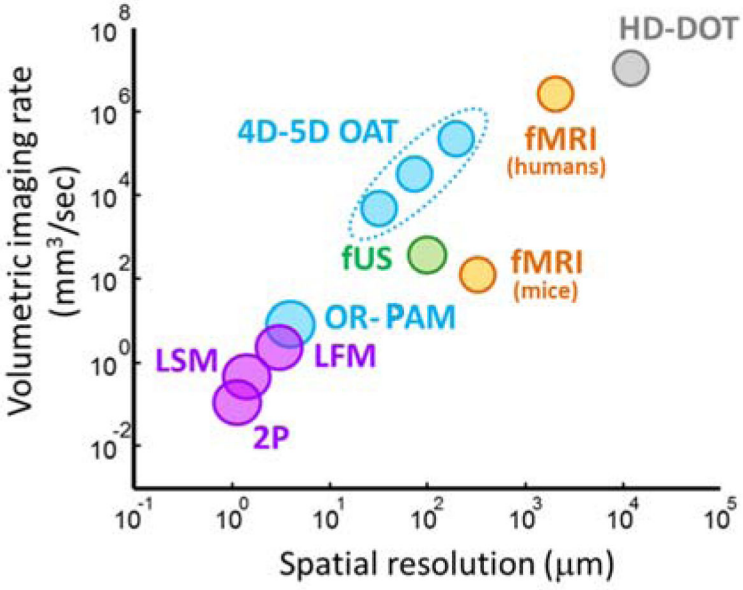

Fig 25.

Comparison of dynamic imaging capabilities of the various functional modalities used in small animal research and the clinics. Shown are: optical methods (violet) based on two photon microscopy (2P) [342], light-sheet microscopy (LSM) [343] and light field microscopy (LFM) [344]; small animal [345] and human [346] functional magnetic resonance imaging (fMRI - orange); high-density diffuse optical tomography (HD-DOT - gray) [347]; functional ultrasound (fUS - green) [348]; optical-resolution photoacoustic microscopy (OR-PAM) [22]; 4D and 5D optoacoustic tomography (4D-5D OAT) [255] (dots indicate three reported systems with isotropic resolution).